Microstructured Optical Arrays for use with soft X-rays

Shand, Matthew

Awarding institution:
King's College London

Title: Microstructured Optical Arrays for use with soft X-rays

Author: Matthew Shand

Matthew Thomas Shand

Microstructured Optical Arrays for use with soft X-rays

King's College London

A thesis submitted to King's College London for the degree of Doctor of Philosophy in the Department of Physics

7th May, 2012

For Nicola.

Acknowledgments

There are many people to thank for help, assistance and support throughout this thesis. Firstly, I would like to thank my supervisor, Dr. Graeme Morrison, for all of the guidance and support throughout my time at King's College London. Thanks also to Prof. Alan Michette, and Dr. Slawka Pfauntsch, for additional help, often provided at a moment's notice.

Much of the technical work would not have been possible without the time and dedication from the the technical support staff at King's College London, Bill Luckhurst, John Wilkinson and Ernest Samuel, in particular for assistance with the development of the microfocus source.

A big thank you to everybody at Silson ltd, both for providing the Micro Zone Plate, and diffraction gratings described within this work, and also for welcoming me so warmly during these past few months of writing. A special thanks to Peter Anastasi, Paul Duggan and Tony Howard for all the help and especially for the discussions on work when needed.

The opportunity to complete this thesis would not have been possible without the time and support from all the members of the Smart X-ray Optics consortium – thank you. Also, thanks to Prof. Alexei Erko at Helmholtz-Zentrum Berlin, for the opportunity to perform additional measurements on MOAs presented in chapter 4.

A thank you must go to Drs Peter Choi, Grainne Duffy and Keith Powell at NANO-UV, both for time spent during the STSM in Paris, and also for the opportunity to test the McXI-I microscope at KCL.

And finally, thanks to all my family and friends Mum, Dad, Toby, Liv, Rachel, James and especially to Nicola. I could not have completed this without the support you have shown me, the times you have allowed me to talk about my work in the knowledge that you thought I was talking utter nonsense!

The Smart X-Ray Optics consortium is funded by the UK Research Councils Basic Technology programme, grant code D04880X.
The characterisation of the McXI-I was funded as a Short Term Scientific Mission, supported by the COST MP0601 Action, funded by the European Science Foundation.
The McXI project is supported by the Eurostars Program McXI Σ!4885.

Contents

List of Figures

List of Tables

Abstract

Zone plates are commonly used in soft X-ray microscopy due to the high spatial resolutions achievable, however the performance is somewhat limited due to their small numerical aperture, combined with chromatic aberration and the multiple diffraction orders that are produced. Microstructured Optical Arrays (MOAs) have been proposed as an alternative method of focusing soft X-rays, using grazing incidence reflections from an array of channels, with the cumulative effect producing a small focused spot. The development and focusing properties of MOAs are described and simulated within this thesis, with comparison made to zone plates and other methods of focusing X-rays.

Experimental characterisation of MOAs and zone plates was achieved using a microfocused electron bombardment X-ray source. Necessary developments required to examine MOAs using the X-ray source and detector system are described, along with current calibration measurements, providing insight into the overall performance of the source.

The use of a CCD detector with the microfocus source has allowed comparison to be made between experimental measurements made to characterise the optical performance of MOAs and computer simulation.

The Smart X-ray Optics (SXO) consortium

The Smart X-ray Optics consortium has been developing focusing optics for soft X-rays for both large (astronomical) and small (laboratory) scale applications. The Microstructured Optical Arrays described and characterised within this thesis have been developed in collaboration with members of the consortium, including;

- **King's College London (KCL)** – Optical characterisation & Finite Element Analysis (FEA) modelling
- **University of Birmingham (UoB)** – Development of piezoelectric actuation & FEA modelling
- **Scottish Microelectronics Centre (SMC)** – Development of MOA structures and fabrication
- **University of Leicester (UoL)** – Optical characterisation & ray tracing
- **University College London (UCL)** – FEA modelling

Additional members of the consortium include;

- **Mullard Space Science Laboratory (MSSL)**
- **STFC Daresbury**

- **Diamond Light Source**
- **Silson Ltd.**
- **Gray Cancer Institute (GCI)**

A summary of publications arising from the SXO consortium on MOAs will now follow.

SXO publications relating to MOAs

[1] C. Dunare, W. Parkes, T. Stevenson, A. Michette, S. Pfauntsch, S. Sahraei, M. Shand, D. Zhang, D. R. Sanmartin, T. Button, C. Feldman, R. Willingale, P. Doel, H. Wang, and A. James. "Microstructured optical arrays for smart X-ray optics". In: *Proceedings of the SPIE - The International Society for Optical Engineering* 7360 (2009), 736015 (12 pp.) DOI: 10.1117/12.820598.

[2] C. Dunare, W. Parkes, T. Stevenson, A. Michette, S. Pfauntsch, M. Shand, T. Button, D. Rodriguez Sanmartin, D. Zhang, C. Feldman, R. Willingale, P. Doel, H. Wang, A. Smith, and A. James. "Micromachining optical arrays". In: *2010 International Semiconductor Conference (CAS 2010)* (Jan. 2010). DOI: 10.1109/SMICND.2010.5650215.

[3] A. Michette, T. Button, C. Dunare, C. Feldman, M. Folkard, D. Hart, C. McFaul, G. R. Morrison, W. Parkes, S. Pfauntsch, A. K. Powell, D. Rodriguez-Sanmartin, S. Sahraei, T. Stevenson, B. Vojnovic, R. Willingale, and D. Zhang. "Active micro-structured arrays for X-ray optics". In: *Advances In X-ray/EUV Optics and Components II* 6705 (2007), pp. 70502–70502.

[4] A. G. Michette, S. J. Pfauntsch, S. Sahraei, M. Shand, G. R. Morrison, D. Hart, B. Vojnovic, T. Stevenson, W. Parkes, C. Dunare, R. Willingale, C. Feldman, T. Button, D. Zhang, D. Rodriguez-Sanmartin, and H. Wang. "Smart X-ray

optics". In: *Journal of Physics: Conference Series* 186 (2009), 012067 (3 pp.) DOI: 10.1088/1742-6596/186/1/012067.

[5] A. G. Michette, S. J. Pfauntsch, S. Sahraei, M. Shand, G. R. Morrison, D. Hart, B. Vojnovic, T. Stevenson, W. Parkes, C. Dunare, R. Willingale, C. H. Feldman, T. W. Button, D. Zhang, D. Rodriguez-Sanmartin, H. Wang, and A. D. Smith. "Active microstructured X-ray optical arrays". In: *Proceedings of the SPIE - The International Society for Optical Engineering* 7360 (2009), 736007 (6 pp.) DOI: 10.1117/12.820171.

[6] D. Rodriguez Sanmartin, D. Zhang, T. Button, C. Meggs, C. Atkins, P. Doel, D. Brooks, C. Feldman, R. Willingale, A. Michette, S. Pfauntsch, S. Sahraei, M. Shand, A. James, G. Willis, C. Dunare, T. Stevenson, W. Parkes, and A. Smith. "Development of spider micro-structured optical arrays for X-ray optics". In: *Proceedings of the SPIE - The International Society for Optical Engineering* (Jan. 2010), 780306 (11 pp.) DOI: 10.1117/12.860420.

[7] D. R. Sanmartin, D. Zhang, T. Button, C. Atkins, P. Doel, H. Wang, D. Brooks, C. Feldman, R. Willingale, A. Michette, S. Pfauntsch, S. Sahraei, M. Shand, A. James, C. Dunare, T. Stevenson, W. Parkes, and A. Smith. "Progress on the development of active micro-structured optical arrays for X-ray optics". In: *Proceedings of the SPIE - The International Society for Optical Engineering* 7448 (2009), 744808 (10 pp.) DOI: 10.1117/12.826096.

[8] M. T. Shand, G. R. Morrison, A. G. Michette, S. J. Pfauntsch, D. Hart, T. Stevenson, W. Parkes, C. Dunare, R. Willingale, C. Feldman, T. Button, C. Meggs, and D. Rodriguez-Sanmartin. "Characterization of Micro-structured Optical Arrays". In: *The 10th International Conference on X-ray Microscopy* 1365 (2011). Ed. by I. NcNulty, C. Eyberger, and B. Lai, pp. 453–456. DOI: 10.1063/1.3625400.

[9] R. Willingale, C. Feldman, A. Michette, T. Button, C. Dunare, M. Folkard, D. Hart, C. McFaul, G. R. Morrison, W. Parkes, S. Pfauntsch, A. K. Powell, D. Rodriguez-Sanmartin, S. Sahraei, M. T. Shand, T. Stevenson, B. Vojnovic, and D. Zhang. "Active Microstructured Optical Arrays of Grazing Incidence Reflectors". In: *X-Ray Optics and Instrumentation* 2010, 56836 (2010), p. 856836. DOI: 10.1155/2010/856836.

[10] D. Zhang, D. Rodriguez-Sanmartin, T. W. Button, C. Atkins, D. Brooks, P. Doel, C. Dunare, C. Feldman, A. James, A. Michette, W. Parkes, S. Pfauntsch, S. Sahraei, T. Stevenson, H. Wang, and R. Willingale. "Development of piezoelectric actuators for active X-ray optics". In: *Journal of Electroceramics* 27.1 (Aug. 2010), pp. 1–6. DOI: 10.1007/s10832-009-9566-y.

[11] D. Zhang, D. R. Sanmartin, T. W. Button, C. Meggs, C. Atkins, P. Doel, D. Brooks, C. Feldman, R. Willingale, A. Michette, S. Pfauntsch, S. Sahraei, A. James, C. Dunare, T. Stevenson, W. Parkes, A. Smith, and H. Wang. "The fabrication and characterisation of piezoelectric actuators for active X-ray optics". In: *Proceedings of the SPIE - The International Society for Optical Engineering* 7448 (2009), 744807 (9 pp.) DOI: 10.1117/12.826018.

Chapter 1

Introduction

1.1 An introduction to X-ray optical science

The range of the electromagnetic spectrum between 0.12 keV and 120 keV is typically considered to be the X-ray region. Within this range, the term "X-ray" can broadly be divided into two further regions, "soft" X-rays for low energy (< 2 keV[1]) where the primary losses within the medium are due to absorption rather than scattering, with "hard" X-rays beyond. The requirement to manipulate or redirect X-rays within both of these regions either to form a focus spot from a point-like source, or alternatively to perform imaging (primarily microscopy) at X-ray energies has grown significantly over the last few decades. This has been driven primarily by the development and improvement of synchrotron sources providing continuous intense radiation at both soft and hard X-ray energies. Applications using X-ray focusing techniques have also increased, with X-ray imaging techniques now standard at synchrotron facilities. Along with the wide range of applications for focusing devices within synchrotron sources, there is also a demand for focusing elements for use within laboratory scale applications.

The main purpose of the work contained within this thesis is to describe and characterise the optical performance of Microstructured Optical Arrays (MOAs)

as shown in chapter 2, using a laboratory scale source. The development of an experimental system (chapter 3) designed to perform this characterisation will be described, as well as simulation tools supporting the results. The remainder of this chapter describes the current technologies used to focus X-rays, as well as outlining typical applications. A broad overview of X-ray science will be given within this chapter, highlighting only a small section of the variety of optics, sources and applications available. Most of the background contained within this chapter may be obtained from a variety of textbooks, [1–3], and relevant chapters are cited individually where appropriate. While the MOAs described within this thesis are designed primarily for use at soft X-ray energies, optical elements designed to focus hard X-rays will also be considered, in order to give an overview of the field. Firstly however the generation, and interaction of X-rays within a uniform material are described, as this will provide an insight into the novel techniques used to focus X-rays.

1.2 X-ray sources

The generation of radiation containing a strong spectral component within the X-ray region of the electromagnetic spectrum is most commonly achieved using the methods described below. X-ray generation using electrons bombarding a solid target will first be considered. This will allow the characteristics of the microfocus X-ray source described in chapter 3 to be understood. X-ray generation by synchrotron radiation and plasma interactions will also be discussed, in order to allow comparisons to be made.

1.2.1 Electron bombardment X-ray sources

X-ray generation using bombardment of a solid target by energetic electrons is a widely used method, and is routinely used in laboratories and medical facilities worldwide. This can provide a continuous source of X-rays with a broadband spectral emission. Bombardment of a target material (of atomic number Z) with electrons accelerated to a kinetic energy E_{e^-} results in the emission of X-rays from the target due to two separate processes. The properties of the emission are well described [4], and a brief summary will now follow.

Firstly, bremsstrahlung radiation is emitted due to the conversion of kinetic energy from the incident electron. The kinetic energy is lost due to interaction of the electron with the nucleus of the target material, with the highest radiation energy emitted limited to the kinetic energy of incident electrons, given by

$$E_{e^-} = E_{\max} = \frac{hc}{\lambda_{\min}}. \tag{1.1}$$

This high energy limit ($E_{\max}$) also describes the conversion of all electron kinetic energy into a single photon. The spectral distribution due to the bremsstrahlung emission below this cutoff energy can be approximately described for thick targets [4] (assuming multiple interactions between the electron and target) by equation (1.2),

$$I_\lambda \approx Cc^2 Z \frac{\lambda - \lambda_{\min}}{\lambda^3 \lambda_{\min}}, \tag{1.2}$$

where C describes a constant determined by the atomic parameters [4].

The shape of the resulting bremsstrahlung distribution estimated using equation (1.2) is shown for a range of incident electron energies in figure 1.1. As C is determined by the element that is bombarded by the electrons, exact comparison between different elements is not possible here. The total bremsstrahlung emission

is shown to increase with electron energy, with a peak X-ray emission energy, E_{peak} given by

$$E_{\text{peak}} \approx \frac{2}{3} E_{e^-}. \tag{1.3}$$

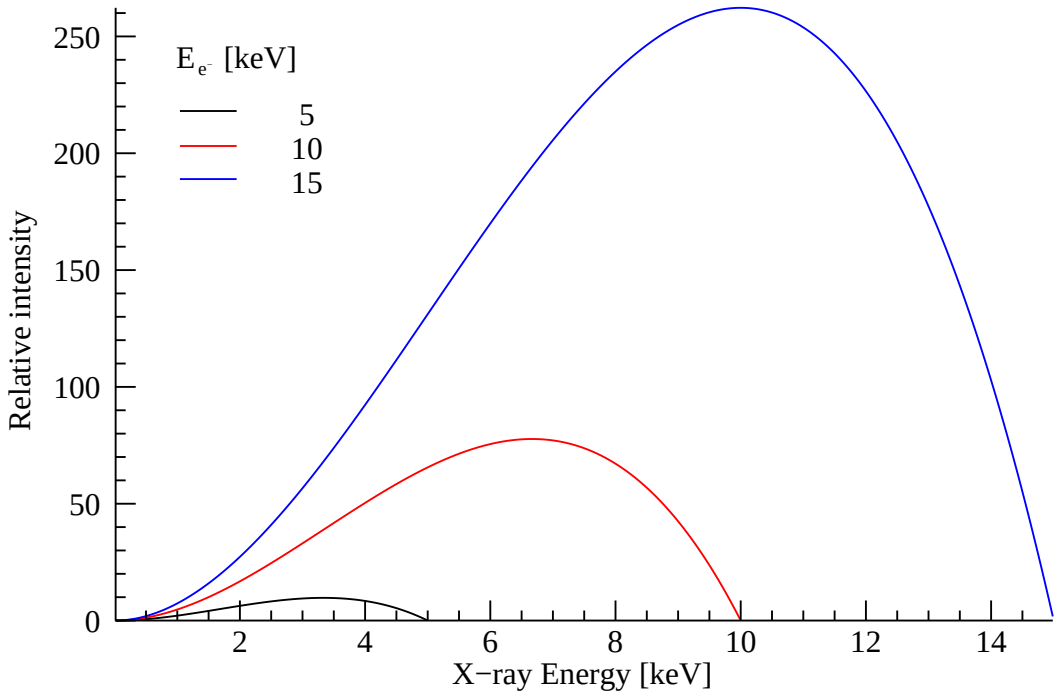

Figure 1.1: X-ray bremsstrahlung distribution calculated from equation (1.2) shows an increased intensity and peak emission energy for higher E_{e^-}.

The total power contained within the bremsstrahlung emission spectrum is typically very low compared to the power of the incident electron flux, and is approximately described by [4]

$$\epsilon = 0.92 \times 10^{-11} Z E_{e^-}. \tag{1.4}$$

The conversion efficiency is therefore still low ($< 1\%$) even for the bombardment of a high Z target with highly energetic electrons.

X-ray emission will also occur from an electron bombardment source at discrete

energies characteristic to the target material. Each of these spectral energy lines corresponds to electronic transitions within the target material, and will be emitted following the ionisation of an atom through bombardment by an incident energetic electron. This process causes an electron at a higher potential energy to relax into the hole created by the removal of an inner electron, emitting an X-ray in the process with an energy equivalent to the difference between the energy levels.

This process only occurs providing the kinetic energy of the energetic electron is greater than the ionisation energy of the atomic level.

The characteristic line emission will in general have a higher intensity relative to the bremsstrahlung emission, with the absolute intensity of a single line described by

$$I \propto (E_{\max} - E_i)^{1.63}, \tag{1.5}$$

with E_i being the ionisation energy for an individual line emission.

Electron bombardment sources have proved to be cost-effective, reliable laboratory scale sources of continuous, broadband emission X-rays. Although the overall intensity of the X-ray emission from a bombardment source is related to the kinetic energy and number of incident electrons, as well as the target material, high X-ray intensities are limited by factors such as target melting, preventing extremely bright sources. Several methods are currently available to reduce this effect, including rotation or cooling of the target, preventing heat from building up on a particular section of the target. More recently this heat loading problem has been overcome by using a heated liquid metal target [5], or using a non-metal liquid drop [6] as the target material.

1.2.2 Alternative X-ray sources

Although electron bombardment X-ray sources are popular in part due to their availability, as well as the simple technology and compact size, several additional methods of generation are also widely used. Both synchrotron and plasma sources are much brighter than the electron bombardment source. A review of each is given [7, 8], and the brief properties of each will now be summarised.

Synchrotron radiation is produced as energetic electrons circulate within a storage ring, with their path guided by magnetic fields. Such radiation is extracted along tangential lines radiating from the storage ring, with each typically many metres long. Each of these "beamlines" delivers a well defined beam of X-rays to an end station where experiments are to be performed, with the properties of the beam determined by optical elements placed along the beamline. Periodic magnetic structures may be inserted into linear segments around the storage ring, changing the properties of the delivered X-ray beam. Such devices, known as "wigglers" and "undulators" cause sinusoidal motion of the electron beam. In general [3] undulator radiation will produce X-rays with a narrow spectral range, with high brightness and partial coherence. Wiggler radiation will in general produce higher energy X-rays than bending magnet radiation.

X-ray generation is also popular on the laboratory scale, as synchrotron facilities are large multi-user machines, potentially with limited access. A comparable source brightness to that of a synchrotron may be obtained using radiation generated by the interactions within a plasma. Strong characteristic spectral lines may be emitted due to the recombination of ions and electrons within the plasma. Again, a broad spectral bremsstrahlung background is also observed. Many different methods of producing a plasma for use as a source of X-ray are currently used. These include z-pinch [9], and laser produced, where an intense laser beam is focused onto a target consisting of either a solid [10], liquid [11], gas [12] or even thin tape [13] target.

The typical brilliance of the three types of X-ray source identified are compared within table 1.1 [14], highlighting typical values of the time averaged brilliance of each source. It is important to note that the plasma sources are repetitive in nature, and so the peak brightness within the timescale of a single laser pulse will be higher.

Table 1.1: Comparison of the brilliance produced by the three different types of X-ray source (after [14])

	Electron bombardment	Plasma	Synchrotron
Brilliance [ph. s^{-1} $mrad^{-1}$ mm^{-2} 0.1% BW]	$\sim 10^8$	$\sim 10^{12}$	$\sim 10^{19}$

1.3 Optical properties of X-rays

The optical behaviour of X-rays is a critical factor in the design of an efficient lens for focusing applications. In this section, the refractive index for X-rays will be introduced, and related to the properties of refraction, reflection and absorption. These properties are essential in describing the properties of the X-ray focusing optics to be described in section 1.4.

1.3.1 Complex refractive index and refraction of X-rays

The complex refractive index n described by equation (1.6) is essential at X-ray energies to describe many different properties.

$$n = 1 - \delta - i\beta \tag{1.6}$$

The real term δ will affect the phase of the X-ray, while the complex term β largely describes the absorption properties.

Each component of the complex refractive index is related to the atomic

scattering factors, f_1^0 and f_2^0, given by equation (1.7) [3], where n_a is the average atomic density, and r_e the classical electron radius.

$$\delta = \frac{n_a r_e \lambda^2}{2\pi} f_1^0(\omega) \tag{1.7a}$$

$$\beta = \frac{n_a r_e \lambda^2}{2\pi} f_2^0(\omega) \tag{1.7b}$$

The scattering factors f_1^0 and f_2^0, are given elsewhere [15] as a function of X-ray energy (and therefore may be related to both ω and λ). It follows from this that the optical constants δ and β will also change with the X-ray energy. This is shown in figure 1.2, as δ and β are shown across the low energy X-ray spectrum.

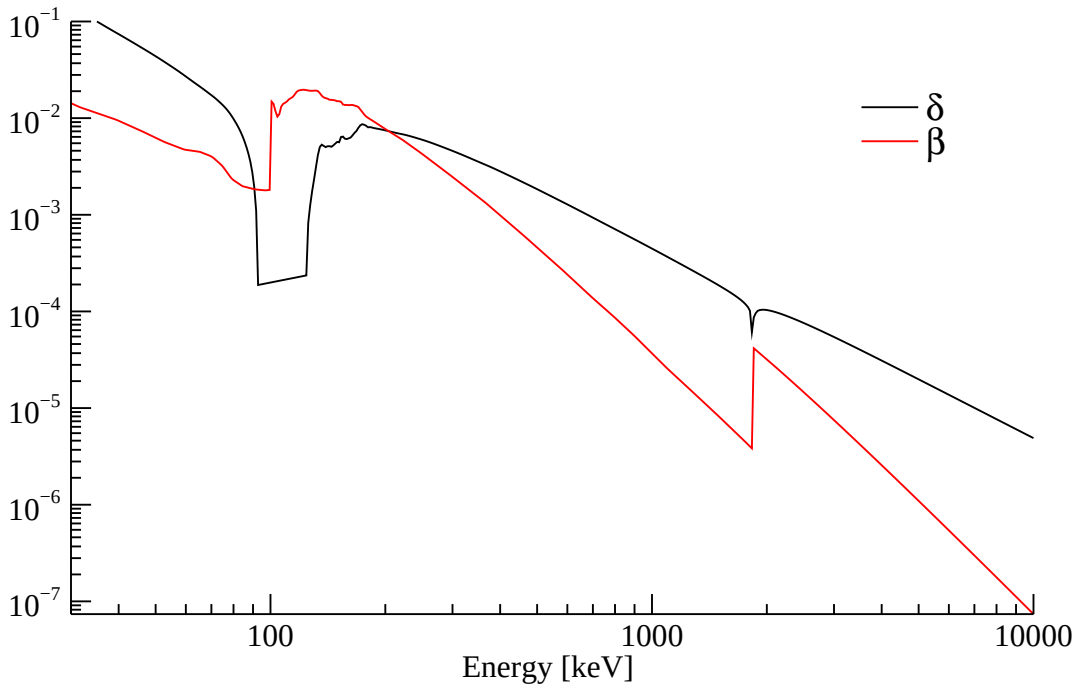

Figure 1.2: The optical constants δ and β across the X-ray region for silicon

It is shown in figure 1.2 that both δ and β decrease as the X-ray energy rises, with sharp oscillations occurring at $\approx 0.1\,\text{keV}$ and $\approx 2\,\text{keV}$. These two regions correspond to the energies of the Si L, and Si K absorption edges respectively. The

real part of the complex refractive index $(1 - \delta)$ is therefore slightly less than 1. As δ is shown to always be small when compared to unity, the difference in angle between the incident and refracted ray at the boundary between two different media will always be small.

1.3.2 X-ray reflection

The complex refractive index described by equation (1.6) is also important when considering the reflection of X-rays. This may be explained by considering the Fresnel equations at X-ray wavelengths [16]. Figure 1.3 shows radiation incident at a grazing angle θ, shown with the corresponding angles θ'_{T} and θ'_{R} for the transmitted and reflected X-rays respectively.

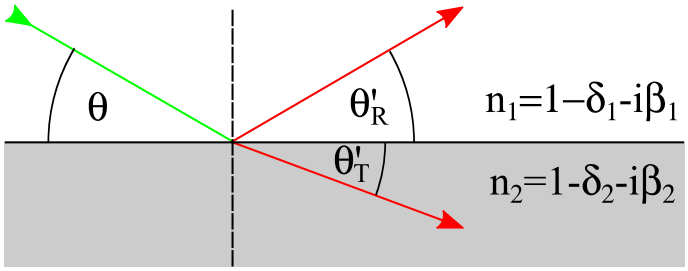

Figure 1.3: The transmission and reflection of radiation at a boundary between media of two different refractive indices. Angles are taken to be measured at grazing incidence from the boundary.

Clearly $\theta = \theta'_{\mathrm{R}}$, and when $\delta_1 = \beta_1 = 0$ (describing radiation passing from vacuum into a medium of refractive index n) the amplitude reflectivities (r) for the electric field vectors polarised parallel and perpendicular to the boundary are given by [16],

$$r_{\parallel} = \frac{n^2 \sin\theta - [n^2 - \cos^2\theta]^{\frac{1}{2}}}{n^2 \sin\theta + [n^2 - \cos^2\theta]^{\frac{1}{2}}} \tag{1.8a}$$

$$r_{\perp} = \frac{\sin\theta - [n^2 - \cos^2\theta]^{\frac{1}{2}}}{\sin\theta + [n^2 - \cos^2\theta]^{\frac{1}{2}}}, \tag{1.8b}$$

and may then be used to determine the intensity of the reflectivity for each

polarisation by

$$R_{\parallel} = r_{\parallel} r_{\parallel}^{*} \tag{1.9a}$$

$$R_{\perp} = r_{\perp} r_{\perp}^{*}. \tag{1.9b}$$

At normal incidence, this reduces for both polarisations to

$$R = R_{\parallel} = R_{\perp} = \frac{\delta^2}{4}. \tag{1.10}$$

As δ is small at X-ray energies, the reflectivity is also very small at normal incidence.

The reflectivity at small grazing incidence, however is significantly larger, compared to that close to normal incidence. To describe this, Snell's law of refraction may be rewritten in terms of the grazing incidence, as

$$\frac{\cos\theta}{\cos\theta_{\mathrm{T}}} = \frac{1-\delta_2}{1-\delta_1}, \tag{1.11}$$

where $\beta_1 = \beta_2 = 0$. Assuming the incident medium has refractive index $n_1 = 1$, then $n_1 > n_2$, and $\theta > \theta_{\mathrm{T}}$, so that the transmitted X-ray is always refracted towards the boundary. It follows from this that there must be a critical angle of incidence θ_{c} where $\theta_{\mathrm{T}} = 0$, and therefore the refracted X-ray will travel along the boundary. All incident grazing angles below this ($\theta < \theta_{\mathrm{c}}$) must be reflected. This high reflectivity is known as total external reflection, and the critical angle for grazing incidence reflection θ_{c} is given by [3]

$$\theta_{\mathrm{c}} = \sqrt{2\delta}. \tag{1.12}$$

The critical angle is typically a few degrees for soft X-ray energies, and falls

significantly for higher energies, since δ also decreases as shown in figure 1.2.

1.3.3 X-ray absorption

The attenuation of X-rays, particularly at low energies is also an important consideration. The absorption of X-rays within a medium where $\beta \neq 0$ may be represented by [14]

$$\frac{I}{I_0} = e^{\frac{-4\pi\beta t}{\lambda}}, \tag{1.13}$$

where t is the path length through the absorbing medium. The transmission of X-rays through a range of materials of different thicknesses is shown in Appendix A (Figures A.3 and A.4).

1.4 Overview of X-ray optics

Conventional refractive lenses, specifically those used for visible light, use the large changes in refractive index at the boundary between two different media. Such methods of redirecting X-rays to a focus are unsuitable at soft X-ray energies due to the high absorption, and small changes in refractive index [17]. The low reflectivities observed at near normal incidences also make X-rays difficult to focus. Novel techniques must therefore be applied in order to focus X-rays. This focusing effect will describe the redirection of X-rays in some way, allowing the optical elements devised to be used either to produce a magnified image, or alternatively to produce a focused spot or distribution of intensity, depending on the application.

The different types of X-ray focusing elements described within this section may be categorised using figure 1.4. It is shown that X-ray optics outlined use either diffraction, reflection or refraction in order to focus X-rays. The properties of the zone plate are described in detail, as one of the most widely used diffractive elements.

A more general overview of grazing incidence reflective optics is also given. The full description of MOAs will follow in chapter 2, as a focusing element using grazing incidence reflection for soft X-rays. Finally, alternative devices will be described, using refraction, or near-normal incidence reflection to produce focusing.

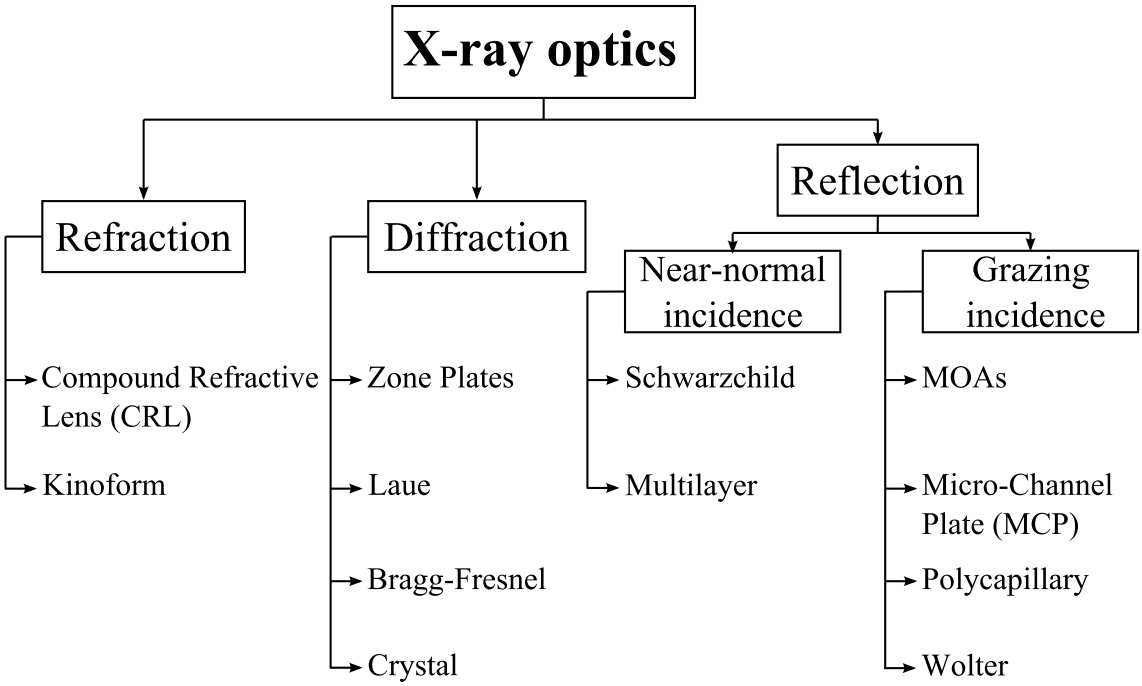

Figure 1.4: X-ray focusing devices fall into three main categories using diffraction, reflection and refraction.

1.4.1 Diffractive X-ray optics

The zone plate has become a fundamental component in achieving focusing for X-rays particularly within the soft X-ray region, with the number of applications using zone plates at higher energies increasing, using energies of up to several keV [18]. While the zone plate has the potential to focus radiation at any energy, they are primarily used within the X-ray regime due to the high spatial resolution achievable in comparison to other focusing optics within this energy range. The structure of a simple zone plate is shown in figure 1.5, where X-rays passing through each of the white (X-ray transparent) rings are diffracted. The darker solid rings of the

zone plate are initially assumed to be opaque to X-rays, and a sharp boundary is assumed between the alternating opaque and transparent zones. The radial width of each ring or zone is shown schematically in figure 1.5 to vary continuously, with the smallest width occurring at the outer edge of the zone plate. The width of this outer zone (d_n, where n is the total number of zones) is critical in describing the focusing properties of zone plates.

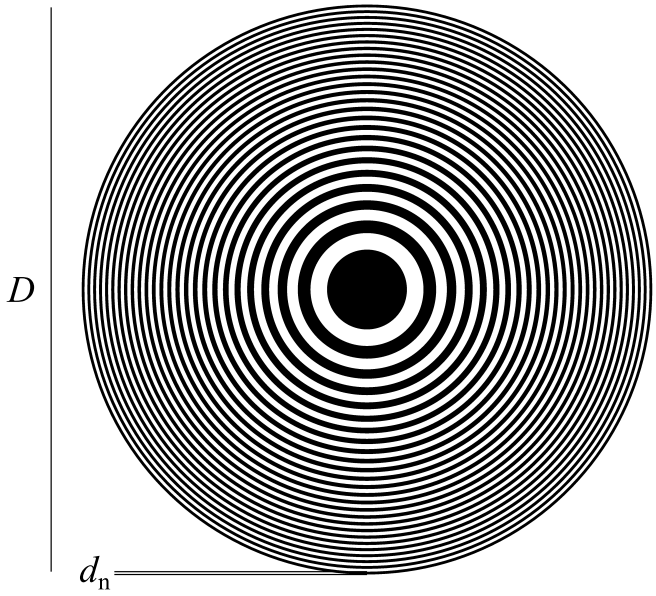

Figure 1.5: Schematic zone plate structure for focusing X-rays. Diffraction from each of the white X-ray transparent rings contributes to the focused spot produced.

The structure of zone plates, along with the focusing properties are described in detail in a variety of sources [1, 3, 18, 19], however the description presented within this section will largely follow that given by Morrison [20]. Focusing of X-rays using the zone plate structure shown in figure 1.5 is achieved as radiation diffracted by each transparent zone is redirected towards a common point. To describe this in further detail, the potential path of X-rays through a radial segment of a zone plate is shown in figure 1.6. Only the innermost and outer transparent zones of the zone plate are shown, with the structure of alternating opaque and transparent assumed to be distributed continuously between these limits. The radial distance from the

optical axis to the boundary between each zone is given by r, with the radius of the outer boundary (r_n) describing the overall radius of the zone plate.

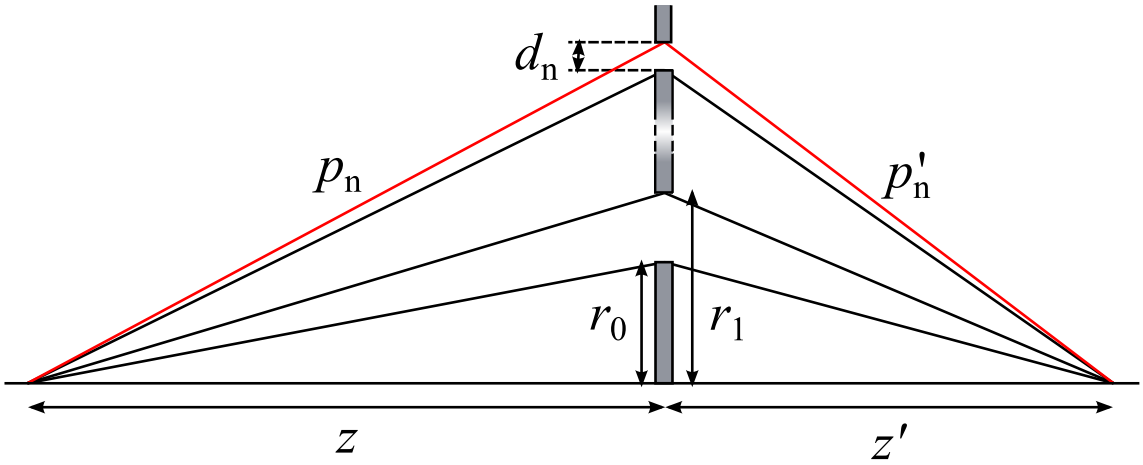

Figure 1.6: Potential X-ray paths through a zone plate. The outermost path (red) at a radius of r_n is described by the optical path $p_\mathrm{n} + p'_\mathrm{n}$

The total optical path length ($p_\mathrm{n} + p'_\mathrm{n}$) shown in figure 1.6 is described by the equation

$$p_\mathrm{n} + p'_\mathrm{n} = z + z' + \Delta + \frac{n\lambda}{2}, \tag{1.14}$$

where the path length between adjacent zones is shown to increase by $\frac{n\lambda}{2}$. In this way, constructive interference between successive transparent zones will occur. It follows from equation (1.14) that for the innermost zone ($n = 0$), the optical path is described as

$$p_0 + p'_0 = z + z' + \Delta, \tag{1.15}$$

meaning Δ is the additional path due to radiation passing through the first zone.

Pythagoras' theorem may be applied to equation (1.14) to relate p_n and p'_n to the axial distances z and z', which may then be simplified to give

$$r_\mathrm{n}^2 = n\lambda f + r_0^2, \tag{1.16}$$

where the focal length f is described by

$$\frac{1}{f} = \frac{1}{z} + \frac{1}{z'}. \tag{1.17}$$

It can then be shown from equation (1.16) that the width of the outermost zone ($d_{\mathrm{n}} = r_{\mathrm{n}} - r_{\mathrm{n-1}}$) is given approximately by

$$d_{\mathrm{n}} \approx \frac{\lambda f}{2r_{\mathrm{n}}} \Rightarrow f = \frac{2r_{\mathrm{n}}d_{\mathrm{n}}}{\lambda} = \frac{Dd_{\mathrm{n}}}{\lambda}. \tag{1.18}$$

The zone plate structure described will therefore focus X-rays in a manner predicted by the thin lens equation (1.17) in an equivalent way to that of visible light optics, with a focal length shown by equation (1.18) to depend critically on the width of the outer zone d_{n}, and overall diameter D. Equation (1.18) also indicates that the focal length of a zone plate will depend on the incident X-ray wavelength. The dependence of the focal length on the incident wavelength means that zone plates are often required to be used with a highly monochromatic X-ray source.

The diffractive properties of a zone plate will also result in radiation focused to different distances along the optical axis, due to the multiple diffraction orders produced. A more general form of equation (1.18) will describe this, shown by equation (1.19), describing the focal length for multiple orders of diffraction m.

$$f_{\mathrm{m}} = \frac{mDd_{\mathrm{n}}}{\lambda} \quad m = 0, \pm 1, \pm 2, \pm 3 \ldots \tag{1.19}$$

The effect of higher orders of diffraction produced by the zone plate is shown in figure 1.7. Radiation parallel to the optical axis falling on the zone plate is diffracted towards different focal points, each of which is located at the focal length from the zone plate, as $z = \infty$ in equation (1.17). The extended central region of the zone plate shown in figure 1.7 is assumed to be opaque to X-rays, allowing the focused spot produced by each order to be separated from the undiffracted background (not

shown).

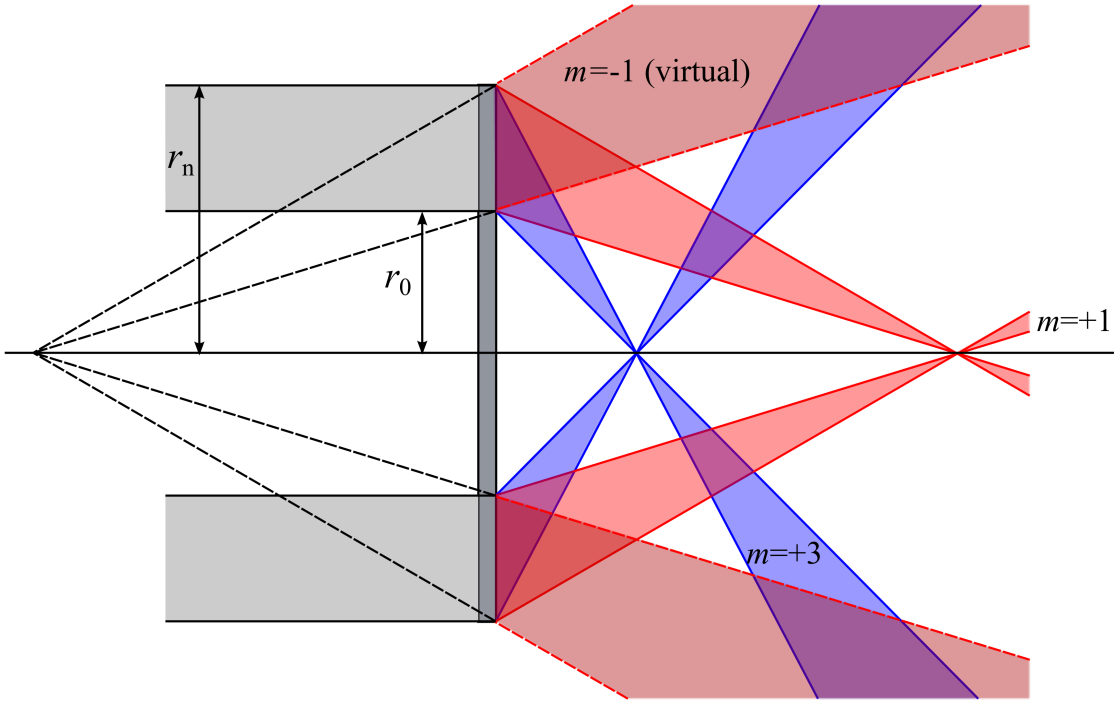

Figure 1.7: A selection of diffraction orders produced by a zone plate. Radiation initially parallel to the optical axis is focused towards many different focused spots.

The dashed line shown in figure 1.7 indicates the negative orders will produce a virtual focused spot upstream of the zone plate, with radiation appearing to diverge beyond this point.

Although radiation is assumed in equation (1.19) to be equally distributed into each order, this will not be the case in practice. The diffraction efficiency for the Fresnel zone plate described, where X-ray opaque zones absorb all incident radiation may be given as

$$\epsilon(m) = \begin{cases} 0.25 & m{=}0 \\ 0 & m{=}\text{odd} \\ \frac{1}{m^2\pi^2} & m{=}\text{even} \end{cases} \tag{1.20}$$

Equation (1.20) represents a theoretical maximum for the Fresnel zone plate, with diffraction efficiencies likely to be lower in practice. The diffraction efficiency between each order of diffraction will change if the boundaries of the zones do not follow equation (1.16) [21], as radiation is focused into the even orders as the ratio between the zones changes.

The diffraction efficiencies shown in equation (1.20) only represent a realistic example where the X-ray opaque zones are fully absorbing. An increase in the efficiency is achieved [22] by allowing the optical path within the opaque zones to increase by $\frac{\lambda}{2}$ for X-rays passing through the zone. Clearly this means that the opaque zones cannot be considered to be completely absorbing, and so will instead now be described as "solid" zones. As the optical path of X-rays within the solid zones is critical, the overall shift of the optical path will depend on the overall thickness, t of the zone plate.

Zone plates are commonly used to focus X-rays due to the high spatial resolutions achievable. This resolution can be determined, using the Rayleigh limit, as

$$\Delta_{\mathrm{r}} = \frac{1.22 d_{\mathrm{n}}}{m}, \tag{1.21}$$

and so the achievable resolution (for $m = 1$) only depends on the width of the outermost zone [20].

1.4.1.1 Production techniques for zone plates

As described in section 1.4.1 the overall efficiency of a zone plate may be linked to the thickness of the opaque zones (due to the changes in the optical path caused by the solid zones) with equation (1.21), indicating that the highest resolutions are obtained when the width of the outermost zone is smallest. In this respect an ideal zone plate may be required to contain an outer zone structure that is both of a very thin width, and high thickness. In general the aspect ratio is limited to around $\frac{t}{d_{\mathrm{n}}} = 4:1$ [3].

A brief description of typical production techniques used to fabricate high resolution zone plates now follows. This will include new ideas developed in order to overcome or complement the current manufacturing techniques. Two widely used [20] fabrication processes are shown in figure 1.8 highlighting the key stages used to create zone plate structures on a substrate (typically a thin film of silicon nitride).

Both of the methods outlined in figure 1.8 use electron-beam lithography to pattern the structure of a zone plate into a polymer resist. The material exposed to the electron beam is then removed in each method, leaving behind a pattern of the zone plate. The left hand side of figure 1.8 shows the zone plate structure electroplated onto the surface of the substrate. Following this, the polymer mould is removed, leaving the zone plate structure. An alternative process is shown in figure 1.8 b). This shows an identical patterning process on a resist, however there is then a pattern transfer process, resulting in a masking layer outlining the zone plate structure lying on the top surface of the layer to form the zone plate. A Reactive Ion Etch (RIE) process then removes the unmasked material, producing the final zone plate structure.

Zone plates have successfully been manufactured using these techniques in a wide variety of materials, with several recently published results summarised in table 1.2. This provides only a small overview of some of the different combinations of processes

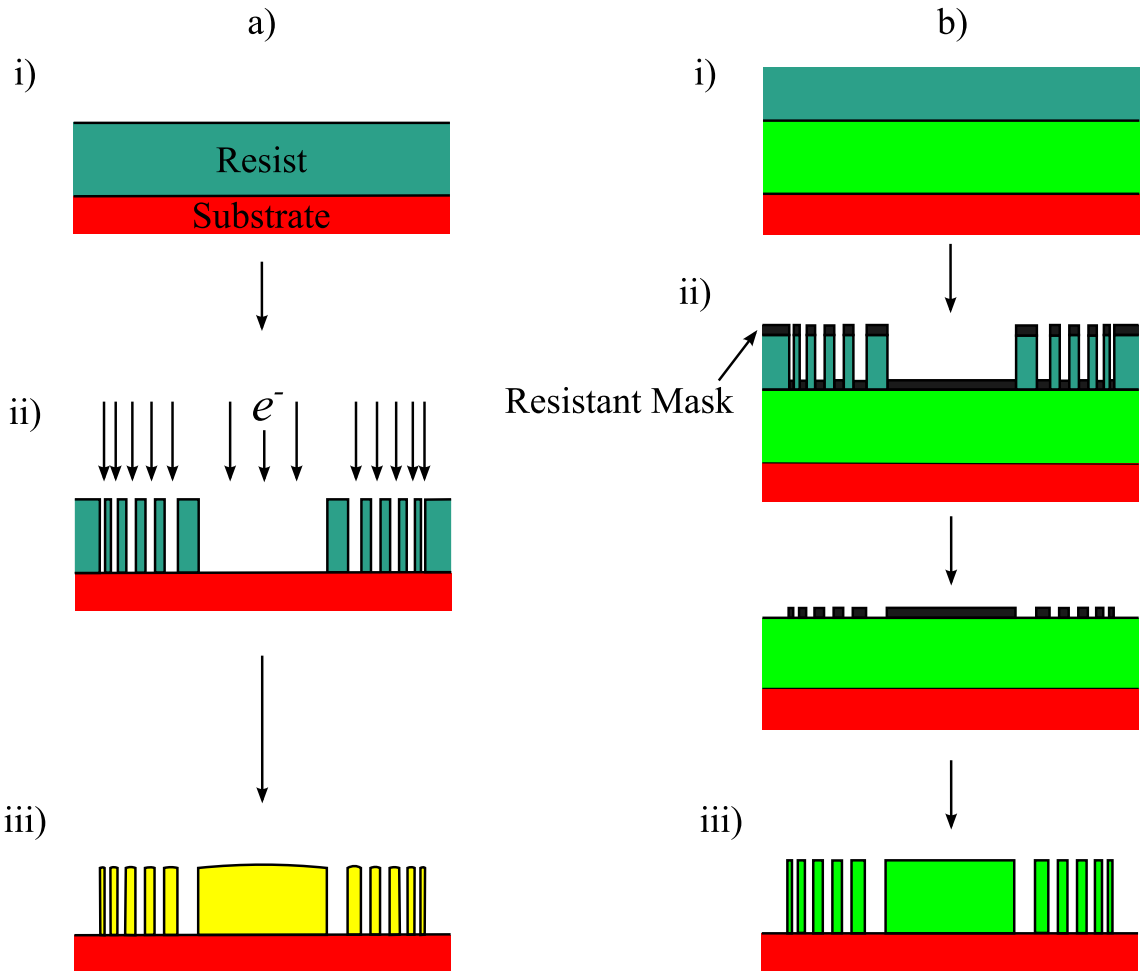

Figure 1.8: Two methods of zone plate fabrication. a) electroplating within a resist mold, and b) Reactive Ion Etching removing material unmasked by a resistant layer. Both processes require electron-beam lithography of a resist to produce the zone plate pattern.

used to manufacture zone plates.

Table 1.2 broadly indicates that the smallest zone widths are only achieved for the thinnest zone plate structures. By relaxing the requirement for a small width, thicker structures can be fabricated. This places a limitation in the fabrication of the zone plates, and therefore the best performance possible.

Techniques have also been developed in order to place less demand on the lithographic process required to produce zone plates. For example, an overlay technique [27] has been successfully developed in order to create an outer zone width of 12 nm using a double exposure technique, and has been used to resolve

Table 1.2: Summary of zone plate fabrication results.

Element	Production method	Energy (keV)	d_n (nm)	D (μm)	t (nm)	Ref.
Ni	Figure 1.8a)	0.5	20	55	130	[23]
Au	Figure 1.8a)	-	70	-	135	[23]
Si	Figure 1.8b)	0.5	30	100	200	[24]
Ge	Figure 1.8b)	0.4	30	56	310	[25]
Ge	Figure 1.8b)	2.4	100	300	900	[26]

a test specimen containing 12 nm period lines. A line-spacing of 20 nm has also been reported [28], using a technique where the line density of the outermost zones is "doubled" by coating the side walls of X-ray transparent zones with a layer of Ir, creating opaque zones of twice the line density. This therefore relaxes the requirement for the high density "writing" of the zone plate pattern performed during the lithography, as fewer zones need to be defined in the resist pattern. The examples discussed here once again only highlight a small selection of the current novel designs used to produce zone plates.

1.4.2 Reflective X-ray focusing optics at grazing incidence

The X-ray reflectivity at a planar boundary between two materials with different refractive indices has previously been described within section 1.3. It has been shown that X-rays are not efficiently reflected for grazing reflection angles greater than the critical angle θ_c. The high reflectivity for grazing angles below θ_c may be used to produce focusing of X-rays from a shaped surface (circular, elliptical, parabolic etc.). Grazing incidence reflective optics for soft X-rays have many different applications, from use as synchrotron radiation mirrors [29] and astronomical imaging to smaller scale laboratory applications.

As described by Michette [16], the aberrations present using single reflections from a continuous spherical surface become large at grazing incidences. This is not

a limiting factor for reflective optical elements at grazing incidence however, and reflecting mirrors using grazing incidence are used at synchrotron facilities worldwide [30], typically using a double reflection [31] in order to produce focusing in two dimensions by use of a pair of orthogonal cylindrical or elliptical mirrors.

Reflective optics using single reflections from a regular array of reflecting surfaces also have applications in X-ray focusing. Each of the reflecting surfaces within the array will focus X-rays towards the focused spot, with the cumulative effect from each reflecting channel describing the overall intensity obtained. Description of such arrays used to focus X-rays will be given in chapter 2, with the introduction of a novel focusing optic currently in development – the Microstructured Optical Array. The focusing properties of this optical element will be described in detail, along with comparison made to other reflective arrays used at X-ray energies.

1.4.3 Alternative X-ray focusing optics

Figure 1.4 indicates that focusing of X-rays is also possible through the use of refraction, through the use of Compound Refractive Lenses (CRLs). These lenses are typically used at high X-ray energies, where absorption is negligible, and use the combined refracting effect from many boundaries along the X-ray path [32]. Similar devices such as kinoform lenses [33] and Fresnel lenses [34], use refraction in a similar way, also to focus high energy X-rays.

Reflection at near normal incidences is achieved at X-ray energies using multilayer mirrors. These mirrors use alternating layers of high and low Z materials (such as Mo/Si), deposited onto a substrate. The total X-ray reflectivity of a multilayer is generated from the contributions from each reflecting boundary. Shaping of the multilayer surface results in a surface suitable for focusing X-rays at angles well beyond the critical angle of grazing incidence reflection. One typical geometry using such a shaped multilayer is a Schwarzschild objective [35], where

two reflections are used at near normal incidence.

1.5 Applications of soft X-ray optics

The X-ray optics described in section 1.4 are currently used both within laboratory and synchrotron user facilities worldwide, either as imaging optics used in X-ray microscopy, or in the formation of a small ($< 0.1\,\mathrm{mm}$) diameter focused spot, that may be used as an X-ray probe. The wide variety of applications for using focused X-rays ranges from biology to magnetism and environmental sciences [18] to highlight only a small sample.

1.5.1 X-ray microscopy

The field of X-ray microscopy has grown in recent years [36], due to the development of high intensity synchrotron sources, combined with advances in manufacturing processes allowing the development of high spatial resolution optics (such as zone plates). One of the driving factors behind the development of X-ray microscopy has been an improved resolution over complementary techniques, such as microscopy using visible light, with thicker samples being imaged due to the higher energy X-rays produced by third generation synchrotrons. An initial region of interest in X-ray microscopy is the "water window" – the low energy region between ≈ 200 to $400\,\mathrm{eV}$, as water is transparent to X-rays within this energy range. This allows the imaging of hydrated biological specimens to be realised, without preparation such as dehydrating or staining, as required in alternative techniques such as electron microscopy.

Two methods are widely used in order to achieve the magnified X-ray image of the specimen. These are known as Transmission X-ray Microscopy (TXM), and Scanning Transmission X-ray Microscopy (STXM). A brief description will now

follow of both techniques. TXM uses a high resolution objective lens in order to magnify the image of the specimen onto a multi-element detector, such as a CCD, with contrast in the image obtained due to absorption within the specimen. In order for this to occur, radiation must first be focused onto the specimen using a condenser. This is shown in figure 1.9 a). Typically both the condenser and objective are zone plates.

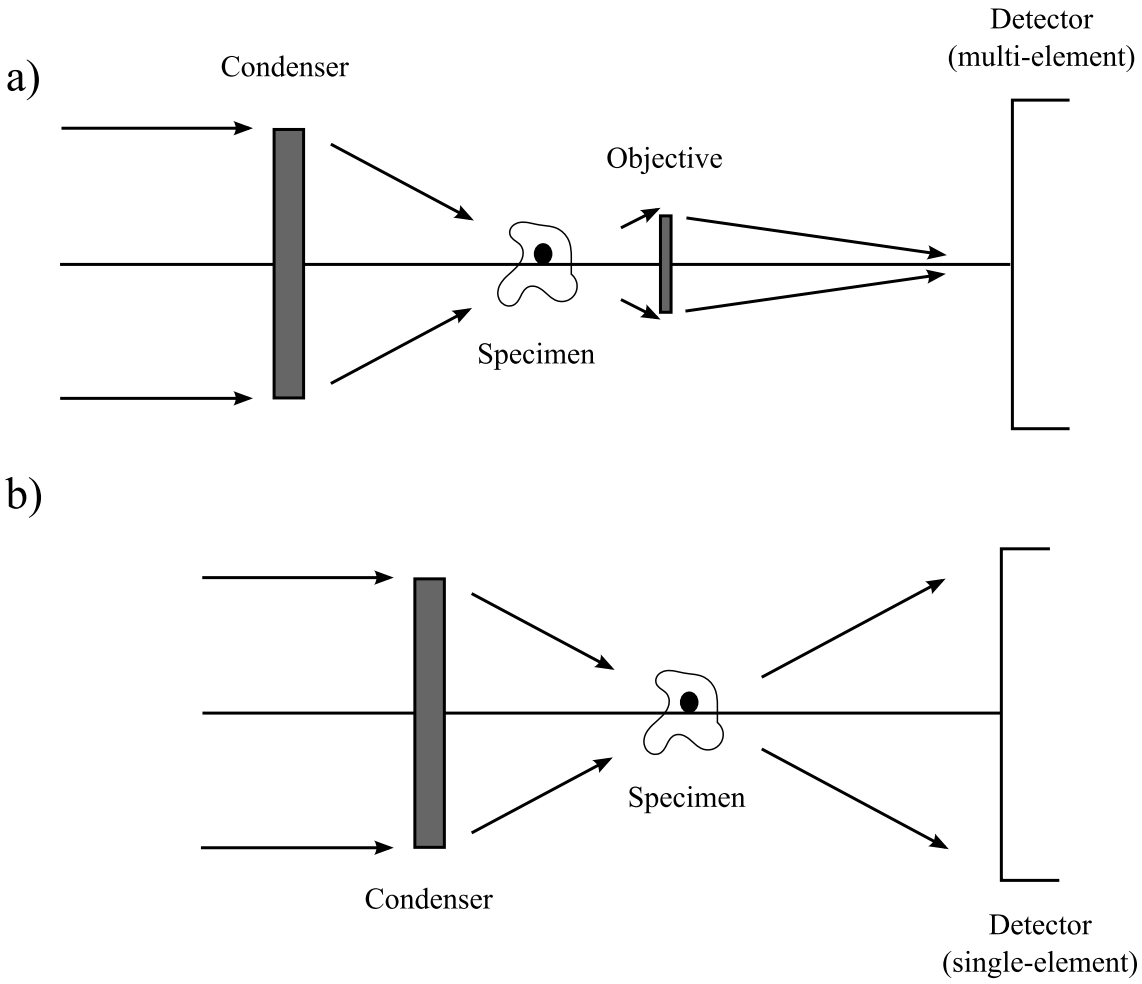

Figure 1.9: Geometries used for X-ray microscopy. a) TXM showing the condenser lens, specimen and objective. b) STXM showing the condenser lens and specimen.

Figure 1.9 b) shows an X-ray microscope configured with an STXM geometry. This shows X-rays focused by an X-ray condenser onto the specimen. X-rays passing through the specimen without absorption are then able to pass to the single element detector. Raster scanning of the specimen across the probe produced by

the condenser lens will allow a magnified image to be constructed, with each step of the raster scan corresponding to a pixel element of the specimen image. Both TXM and STXM geometries are widely used at synchrotrons worldwide, with resolutions now approaching 12 nm [27].

The STXM geometry uses a small diameter probe focused onto a small region of the specimen, and is therefore considered to be more suitable for use with specimens that are sensitive to the radiation dose from the X-rays (i.e. biological tissues). Compared with this, TXM offers faster image acquisition times [3], however the radiation is distributed over the area of the focused spot produced by the condenser, potentially causing damage to the specimen. One of the additional advantages to the STXM geometry is the ability to easily perform elemental studies (stereomicroscopy) by changing the energy of the incident X-ray beam. This allows any changes in the transmission images due to absorption to be examined. Such image acquisition allows a stack of images to be constructed, with each image corresponding to a different X-ray energy.

Both TXM and STXM have been demonstrated in a tomographic mode (see for example [37]) allowing projection images of the specimen to be taken as it is rotated around an axis. These images may then be combined using computer reconstruction, creating a 3-D representation of the specimen. Cryogenic fixing of the specimen (see for example [38]) is also now common when using radiation sensitive specimens in order to limit damage due to the X-ray beam.

X-ray microscopy using synchrotron based sources is not limited to the two methods described, and there has been great interest in phase contrast techniques [39] allowing low contrast imaging to be performed. More recently, lensless imaging techniques such as Coherent Diffractive Imaging (CDI) [40] and ptychography [41] have been demonstrated, and allow the reconstruction of an image to be performed using the collected diffraction pattern. Such techniques require the use of a highly

coherent X-ray beam, as well as significant computing power to reconstruct the image of the specimen.

X-ray microscopy is not restricted to synchrotron facilities, with microscopes using both TXM [42] and STXM [43] techniques successfully used to obtain soft X-ray images within a laboratory. The characterisation of such a microscope using a TXM geometry is described in chapter 5, developed as part of the McXI project to produce a commercial, tabletop X-ray microscope with high spatial resolution in the water window.

1.5.2 X-ray microprobing

Applications using focusing of X-rays are not limited to only microscopy, there are other techniques routinely performed using a probe of X-rays focused to a small spot of around a few μm in diameter. These include X-ray Fluorescence (XRF), X-ray diffraction and Extended X-ray Absorption Fine Structure (EXAFS) experiments. Each of these requires a tightly focused X-ray beam, in order to probe small sections of the specimen.

Microfocused distributions of X-rays may also be used within a laboratory environment [44, 45], as a probe used to irradiate sub-cellular components, used for radiobiological experiments. The laboratory scale experiments here require a high intensity focused X-ray spot to ensure a high throughput of specimens, improving statistical results. While measurements have been performed using only the focused spot formed using zone plate optics, the Microstructured Optical Array (MOA) described in chapter 2 may improve the X-ray flux in the focused spot.

1.6 Summary

Soft X-rays are widely used at synchrotrons and laboratories worldwide within applications such as microscopy which require a tightly focused, well defined spot of X-rays. Traditional refracting lenses, analogous to those typically used for focusing visible light are not suitable for soft X-rays, as losses due to absorption are high, with the small changes in refractive index leading to long focal lengths [1]. Soft X-rays are also known to exhibit low reflectivities, except at grazing incidence. The use of a Microstructured Optical Array, as a focusing element for soft X-rays, using grazing incidence to produce X-ray focusing will now be described.

References

[1] A. G. Michette. *Optical Systems for soft X-rays*. Plenum, 1986.

[2] A. G. Michette and C. J. Buckley, eds. *X-Ray Science & Technology*. IOP Publishing, 1993.

[3] D. Attwood. *Soft X-Rays and Extreme Ultraviolet Radiation*. Cambridge University Press, 1999.

[4] A. W. Potts. *X-Ray Science & Technology*. Ed. by A. G. Michette and C. J. Buckley. IOP Publishing, 1993. Chap. 2.

[5] O. Hemberg, M. Otendal, and H. M. Hertz. "Liquid-metal-jet anode electron-impact x-ray source". In: *Applied Physics Letters* 83.7 (2003), pp. 1483–1485.

[6] T. Tuohimaa, J. Ewald, M. Schlie, J. M. Fernandez-Varea, H. M. Hertz, and U. Vogt. "A microfocus x-ray source based on a nonmetal liquid-jet anode". In: *Applied Physics Letters* 92.23 (2008).

[7] S. L. Hulbert and G. P. Williams. *Handbook of Optics*. Ed. by M. Bass. 2nd ed. Vol. 3. McGraw-Hill, 2001. Chap. 32, pp. 32.1–32.20.

[8] A. G. Michette. *X-Ray Science & Technology*. Ed. by A. G. Michette and C. J. Buckley. IOP Publishing, 1993. Chap. 4, pp. 110–159.

[9] M. Benk, D. Schaumlfer, T. Wilhein, and K. Bergmann. "High power soft x-ray source based on a discharge plasma". In: *Journal of Physics: Conference Series* 186.1 (Jan. 2009). DOI: 10.1088/1742-6596/186/1/012024.

[10] J.-H. Lim, K.-Y. Nam, K.-W. Kim, Y.-M. Kwon, J.-G. Park, J. H. Min, H.-H. Son, J.-Y. Min, and K.-H. Yoon. "Development of laser plasma-based soft X-ray microscopy". In: *Proceedings of the SPIE - The International Society for Optical Engineering* 5918 (Jan. 2005). DOI: 10.1117/12.626319.

[11] L. Malmqvist, L. Rymell, M. Berglund, and H. M. Hertz. "Liquid-jet target for laser-plasma soft x-ray generation". In: *Review Of Scientific Instruments* 67.12 (Dec. 1996), pp. 4150–4153.

[12] H. Fiedorowicz. "Generation of soft X-rays and extreme ultraviolet (EUV) using a laser-irradiated gas puff target". In: *Laser And Particle Beams* 23.3 (Sept. 2005), pp. 365–373.

[13] A. G. Michette, I. C. E. Turcu, M. S. Schulz, M. T. Browne, G. R. Morrison, P. Fluck, C. J. Buckley, and G. F. Foster. "Scanning-X-Ray Microscopy Using A Laser-Plasma Source". In: *Review Of Scientific Instruments* 64.6 (June 1993), pp. 1478–1482.

[14] A. G. Michette. *X-Ray Science & Technology*. Ed. by G. Michette A and C. J. Buckley. IOP Publishing, 1993. Chap. 1.

[15] B. L. Henke, E. M. Gullikson, and J. C. Davis. "X-Ray Interactions - Photoabsorption, Scattering, Transmission And Reflection At E=50-30,000 eV, Z=1-92". In: *Atomic Data And Nuclear Data Tables* 54.2 (1993), pp. 181–342.

[16] A. G. Michette. *X-Ray Science & Technology*. Ed. by A. G. Michette and C. J. Buckley. IOP Publishing, 1993. Chap. 7, pp. 254–304.

[17] C. A. MacDonald and W. M. Gibson. *Handbook of Optics*. Ed. by M. Bass. McGraw-Hill, 2001. Chap. 19, pp. 19.5–19.10.

[18] M. Howells, C. Jacobsen, and T. Warwick. *Science of Microscopy*. Ed. by W. Hawkes and J. C. Spence. Vol. 2. Springer, 2007. Chap. 13, pp. 835–926.

[19] E. Spiller. *Soft X-ray Optics*. SPIE Press, 1994.

[20] G. R. Morrison. *X-Ray Science & Technology*. Ed. by A. G. Michette and C. J. Buckley. IOP Publishing, 1993. Chap. 8.

[21] A. G. Michette. *Handbook of Optics*. Ed. by M. Bass. 2nd ed. Vol. 3. McGraw-Hill, 2001. Chap. 23, pp. 23.1–23.9.

[22] J. Kirz. "Phase Zone Plates For X-Rays And Extreme Uv". In: *Journal Of The Optical Society Of America* 64.3 (1974), pp. 301–309.

[23] A. Holmberg, M. Lindblom, J. Reinspach, M. Bertilsson, and H. M. Hertz. "Soft x-ray zone plate fabrication at KTH, Stockholm". In: *9th International Conference On X-ray Microscopy* 186 (2009). DOI: 10.1088/1742-6596/186/1/012065.

[24] J. Vila-Comamala, K. Jefimovs, J. Raabe, B. Kaulich, and C. David. "Silicon Fresnel zone plates for high heat load X-ray microscopy". In: *Microelectronic Engineering* 85.5-6 (2008), pp. 1241–1244.

[25] M. Lindblom, J. Reinspach, O. von Hofsten, M. Bertilson, H. M. Hertz, and A. Holmberg. "High-aspect-ratio germanium zone plates fabricated by reactive ion etching in chlorine". In: *Journal Of Vacuum Science & Technology B* 27.2 (2009), pp. L1–L3.

[26] C. David, B. Kaulich, R. Barrett, M. Salome, and J. Susini. "High-resolution lenses for sub-100 nm x-ray fluorescence microscopy". In: *Applied Physics Letters* 77.23 (2000), pp. 3851–3853.

[27] W. Chao, J. Kim, S. Rekawa, P. Fischer, and E. H. Anderson. "Demonstration of 12 nm Resolution Fresnel Zone Plate Lens based Soft X-ray Microscopy". In: *Optics Express* 17.20 (2009), pp. 17669–17677.

[28] K. Jefimovs, J. Vila-Comamala, T. Pilvi, J. Raabe, M. Ritala, and C. David. "Zone-doubling technique to produce ultrahigh-resolution x-ray optics." In: *Phys Rev Lett* 99.26 (2007), p. 264801.

[29] A. Freund. *Handbook of Optics*. Ed. by M. Bass. 2nd ed. Vol. 3. McGraw-Hill, 2001. Chap. 32, pp. 26.1–26.8.

[30] A. Snigirev and I. Snigireva. *Modern Developments in X-ray and Neutron Optics*. Ed. by A. Erko, M. Idir, T. Krist, and A. G. Michette. Springer, 2008. Chap. 17.

[31] P. Kirkpatrick and A. V. Baez. "Formation of Optical Images By X-rays". In: *Journal of the Optical Society of America* 38.9 (1948), pp. 766–774. DOI: 10.1364/JOSA.38.000766.

[32] A. Snigirev, V. Kohn, I. Snigireva, and B. Lengeler. "A compound refractive lens for focusing high-energy X-rays". In: *Nature* 384.6604 (Nov. 1996), pp. 49–51.

[33] L. Alianelli, K. J. S. Sawhney, M. K. Tiwari, I. P. Dolbnya, R. Stevens, D. W. K. Jenkins, I. M. Loader, M. C. Wilson, and A. Malik. "Germanium and silicon kinoform focusing lenses for hard x-rays". In: *Journal of Physics: Conference Series* 186.1 (Jan. 2009). DOI: 10.1088/1742-6596/186/1/012062.

[34] W. Jark, F. Perennes, and M. Matteucci. "On the feasibility of large-aperture Fresnel lenses for the microfocusing of hard X-rays". In: *Journal of Synchrotron Radiation* 13 (May 2006), pp. 239–252. DOI: 10.1107/S0909049506004936.

[35] F. Cerrina. *Handbook of Optics*. Ed. by M. Bass. 2nd ed. Vol. 3. McGraw-Hill, 2001. Chap. 27, pp. 27.1–27.5.

[36] J. Kirz and C. Jacobsen. "The history and future of X-ray microscopy". In: *Journal of Physics: Conference Series* 186.1 (Jan. 2009). DOI: 10.1088/1742-6596/186/1/012001.

[37] F. Marone, C. Hintermuumllller, S. McDonald, R. Abela, G. Mikuljan, A. Isenegger, and M. Stampanoni. "X-ray tomographic microscopy at TOMCAT". In: *Journal of Physics: Conference Series* 186.1 (Jan. 2009). DOI: 10.1088/1742-6596/186/1/012042.

[38] S. Heim, P. Guttmann, S. Rehbein, S. Werner, and G. Schneider. "Energy-tunable full-field x-ray microscopy: cryo-tomography and nano-spectroscopy with the new BESSY TXM". In: *Journal of Physics: Conference Series* 186.1 (Jan. 2009). DOI: 10.1088/1742-6596/186/1/012041.

[39] B. Kaulich, P. Thibault, A. Gianoncelli, and M. Kiskinova. "Transmission and emission x-ray microscopy: operation modes, contrast mechanisms and applications". In: *Journal of Physics - Condensed Matter* 23.8 (Mar. 2011), p. 083002. DOI: 10.1088/0953-8984/23/8/083002.

[40] H. N. Chapman, A. Barty, M. J. Bogan, S. Boutet, M. Frank, S. P. Hau-Riege, S. Marchesini, B. W. Woods, S. Bajt, H. Benner, R. A. London, E. Plonjes, M. Kuhlmann, R. Treusch, S. Dusterer, T. Tschentscher, J. R. Schneider, E. Spiller, T. Moller, C. Bostedt, M. Hoener, D. A. Shapiro, K. O. Hodgson, D. Van der Spoel, F. Burmeister, M. Bergh, C. Caleman, G. Huldt, M. M. Seibert, F. R. N. C. Maia, R. W. Lee, A. Szoke, N. Timneanu, and J. Hajdu. "Femtosecond diffractive imaging with a soft-X-ray free-electron laser". In: *Nature Physics* 2.12 (2006), pp. 839–843.

[41] J. M. Rodenburg, A. C. Hurst, A. G. Cullis, B. R. Dobson, F. Pfeiffer, O. Bunk, C. David, K. Jefimovs, and I. Johnson. "Hard-x-ray lensless imaging of extended objects". In: *Physical Review Letters* 98.3 (Jan. 2007), p. 034801. DOI: 10.1103/PhysRevLett.98.034801.

[42] M. Bertilson, O. von Hofsten, J. Thieme, M. Lindblom, A. Holmberg, P. Takman, U. Vogt, and H. Hertz. "First application experiments with the Stockholm compact soft x-ray microscope". In: *Journal of Physics: Conference Series* 186.1 (Jan. 2009). DOI: 10.1088/1742-6596/186/1/012025.

[43] A. G. Michette, S. J. Pfauntsch, A. K. Powell, T. Graf, D. Losinski, C. D. McFaul, A. Ma, G. J. Hirst, and W. Shaikh. "Progress with the King's College Laboratory scanning X-ray microscope". In: *Journal De Physique IV* 104 (Mar. 2003), pp. 123–126.

[44] M. Folkard, K. M. Prise, C. Shao, S. Gilchrist, G. Schettino, A. G. Michette, and B. Vojnovic. "Understanding radiation damage to cells using microbeams". In: *Acta Physica Polonica A* 109.3 (2006), pp. 257–264.

[45] M. Folkard, G. Schettino, B. Vojnovic, S. Gilchrist, A. G. Michette, S. J. Pfauntsch, K. M. Prise, and B. D. Michael. "A focused ultrasoft X-ray microbeam for targeting cells individually with submicrometer accuracy". In: *Radiation Research* 156.6 (2001), pp. 796–804.

Chapter 2

Microstructured Optical Arrays

2.1 Introduction

Section 1.4.2 has outlined the use of grazing incidence reflection at a surface in order to achieve a high reflectivity within a focusing optic, delivering the highest possible X-ray flux to the focused spot. The Microstructured Optical Array (MOA) has also been introduced in figure 1.4 as an optical element using grazing incidence reflection to produce focusing at soft X-ray energies. Development of MOAs has been one of the primary goals of the Smart X-ray Optics (SXO) consortium in order to produce a high intensity distribution of focused soft X-rays, with active control over the focusing characteristics. The use of double reflections from two individually controllable MOAs will have the potential to realise a highly efficient X-ray focusing device with a variable focal length.

In this chapter the focusing properties from a single reflective channel at grazing incidence will be considered, and extended to include both single and double reflections along the optical path. The single and double reflection geometries described will then be considered further in order to estimate the focusing ability of an array of similar channels. In order to highlight the potential use of MOAs for focusing of soft X-rays, the development of routines designed to simulate the

focusing properties will also be discussed. Although the principles describing focusing using combinations of either single or multiple reflections contained within an array of reflecting channels have already been widely discussed [1–6], including within publications by the SXO consortium [7, 8], the notation previously used has been slightly adapted and expanded to allow a consistent notation to be applied throughout this thesis.

The development of production techniques for MOAs is also discussed, specifically the targeted goal of creating an array of smooth-walled, planar reflecting channels in silicon, as well as the actuation of such arrays by use of piezoelectric actuators bonded to one side of the substrate. A potential use for a MOA focusing system will also be highlighted through comparison made with current microprobe geometries formed using zone plate focusing optics. The microprobe geometries described in this chapter are suitable for use in studies related to the radiation response for biological material. An X-ray source used to produce such this microprobe will be described in chapter 3.

2.2 Grazing incidence reflection properties from a single channel

To describe and simulate the overall focusing properties from an array of similar reflecting channels (which will describe the ability of MOAs to produce a focusing effect), the reflecting behaviour from a single channel must first be described. The cumulative effect from an array of channels may then be used in order to describe the overall focusing properties. The reflecting properties of a single channel may be simply described by considering the optical path through a channel from a point source, and examining the resulting intensity distribution at a detector plane, as shown in figure 2.1.

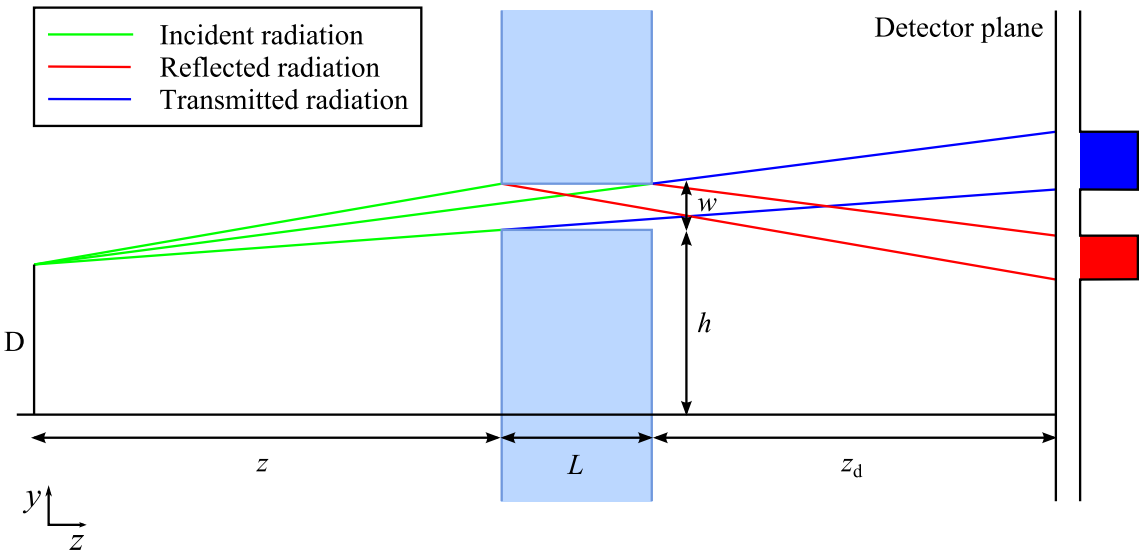

Figure 2.1: The resulting intensity distribution at a detector plane following the path of X-rays through a single channel parallel to the optical axis.

The single channel shown within figure 2.1 consists of a narrow slot of width w where material has been removed from a solid substrate of thickness L. The resulting channel contains two parallel walls perpendicular to the surface of the substrate, both of which have the potential to reflect incident X-rays at grazing incidence, as described in section 1.3.2. It shall be assumed here that X-rays will pass through the channel without attenuation, while all X-rays that do not enter the open channel are absorbed by the substrate. The only X-rays detectable beyond the substrate will therefore have to pass through the channel structure. It is initially assumed that the substrate will extend infinitely throughout a plane perpendicular to an optical axis, resulting in channel walls that are parallel to this axis. The separation between the optical axis, and the closest (*inner*) channel wall is described by the distance h. The channel wall (*outer*) redirecting X-rays back towards the optical axis is therefore at a distance $h + w$. Describing the channels in this way allows the position of the channel relative to the optical axis to be described at all times, either above or below the optical axis. For the following descriptions, it will be assumed that h is always positive, and therefore the channel is located above the optical axis.

In order to consider the X-ray distribution resulting from the reflection by a surface lying parallel to the optical axis, the separation between the source, substrate and "detector" plane (where the X-ray distribution will be described) is required. This is considered relative to an origin located at the intersection between the plane containing the source, and the optical axis. The source may then be displaced transverse to the optical axis by a distance D, allowing both axial and non-axial point sources to be considered. From the origin, the closest (*upstream*) surface of the substrate is located at a distance z along the optical axis. Beyond the *downstream* surface of the substrate, the detector plane is at a distance z_{d}.

Figure 2.1 shows the range of potential paths for a single X-ray reflection (shown in red) occurring along the outer wall of a single channel being directed back towards the optical axis. Additionally, radiation illuminating the channel at the upstream edge and missing the outer channel wall will be transmitted through the channel without reflection (blue), and will also continue to the detector plane. This results in two individual intensity distributions resulting from a single channel, the outer boundaries of which may be related to the dimensions of the channel structure. As the reflecting surface of each wall of the channel is assumed to be linear, there will be no focusing of X-rays from within a single channel. This lack of focusing results in a distribution at the detector plane that is related to the geometrical projection of the point source through the finite channel structure.

The available length of the reflecting channel surface limits the width of the intensity profiles in the plane of the detector. From this it is apparent that when reflection is possible from the full length of the channel wall (L), the corresponding width at the detector plane will be at a maximum. The available reflecting length may however be reduced by a shadowing effect, as shown in figure 2.2. Incident radiation may be blocked by the upstream surface of the substrate, and is prevented from reaching the reflecting surface, as shown in figure 2.2 region i). This

region may also block radiation transmitted through the channel without reflection. Alternatively, radiation may be blocked from reaching the detector plane by the inner channel wall, shown within region ii). Both of these effects may reduce the available reflecting length of the channel wall, for which radiation will pass through with only a single reflection. Radiation blocked within region ii) may however be reflected a second time from the inner channel wall. There may therefore be a combination of single, double (or more) reflections from within a single channel.

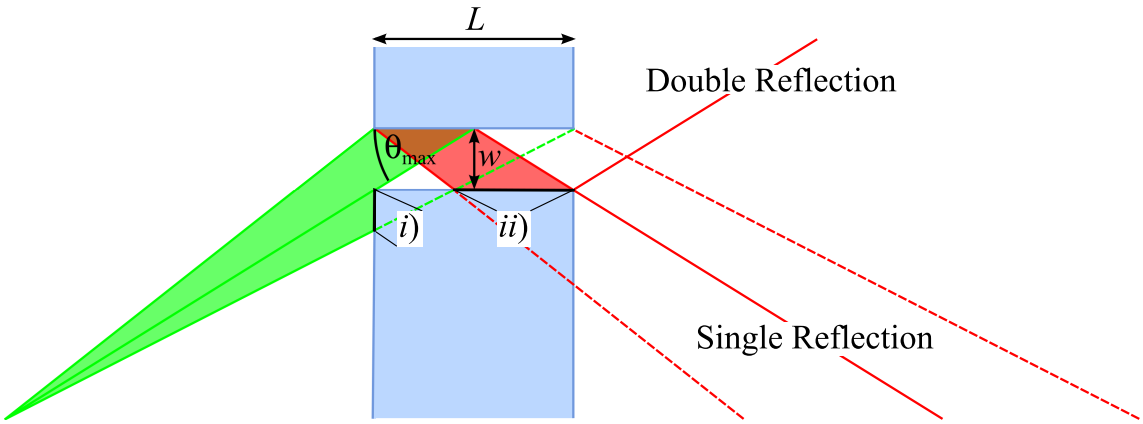

Figure 2.2: Radiation entering the channel may be blocked by the regions i) & ii), reducing the length of the available reflecting channel surface. Multiple reflections may also occur within the channel for large grazing angles.

The maximum grazing angle (θ_{max}) for which a single reflection from a channel will occur is given by equation (2.1). This maximum angle also corresponds to the minimum possible available length for the reflecting channel, beyond which no singly reflected X-rays will pass through the channel. Instead, if the grazing angle is above θ_{max}, a double reflection will occur within the channel.

$$\tan(\theta_{\mathrm{max}}) = \frac{2w}{L} \tag{2.1}$$

This maximum angle depends only on the aspect ratio of the channel structure ($\frac{w}{L}$). Taking the dimensions of a typical channel for a MOA (see section 2.5.1) as $w = 10\,\mu\mathrm{m}$, and $L = 200\,\mu\mathrm{m}$, the maximum grazing angle for which a single reflection can occur is $\theta_{\mathrm{max}} = 5.71\,^{\circ}$. The corresponding reflectivity for silicon at this

grazing angle for incident X-ray energies above 0.5 keV is $\ll 0.1$ (See Appendix A, figure A.1). Multiple reflections from within a single channel will therefore not be considered further within this chapter due to the poor reflectivity.

2.2.1 Reflection from a single, tilted channel

A grazing incidence reflection also occurs within a channel if the reflecting wall is not parallel to the optical axis. Figure 2.3 shows two potential examples of a tilted channel, with an angle $\pm\varphi$ between the channel and the optical axis. A potential X-ray path for a single reflection is also shown for each of the two examples. By assuming that the reflection will only occur at the centre of the channel, the range of possible X-ray paths reflected is reduced to a single path from a point source. It is therefore advantageous to consider a channel of negligible width and length ($w, L \to 0$), resulting in a reflection occurring at a single point a distance h from the optical axis. Clearly this simplification cannot be made to describe the overall properties for a physical MOA, however it does allow the focusing behaviour to be determined. The simplifications made will reduce both the width of the reflected distribution downstream of the substrate, and also eliminate the unreflected radiation passing through the channel as previously described. While the assumptions here are made in order to reduce the range of optical paths, a broader range of optical paths will always be visible in practice due to the dimensions of the finite channel structure. It should also be noted that in practice the shadowing effect, and multiple reflections described in section 2.2 may still occur if the grazing angle is too high, reducing the available reflecting surface for a tilted channel. It will be assumed here that this effect can also be ignored.

The angle between the optical axis and the ray incident on the channel α, and the corresponding angle for the reflected ray α' can both be related to the grazing reflection angle θ, and the angle of tilt φ applied to the channel by equation (2.2). In

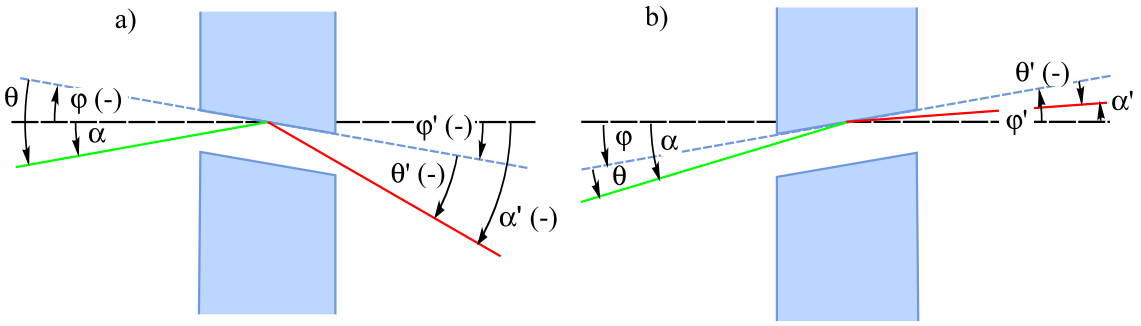

Figure 2.3: Single reflection by a channel tilted to an angle a) $-\varphi$ and b) $+\varphi$

general, an angle measured with a clockwise rotation as indicated in figure 2.3, will be described as a negative angle, while an anti-clockwise rotation is positive. This convention is applied in order to aid the description of a geometry with multiple reflections as described in section 2.4. As shown, the general description shows that all angles and distances on the downstream side of the reflection are distinguished by a superscript prime. This will also allow more complex multiple reflection systems to be shown in the future, with each reflecting element distinguished through the use of a subscript. The sign of each angle is clearly important to ensure consistency, and care must be taken to ensure the correct sign is applied.

$$\alpha = \theta + \varphi \tag{2.2a}$$

$$\alpha' = \theta' + \varphi' \tag{2.2b}$$

Application of equation (2.2) with appropriate signs to determine the angles in figure 2.3 results in a complete description, allowing both positive and negative values of α and α' to be considered. While the simplification $\varphi = \varphi'$ may always be made, it should be noted that $\theta' = -\theta$, due to the reflection. Using these two relations ($\varphi = \varphi'$, $\theta' = -\theta$), and substituting into equation 2.2, it is possible to show that

$$\alpha' = -(\alpha - \varphi) + \varphi = 2\varphi - \alpha. \tag{2.3}$$

The incident and reflected ray angles α and α' as described by equation (2.2) can be used to determine the distances (z, z') along the optical axis, where the incident and reflected rays will cross the optical axis for a given distance h of the channel from the optical axis. The distance z' here is considered to be the case of z_d, where the reflected radiation intersects the optical axis – this is required as the detector may not always be positioned at the focus of the optical element. Where the detector is positioned at this intersection, z' will always be used. Equation (2.4) describes these distances in terms of α, α' and h. It has been previously shown [8] that equation (2.4), and all subsequent equations derived from it may be simplified using small angle approximations, however these simplifications are not applied here in order to allow more general systems to be described.

$$z = \frac{h}{\tan(\alpha)} \tag{2.4a}$$

$$z' = -\frac{h}{\tan(\alpha')} \tag{2.4b}$$

A change of sign is required in equation (2.4b) in order to ensure that both z and z' are positive. This ensures that equation (2.4) still behaves as shown in figure 2.1. Figure 2.4 shows the calculated axial distance z' for channel tilt angles $-10 < \varphi < 10\,\mathrm{mrad}$, for a fixed height $h = 1\,\mathrm{mm}$, and incident source distance z.

It is possible to predict the behaviour of figure 2.4, by considering equation (2.5), derived by substituting equation (2.3) into equation (2.4b).

$$z' = \frac{-h}{\tan(2\varphi - \alpha)} \tag{2.5}$$

Considering a channel parallel to the optical axis ($\varphi = 0$) immediately shows

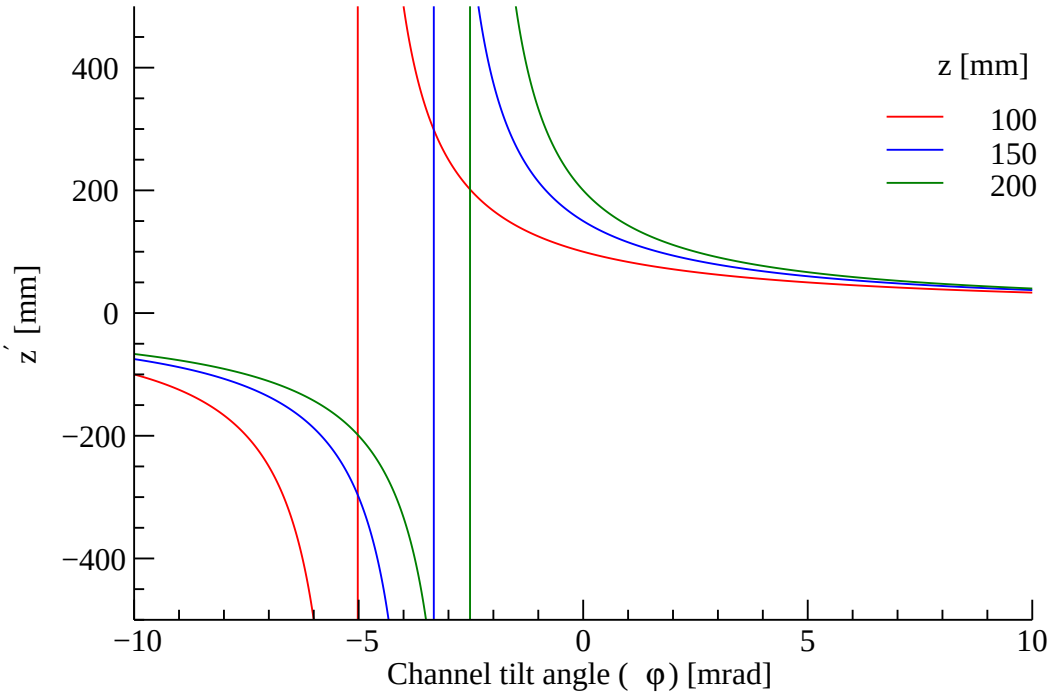

Figure 2.4: The intersection distance z' changes dramatically as the tilt angle of the channel is altered. This is shown for a constant height of $h = 1.0\,\text{mm}$, and a range of z.

that $z = z'$, as well as $\alpha = -\alpha'$. It is also apparent that $\alpha' = 0$ when $\alpha = 2\varphi$, and so z' is undefined. This corresponds to the discontinuities seen in figure 2.4. As indicated in figure 2.3 b), a positive value of α' is possible. Using equation (2.5), a negative α' indicates that $z' < 0$, and so the intersection of the radiation will be virtual, upstream of the channel.

Reflection from the tilted channel is only possible when $\theta > 0$. This may be shown considering figure 2.3. Where $\theta = 0$, there will be no change in the ray direction following "reflection", and therefore $\varphi = \alpha$. Where $\varphi > \alpha$, and therefore $\theta < 0$, the ray approaches the reflecting surface from the opposite side of the channel wall, and is absorbed before reflection.

Incident radiation may not necessarily all arrive at the reflecting channel surface from a single point source on the optical axis. It is therefore necessary to consider the intensity distribution at the detector plane obtained from non-axial sources.

This will allow light from a finite source to be described.

The light path of radiation from two individual point sources (S, S_D) initially separated by a distance D is shown in figure 2.5. Following reflection by the single tilted channel, the ray paths are separated by D' at a distance z' downstream from the channel. The distances z and z' are given by equation (2.4).

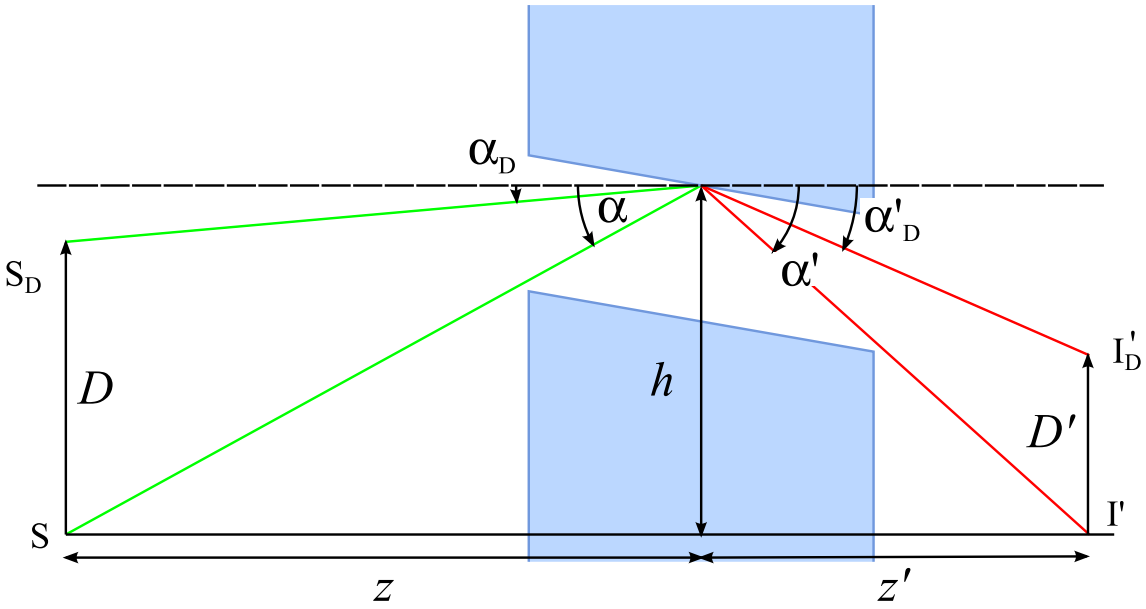

Figure 2.5: The optical path of two individual point sources through a single channel results in a variable separation D'

The separation between the two ray paths at a distance z' beyond the channel can be determined by using the constant height of the reflecting channel for each ray path, resulting in

$$h = z\tan(\theta + \varphi) \tag{2.6a}$$

$$h = -z'\tan(\theta' + \varphi) \tag{2.6b}$$

$$h - D = z\tan(\theta_D + \varphi) \tag{2.6c}$$

$$h - D' = -z'\tan(\theta'_D + \varphi) \tag{2.6d}$$

equating h between equations (2.6a), (2.6c), and (2.6b), (2.6d) results in

$$z\tan(\theta+\varphi) = z\tan(\theta_{\mathrm{D}}+\varphi) + D \tag{2.7a}$$

$$z'\tan(\theta'+\varphi) = z'\tan(\theta'_{\mathrm{D}}+\varphi) + D'. \tag{2.7b}$$

Equation (2.7) may be rearranged (using that $-\theta' = \theta$) in order to relate the separation of the point sources at the object and image planes to the axial distances along the optical axis, shown in equation (2.8).

$$\tan(\theta-\theta_{\mathrm{D}}) = \frac{D}{z} = \frac{D'}{z'} \tag{2.8}$$

Following reflection by the single channel, the two point sources, initially separated by a distance D, will have a corresponding separation D' at a distance z' downstream of the channel at the position where the incident ray from the origin will intersect the optical axis again. Equation (2.8) shows that the separation D' will be given by $\frac{Dz'}{z}$ following reflection from the single tilted channel.

2.3 Focusing properties of arrays of reflecting channels

Section 2.2 described the resulting ray path as radiation is reflected by the side wall of a single channel. This began with a qualitative description of the potential path where the channel is parallel to the optical axis, and was extended to consider the reflection from a single channel tilted with respect to the optical axis. Radiation from a point source on the optical axis a distance z from the reflecting channel will (for $\varphi < 0$) intersect the axis again a distance z' beyond the channel. A regular array of reflecting channels, each located at a different distance from the optical axis will all perform in a similar manner, potentially producing a range of different

intersection distances z', one for each channel. The cumulative effect from such an array of channels is shown in figure 2.6, where the rays reflected by each individual channel all converge at a common point. This requires the tilt angle to increase for channels further from the optical axis. The substrate containing the array of channels is assumed to be planar, and lies in a plane perpendicular to the optical axis. In order for the reflection from each channel to converge at a single point, the values of θ and φ must change systematically from one channel to the next.

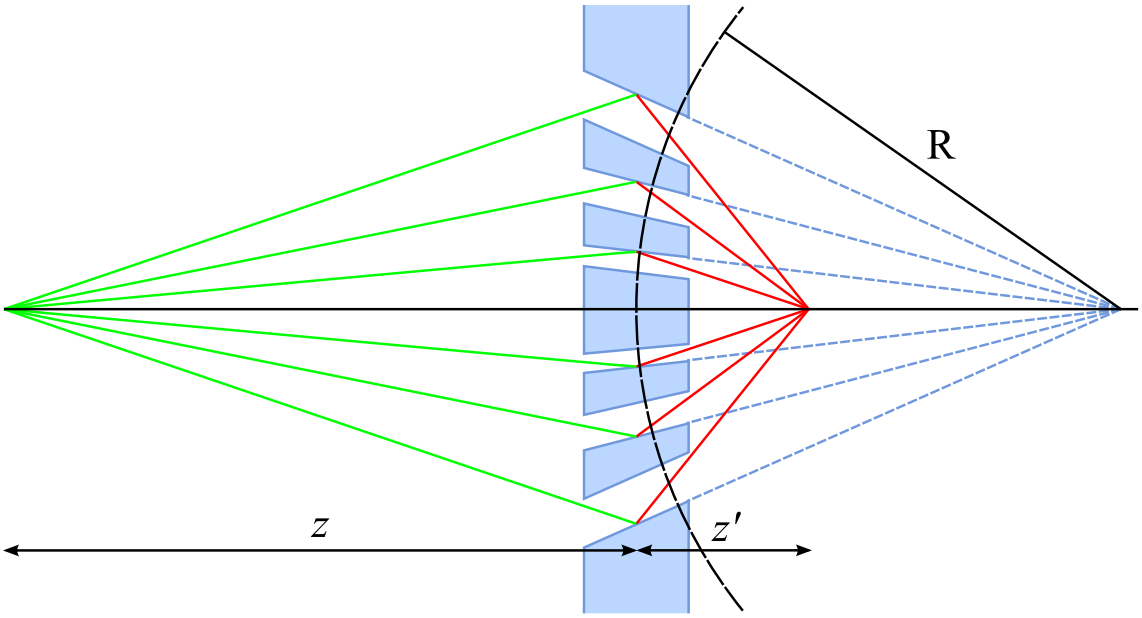

Figure 2.6: The optical path of radiation reflected by an array of channels arranged to produce a common image point by selecting appropriate tilt angles

Rearranging equation (2.4) in terms of θ and θ', using equation (2.2), results in

$$\theta = \tan^{-1}(\frac{h}{z}) - \varphi \tag{2.9a}$$

$$\theta' = -\tan^{-1}(\frac{h}{z'}) - \varphi \tag{2.9b}$$

The relation $\theta = -\theta'$ may then be used, and the resulting equations compared and simplified, leading to equation (2.10), describing the tilt angle of the reflecting surface required to create the common intersection point for any channel height h

above the optical axis.

$$\frac{1}{z'} - \frac{1}{z} = \frac{\tan(2\varphi)}{h} \tag{2.10}$$

Equation (2.10) may then be expanded using trigonometric identities, and it may be shown that,

$$\frac{1}{z'} - \frac{1}{z} = \frac{2\tan(\varphi)}{h}\left\{\frac{1}{1-\tan^2\varphi}\right\} = \frac{2}{R}\left\{\frac{1}{1-\tan^2\varphi}\right\}, \tag{2.11}$$

where R may be described as the the radius of curvature which all reflecting channels (for small φ) lie parallel to, defined by equation (2.12).

$$R = \frac{h}{\tan(\varphi)} \tag{2.12}$$

The cumulative distribution formed from the array of channels at the point of intersection z' downstream of the channel array is the focused image formed from a point source. The reflecting behaviour of a single channel described in section 2.2.1 applies to all channels of the array, and so the cumulative effect of the array is that it approximates a focusing element. The focal length f of such a channel array can be determined by elimination of φ from equation (2.4a) and (2.4b), and is shown by equation 2.13.

$$\frac{1}{z} + \frac{1}{z'} = \frac{2\tan(\theta)}{h(1-\tan^2(\theta))} = \frac{1}{f} \tag{2.13}$$

Equation (2.13) shows that an array of channels, with reflecting walls tilted will focus radiation according to the thin lens equation (1.17). The evidence allowing the array to be described as a focusing element is supported by section 2.2.1, where it has been shown that a single channel will form a virtual image (when $z' < 0$), and also collimate radiation from a point source ($\alpha' = 0$) downstream from the array at suitable values of z and φ. It has also been shown by equation (2.8) that a single channel will form a geometrically magnified image of a finite source at different

object distances. One of the more unusual properties of the entire focusing array is that the image is not inverted with respect to the source (see figure 2.5), unlike the imaging properties from more conventional (i.e. refractive) optics obeying the same thin lens equation. The ability of a single channel to produce a magnified image of a finite source following focusing may be extended to include the cumulative effect from the entire array. Although there is no direct focusing of radiation by each individual channel, it is the cumulative effect from the entire array which appears to behave as a focusing optical element.

Throughout this section, the X-rays passing through each channel have been considered to interact only with the centre of each channel wall. In practice however, the reflection may occur at any point along the reflecting length of the channel wall. This will result in a broadened distribution of X-rays at the image plane, due to a wider range of possible optical paths from each reflecting channel wall. Radiation may also pass through each channel without reflection, as described in section 2.2. For a regular array of channels with a finite reflecting length, there may be an overlap between the unreflected radiation and the reflected distribution from each channel at the image plane. In order to separate the two distributions, the introduction of a narrow region containing no channels, such as a central stop on the optical axis, will create a shadow region on the detector plane into which the reflections from each channel will fall.

Previous discussion within this chapter of the focusing properties has considered a flat plane containing both the substrate and optical axis, with all X-rays travelling within this plane. Extending the channel structure transverse to this plane will produce an array of planar reflecting surfaces. The reflection from each planar channel wall will reflect X-rays in an identical manner to that of a linear channel, however the two-dimensional distribution formed at the detector plane will change. The reflected distribution at the image plane from the planar channel structure will

now produce a focused line at the image plane. This line focus will be parallel to the extended channel structure. A complementary channel arrangement will describe channels with circular symmetry about the optical axis. This will produce a nested array of concentric cylindrical or conical reflecting surfaces, and the cumulative distribution of single reflections from each channel within the array will contribute to a point-like image from an incident point source. Such a structure may be very difficult to produce on the scale of MOAs as described in section 2.5.1.

2.4 Focusing from multiple arrays of reflecting channels

In section 2.3, the focusing properties of a reflective array were considered where only a single reflection occurs along the X-ray path. This description included an array of planar reflecting channel surfaces, producing a linear focus at the detector plane from a point source. This will be described as a 1-D focus, as the focusing effect is only apparent in a single direction. In order to describe 2-D focusing, a point-like image is required resulting from a point source. While shaping the surface of the reflecting channels towards a cylindrical or conical surface could be a method of producing 2-D focusing, allowing a single reflection to produce a point-like image at the detector plane, manufacture of such structures becomes difficult. An alternative route to producing a point-like focus uses two (or more) reflections along the X-ray path from a pair of individual planar channels to achieve a similar result. Multiple reflections along the path within a 1-D line focusing system of planar channel arrays may be used to improve and control the line focus obtained in a single dimension over that of a single reflection.

As described in section 2.3, the resulting X-ray distribution from a point source at the image plane is a focused line from an array of planar reflecting surfaces. In order

to approximate a 2-D focused spot from a point source using the focusing methods described in section 2.3, the combined distribution from two separate arrays may be used. An example of two such arrays with the planar reflecting channel walls perpendicular to each other is shown in figure 2.7. Radiation passing through the first array without reflection may be redirected back towards the optical axis by the second, and *vice versa* resulting in two perpendicular linear foci at the detector plane, with a higher intensity at the point where they intersect. It should be noted that this will be described as an optical element using more than one reflection to focus X-rays even though there is still only a single reflection along the path for each X-ray converging towards the focus spot. As there is a finite separation between the arrays (therefore $z_1 \neq z_2$), radiation may be brought to a focus at different positions for each array leading to astigmatism in the 2-D image.

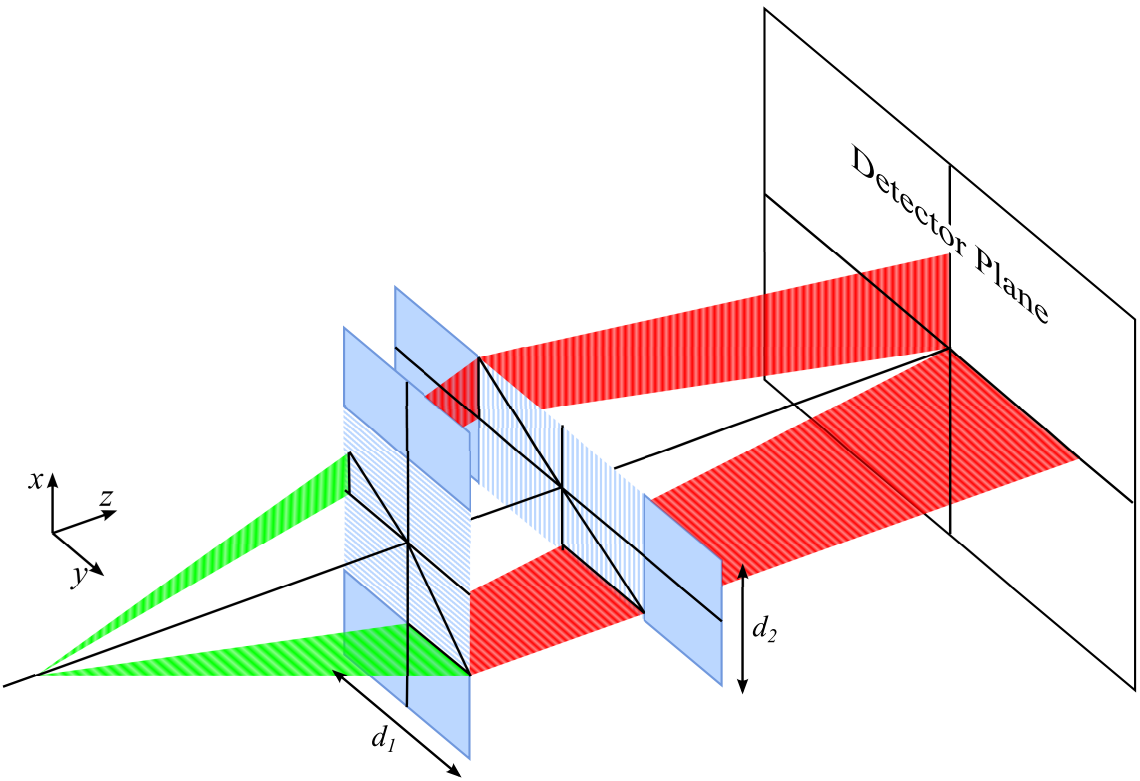

Figure 2.7: Single reflections from a pair of perpendicular channel arrays will approximate a 2-D focus spot in the region where the two linear foci intersect

For a point source located on the optical axis, the intersection of the linear foci

will also occur at the optical axis, and only ray paths lying in one of the two planes $(x,\ z)$ or $(y,\ z)$ will contribute to this spot. All other reflected radiation will be distributed within the extended line foci. A constant intensity in the focal spot will therefore be obtained regardless of the extent (shown as d in figure 2.7) of the channels as this will only define the length of the line focus obtained in the image. This focused spot may however be blocked by the central region containing no open channels. This is shown in figure 2.8, where radiation reflected within the central plane of the first array is blocked by the central stop of the second. Similarly, radiation which would pass through open channels of the first array and be reflected by the second is blocked by the central stop before reflection.

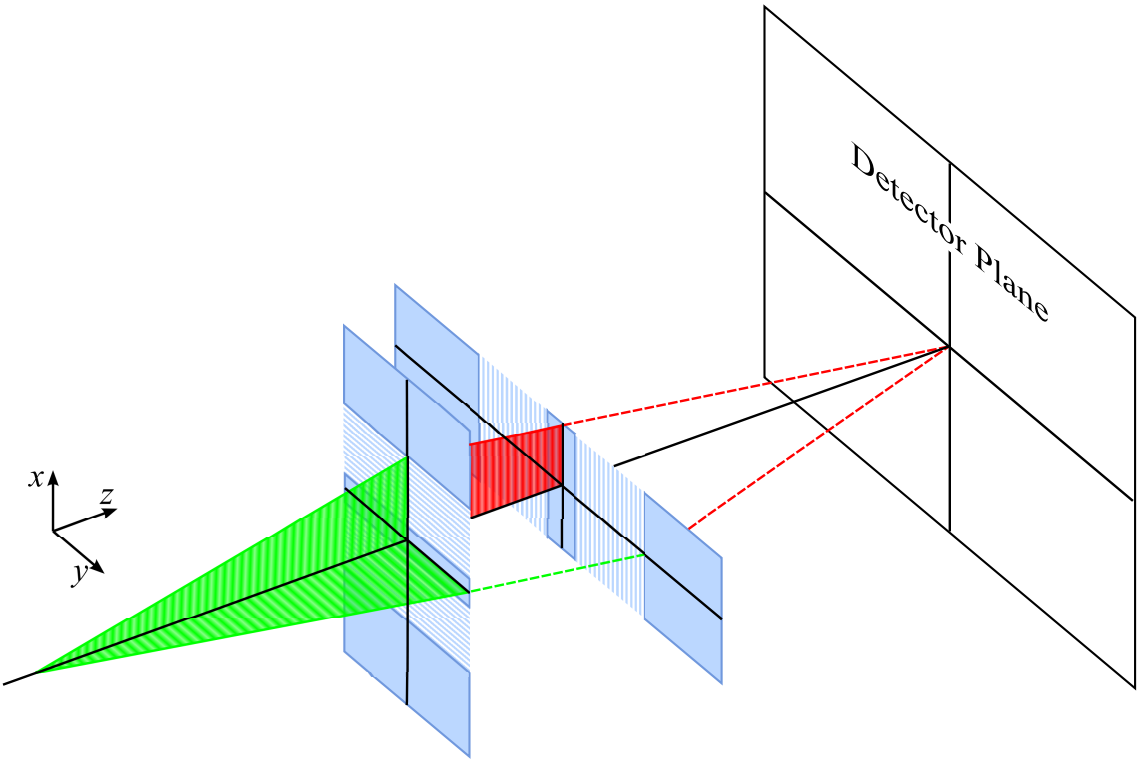

Figure 2.8: Radiation passing through a pair of arrays with a single reflection may be blocked by the central stop, preventing X-rays from reaching the focus

The predicted X-ray distribution at a detector plane resulting from a perpendicular pair of channel arrays, both containing a central stop is simulated in figure 2.9. The structure of the channels is assumed to correspond to the dimensions

of a typical MOA (see section 2.5.1) with $w = 10\,\mu\text{m}$ and $L = 200\,\mu\text{m}$. The axial position of the arrays are $z_1 = 150$ and $z_2 = 155\,\text{mm}$, with the total path along the optical axis from source to detector as 305 mm. The resulting foci produced by each array will therefore create an intensity distribution at the detector that is almost in focus from each array. This is only correct if the tilt angle is zero for each channel. The resulting X-ray distribution at the detector plane is determined by the dimensions of the array of channels, with a periodic pattern of unreflected radiation (shown in blue) throughout. The perpendicular linear foci (shown in red) from each focusing array are clearly visible in figure 2.9, in the region of the detector where the central stop shadows the unreflected radiation from each array.

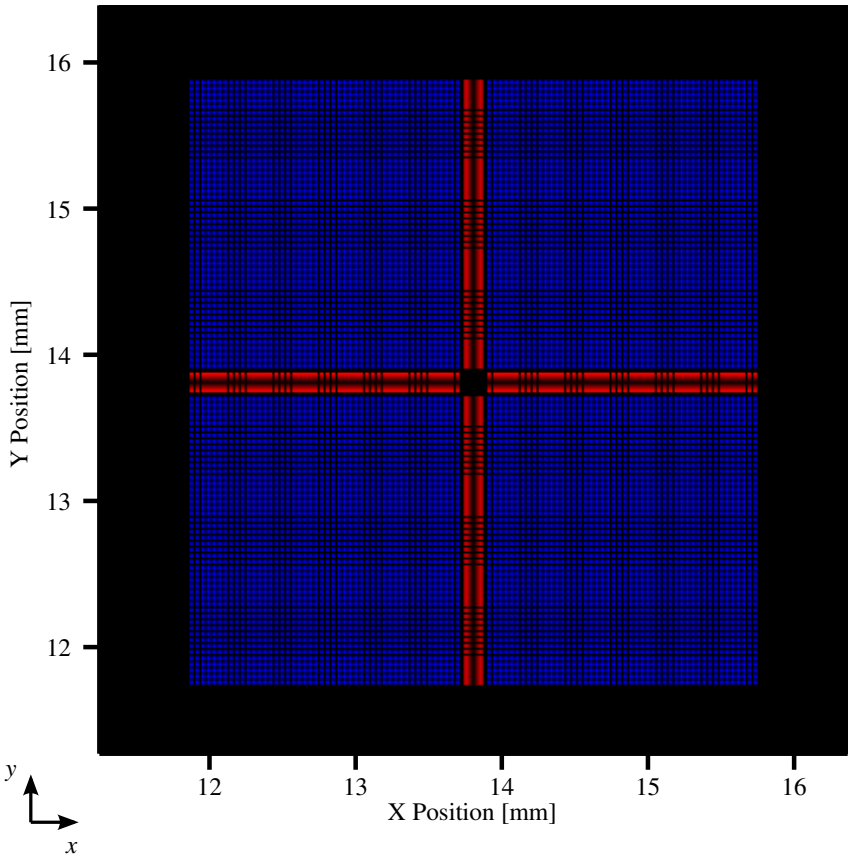

Figure 2.9: Simulated 2-dimensional intensity distribution due to a perpendicular pair of planar channel arrays. A narrow central cross (red) is formed in the shadow of the central stop from each array. The central reflected region where the foci overlap is masked by the shadow of the central stop from each array.

In order to approximate a point-like image on the optical axis using a single reflection along each optical path for an array of planar reflecting surfaces, the shadow region of the central stop needs to be modified. If the central stop is an integral feature of the substrate (as shown in figure 2.8), created as a region without a channel structure, then it cannot extend over the full extent d. If the central stop does not extend for the full extent d, reflected radiation can travel towards the focus, while still maintaining the central shadowed region. The alternative is to consider a central stop isolated from each array, achieving a similar result while still maintaining the central shadowed region.

Single reflections along the optical path are only forming an approximation to a point-like focus spot in the small region where the focus from each array overlaps. The overall 2-D image may be improved if the X-rays are reflected twice along the optical path, once by each orthogonal set of channels. This geometry will allow a 2-dimensional approximation to a focus from a point source that can be formed in the shadowed region of a central bar, as radiation will always be redirected back towards the optical axis providing there is a single reflection from each successive array, as shown in figure 2.10.

Two reflections along the X-ray path may also be used in order to improve the focusing effect for the linear focus, compared to that achieved using only a single reflection. The optical path of radiation reflected twice by two arrays of linear reflecting channels is shown in figure 2.11. In this example the first channel along the optical path is shown parallel to the optical axis. The second array further downstream from the first contains channel walls tilted towards a common point on the optical axis in a manner identical to that described in section 2.3. Radiation from a point source is brought to a common intersection point on the optical axis following reflection by each channel array pair. The reflecting channel walls for either array may be tilted independently with respect to the optical axis, with each

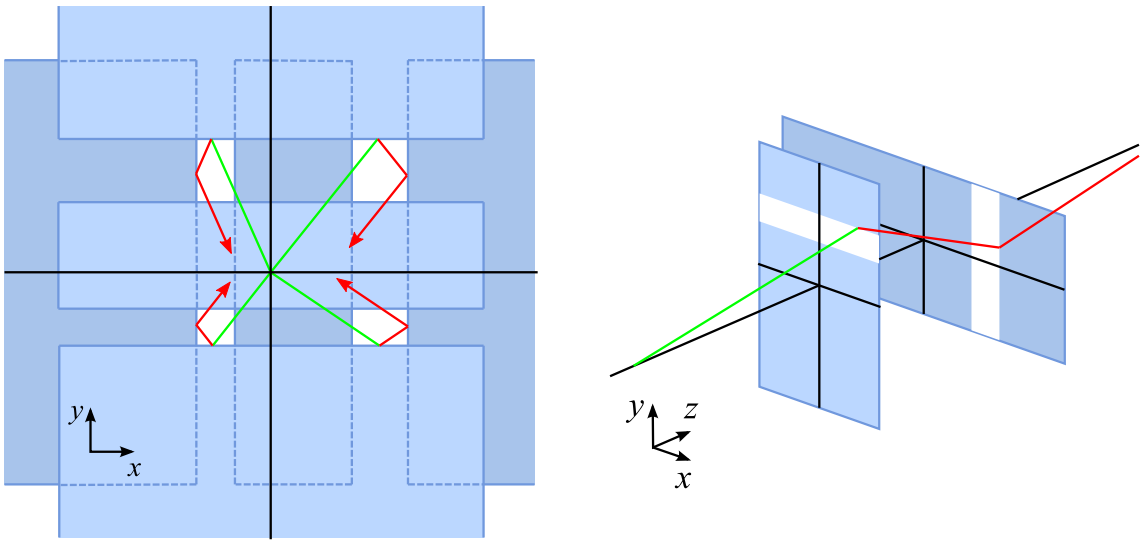

Figure 2.10: Two-dimensional focusing from a pair of planar channel arrays. Radiation reflected once by each array will approximately be redirected back towards the optical axis within the shadow of the central stop (Diagram adapted from [2])

array changing the focusing properties of the array pair.

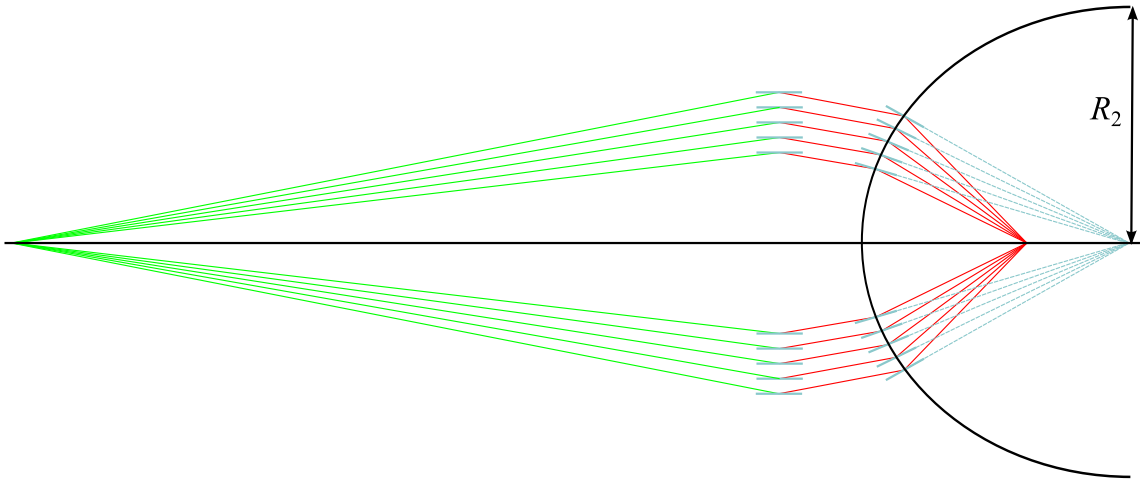

Figure 2.11: A double reflection from two parallel channel arrays may result in an enhanced focusing ability

It should be noted that while the tilt angle will alter the path of radiation passing through the pair of arrays, careful selection of the tilt angles is required in order to achieve a focused point source – radiation reflected by the first array must be reflected by the second in order to reach the focus. In order to describe the total focusing ability, the optical path of radiation reflected by a pair of channels is

described using figure 2.12. As previously described for the single reflecting array, the reflection from each channel is assumed to occur only from the centre of each channel wall.

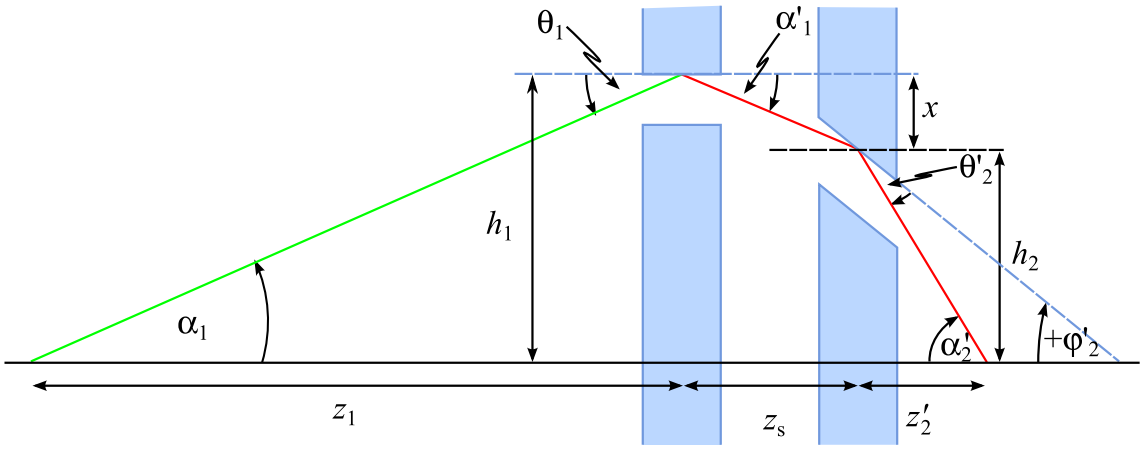

Figure 2.12: Geometry for a double reflection focusing setup

Figure 2.12 shows a potential path of radiation reflected twice through a pair of single channels. Following the notation of section 2.2.1 each channel along the optical path will be identified using a subscript: ($_1$ for the upstream channel, $_2$ for downstream). The sign convention previously applied for a single channel also applies to each channel along the optical path. In this way, the distance to each outer channel wall from the optical axis is given by h_1 and h_2 respectively. The axial separation between each of the channels is given by z_s. The angles α_1, and α'_2 will describe the angles between the incident and reflected radiation with the optical axis respectively, and can be described using equation 2.14.

$$\alpha_1 = \theta_1 + \varphi_1 \tag{2.14a}$$

$$\alpha'_2 = \theta'_2 + \varphi'_2 \tag{2.14b}$$

Both figures 2.11 and 2.12 show a potential geometry where $\varphi_1 = 0$, and therefore the channel walls of the array are parallel to the optical axis, however this need not

always be the case. As previously described for a single reflection, the intersection distances along the optical axis may be described in terms of α_1 and α_2', in an identical manner to that of the single array (equation 2.4) by

$$z_1 = \frac{h_1}{\tan(\alpha_1)} \tag{2.15a}$$

$$z_2' = -\frac{h_2}{\tan(\alpha_2')}. \tag{2.15b}$$

In addition to this, the relative heights of the two channels are linked by,

$$h_2 = h_1 + x = h_1 + z_s \tan(\alpha_1'), \tag{2.16}$$

where the distance x (as shown in the context of figure 2.12) is a negative number, due to $\alpha_1' < 0$.

Radiation reflected by the upstream channel will be incident on the downstream channel at an angle α_1' from the optical axis. Therefore, by definition

$$\alpha_1' = \alpha_2, \tag{2.17}$$

allowing the ray path to be easily predicted between each channel pair. As there are many more parameters in this optical system, defining an exact focal length (as shown for the single reflection array) becomes complicated. However as each channel along the optical path will individually focus X-rays in a predictable way, the compound system will be assumed to behave as a focusing optical element.

While the exact focal length of the compound double reflection system is difficult to calculate here, there are a number of geometries that may be realised, each with useful focusing properties, as there are clear simplifications or advantages that may be associated with the ray path. The key geometries are identified in table 2.1, along with the advantages and simplifications that may be made along the optical path.

Geometry	Description	Simplification
$\varphi_1 = 0$ or $\varphi_2 = 0$	Either upstream or downstream array has channel walls parallel to optical axis (Shown in figure 2.12)	$\alpha_1 = \theta_1$ or $\alpha_2' = \theta_2'$
$\theta_1 = \theta_2$	Equal grazing angle is obtained at each array	-
$\varphi_2' = -\varphi_1$	Radiation is parallel to the optical axis between the reflecting arrays	$\alpha_1' = \alpha_2 = 0$, $\theta_1 = \theta_2$

Table 2.1: Several unique geometries may be described for a compound double reflection system, by selecting appropriate values of φ and θ for each array

While it is possible to maintain a constant focal length by using different combinations of tilt angles for both arrays, setting $\theta_1 = \theta_2$ will result in an identical grazing incidence reflection angle along the ray path. In this way, the lowest possible grazing angle for both arrays may be obtained. While it is possible to achieve a smaller grazing angle for a single channel within the pair, the reflection angle from the other surface will always be larger. This is important in order to achieve an efficient focusing optic, where a high reflectivity is required towards the outer edge of the optical element where the grazing angle is largest.

2.4.1 Comparison between single and double reflection focusing arrays

There are several advantages which may arise from the use of a double reflection from a pair of channel arrays instead of only a single reflection. As previously described in section 2.4, the main advantage gained through use of a double reflection from an orthogonal pair of channel arrays (such as that outlined in figure 2.10) is to approximate a 2-D focus spot from a point source. While this result is also possible using either a single or double reflection system with rotational symmetry about the optical axis (for example from the cylindrical channels described in section 2.3), the

production of such arrays is technically very challenging.

There are also a number of advantages in using a double reflection along the optical path in order to produce a linear focus (such as that shown in figure 2.11). In order to highlight this, comparison between single and double reflection geometries with a comparable focal length is required. This requires identical distances to both the upstream (entry) and downstream (exit) surfaces of the channel array, and so $z_1 = z$, $z_2' = z'$. The height of the entry channel above the optical axis is also assumed to be the same for the single and double reflection ($h_1 = h$). As the focal length is fixed, the total change in the angle between entry and exit paths of the ray entering a channel at a height h in either system must also be approximately constant, as shown in figure 2.13.

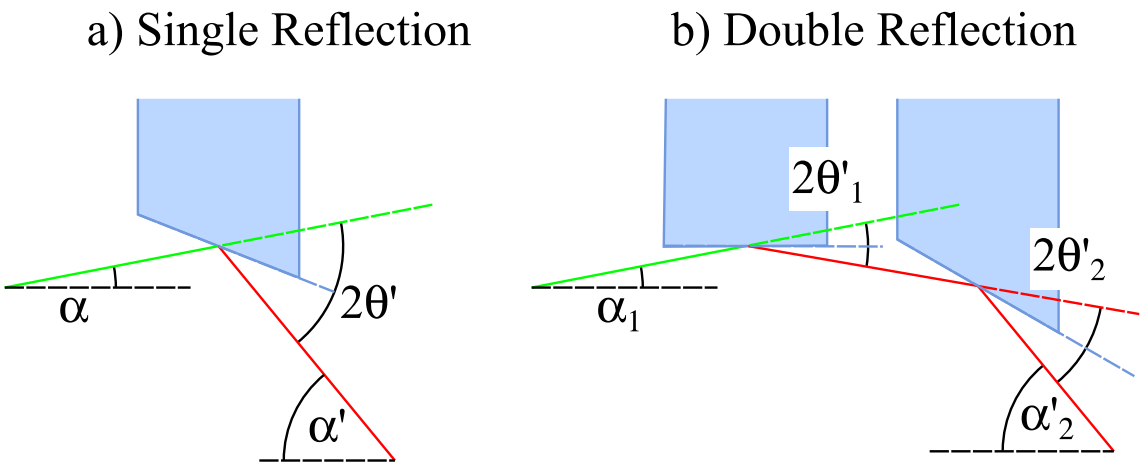

Figure 2.13: The overall angular change due to the reflection(s) must be approximately constant between a single and double reflection channel system with a comparable focal length.

It follows from figure 2.13 that the grazing angle for either reflection within the double channel system must be smaller than that for a single reflection. This means that the critical grazing angle θ_c will occur at a larger distance from the optical axis, potentially resulting in a much wider active area able to reflect X-rays to the focus effectively. This effect must be greatest when the grazing angle is the same for each array as described in table 2.1, creating the largest possible active area for

the overall channel array.

Where the full reflecting length of the channels is used to produce the X-ray distribution, the X-ray path from the source to the focused spot depends on the position of the reflecting point within the channel. This will result in a slight change in the performance of the single channel, as the magnification will differ slightly for reflections occurring along the length of the channel. This unequal path length is described by an aberration known as coma, and becomes large for grazing incidence reflective optics. Coma may however be reduced by using a double reflection, as the Abbe sine condition, shown in equation (2.18) [9], is approximately satisfied across each channel within the array.

$$\frac{\sin(\alpha)}{\sin(\alpha')} = \text{constant} \tag{2.18}$$

2.5 Development of active X-ray optics

Microstructured Optical Arrays were investigated by the SXO consortium, using either single or double reflections at grazing incidence along the X-ray beam path in order to produce a focusing effect for soft X-rays. The behaviour of the reflective channel arrays described in sections 2.3 and 2.4 are therefore appropriate for describing the focusing properties of MOAs. One of the concepts developed and applied to MOAs by the SXO consortium involved bonding piezoelectric strips to the surface of an array of reflecting channels, achieving active control of the curvature, hence the focusing properties of the array. The application of these piezoelectric strips is described in section 2.5.2.

Development of MOAs has concentrated on producing an array of parallel channel walls with a low surface roughness, allowing a uniform high reflectivity to be achieved from each reflective surface. In addition to this, extensive Finite Element Analysis (FEA) modelling has been applied in order to develop an actuator layout

allowing a suitable curvature to be applied to the substrate, providing an optical element with a useful focal length. Progress with each of these has been previously presented elsewhere [8, 10, 11], and will be summarised in sections 2.5.1 and 2.5.2. The optical characterisation of each of these generations will be described further in chapter 4.

2.5.1 High aspect ratio silicon etching – a method for producing MOAs

The initial design target for producing a MOA channel structure was to generate an array of narrow channels through a thin ($\sim 200\,\mu m$) substrate. Producing an array of parallel channel walls within a thin substrate allows the surface (and therefore the channels) to be actuated repeatably using the piezoelectric devices bonded to the surface.

Structures have been successfully produced by etching a regular array of channels of width $w \simeq 10\,\mu m$ through a silicon substrate, in a square active area of $2\,mm \times 2\,mm$. It is essential that the channel walls are parallel following production, allowing the reflections from each channel to contribute to a common focused spot. The initial approach (first generation) to produce such a channel structure used the Bosch process [12, 13], creating a periodic array of planar channel walls. Material is removed from an unmasked region of the substrate in this Deep Reactive Ion Etch (DRIE) process by exposure to a plasma formed from a mixture of SF_6 and O_2 gas. Following removal of the substrate material a polymer layer (of C_4F_8) is deposited. This layer prevents etching of the channel side walls in the subsequent etch, while allowing material to be removed from the base of the channel. Highly anisotropic etching deep into the silicon substrate is therefore possible by repeatedly removing material from the base of the channel, with the passivation layer preventing the channel from becoming significantly wider.

A typical first generation MOA channel structure is shown within figure 2.14. Analysis of the surface of the reflecting channel walls of this structure shows that there is a significant long range periodicity along the walls of the channel in the reflecting surface of the channel walls due to the cyclical steps of the Bosch process. Despite optimisation of the processing techniques, the lowest roughness achieved for MOA channels using the Bosch process has been 8 nm [14]. This is however contained within a region close to the top of a channel (in the direction along which the channel is etched), and the surface roughness increases significantly towards the bottom of the etch channel. In order to achieve a high reflectivity with minimal X-ray scattering from the channel walls, a target roughness for the surface has been selected as 2 nm RMS. As the roughness achievable using the Bosch process is larger than this, an alternative method of production was proposed (second generation).

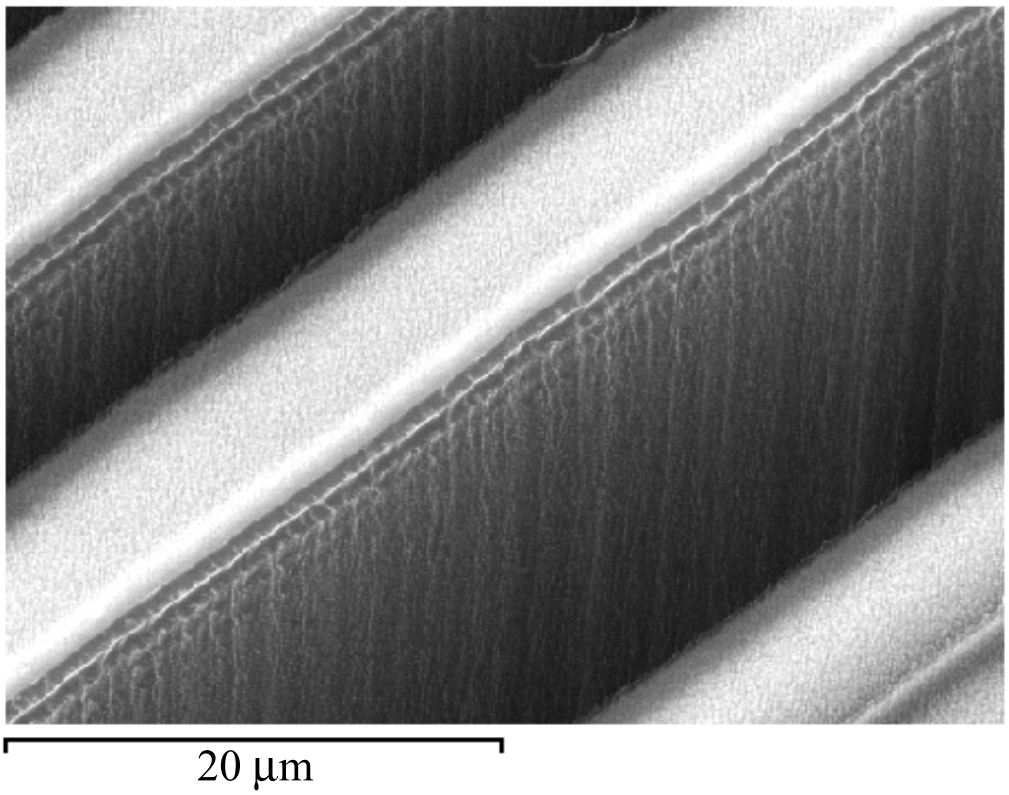

Figure 2.14: An example of a high aspect ratio first generation channel structure fabricated using the Bosch process. The SEM image shows the top of the channel, with a long range "rib" structure visible down the length of the channel.

This alternative method to produce MOA channel structures uses TetraMethylAmmonium Hydroxide (TMAH) etching [15] to etch through the silicon substrate with an extremely high anisotropy. The wet chemical-etching process used has a high degree of anisotropy in the etch rate between the [110] and [111] directions in bulk silicon. This has the advantage of producing extremely low roughness ($\sim 1.5\,\mathrm{nm}$), parallel walls for the reflecting surface, and has been adopted as a viable route for producing MOA channels. A typical channel structure created from a TMAH etch is shown in figure 2.15.

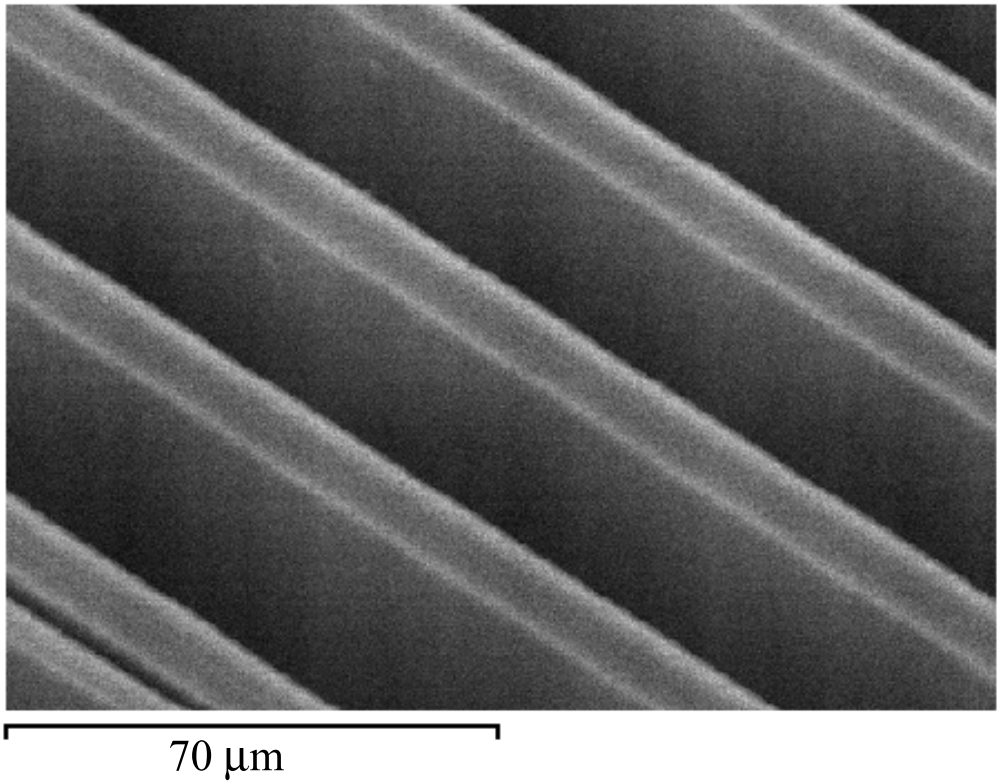

Figure 2.15: An example of a high aspect ratio second generation MOA structure fabricated using TMAH chemical etching.

2.5.2 Actuation methods for MOAs

As previously described in section 2.5, active control of the focusing properties of a MOA may be achieved by actuating the substrate, tilting each channel wall with

respect to the optical axis. Creating uniform curvature across the surface of the substrate will result in tilt angles that are described approximately by equation (2.12). The actuation methods used in order to deform the surface of the substrate lead to a slight distortion of the channels as well as changing the tilt angles – the centre of the reflecting surfaces do not lie at equal distances along the optical axis. This effect is however small compared to both the total thickness of the substrate and aperture of the MOA, and so will be neglected.

The use of piezoelectric actuators bonded to the surface of the substrate provides a compact solution, while allowing control of the focal length *in situ*. The initial design of the piezoelectric actuator layout is shown in figure 2.16, showing strips of piezoelectric actuators bonded either side of the active region containing the X-ray reflecting channels. Such an actuator layout may be applied to both the first and second generations of MOAs. In order to provide a useful focal length for a double reflection MOA, using only a single actuated MOA, a radius of $R \simeq 50$ mm has been identified, resulting in a focusing element with an effective focal length of $f \approx 24$ mm. Application of the initial simple piezoelectric actuator scheme to an array results in a minimum experimentally measured radius of $R = 420$ mm [16] for a 200 µm thick silicon substrate.

In order to actuate an MOA to achieve the smaller target radius of curvature, a novel actuator and substrate design has been developed – the "spider" array [10]. This design (third generation) increases the curvature within the active area along an array of lever-like structures patterned into the silicon substrate. Actuation of the substrate is still required on either side of the active area to generate the curvature, however there is far less demand on the edges of the substrate where the actuators are positioned, to achieve the smallest radius of curvature possible. For example, mechanical deformation of the outer edges of a spider MOA of thickness 100 µm to a 250 mm radius of curvature at the outer edges of the substrate results in a measured

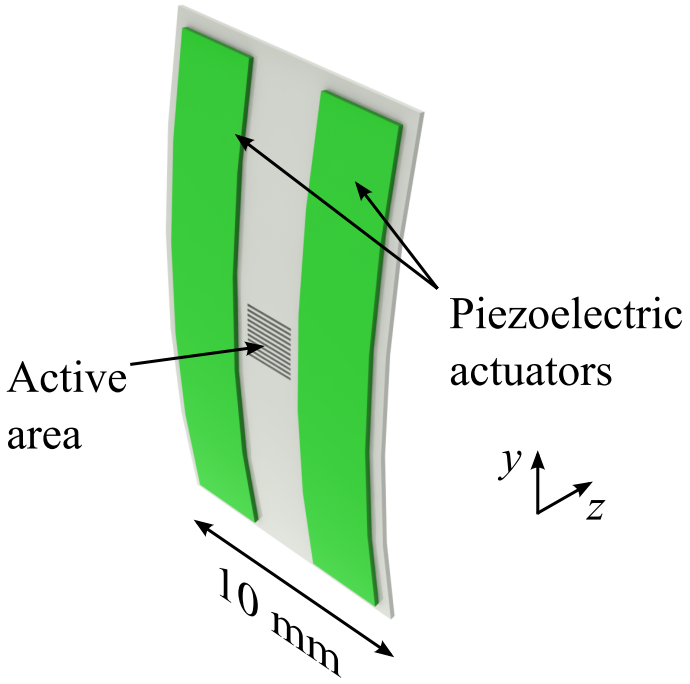

Figure 2.16: Actuation of a single MOA, showing a simple piezoelectric actuator layout.

value of $R = 30\,\text{mm}$ across the active area, well below the previously defined target.

The design of the lever arms for the spider actuator began as a series of radial spokes, radiating from the active area. While it is possible to fabricate such a structure, more complex processing is required, using both chemical (TMAH) and DRIE (Bosch) etching techniques, to ensure smooth channel walls along with the production of the radial spokes. This design has since been modified to use only TMAH chemical etching by creating the levers that run either parallel with the channels, or at an angle of 70.53°, corresponding to the {111} planes of silicon. This new design is shown in figure 2.17, and has been experimentally shown [10] using piezoelectric actuators to achieve a smallest radius of $R = 47\,\text{mm}$ within the active area.

Additional flexibility may be added to the spider array by dividing the piezoelectric actuators into many different segments, with individual control over each segment. This allows fine control of the tilt of each reflecting channel within the array. It is estimated that this may provide additional fine control over the

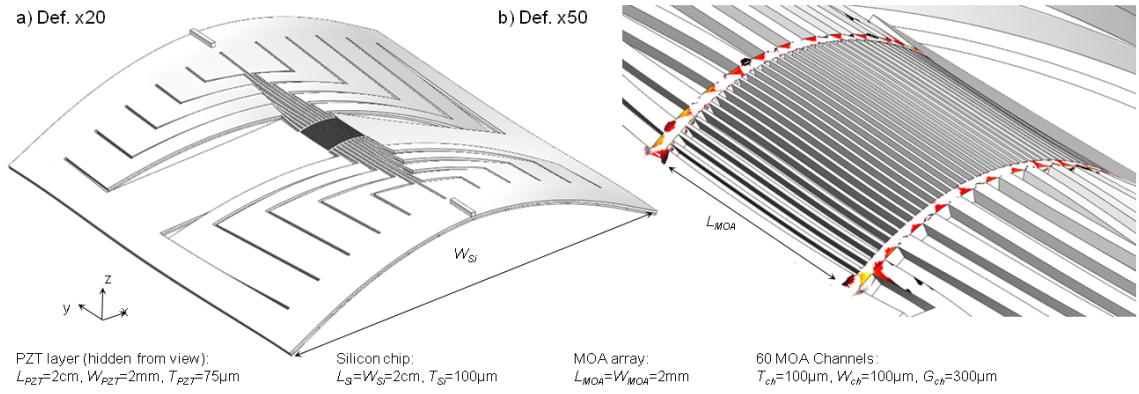

Figure 2.17: The radius of curvature of the active area of a MOA is enhanced through the use of a "spider", or lever-like arms within the substrate. *Image reproduced from* [16]

aberrations present in the focused image.

The spider arrays have also been incorporated into a surrounding package [10], allowing protection of the fragile substrate, while supporting and enabling actuation of the array. This package includes mounting points compatible with the sample manipulator described in chapter 3, allowing characterisation of the actuated arrays to be performed in the future.

2.6 Comparison of MOAs to existing X-ray optics

As mentioned in section 1.4.2 Microstructured Optical Arrays are not the only optical element to use grazing incidence reflections in order to produce focusing of soft X-rays. A range of optical devices has been developed for use in both laboratory, and large (astronomical) scale applications. A brief review of this current technology follows, with comparison to MOAs made where appropriate. As each optical element described will contain similarities to MOAs, it will be possible to describe the focusing properties for them using the description given in sections 2.2 to 2.4.

Micro-Channel Plate (MCP) optics

One of the more directly comparable optical elements to MOAs uses Micro-Channel Plates (MCPs) to achieve X-ray focusing. These use reflections from a large array of formed pores or holes in a plane transverse to the optical axis, which may be shown to focus in an identical way to a single channel. Focusing of soft X-rays has been demonstrated for both square [2] and circular [3] arrays of pores, using combinations of both single and double reflections to approximate 2-D focusing. The length of the reflecting channel structure (L) in each case is generally a few millimetres thick, far thicker than MOA structures, with typical channel widths of $w \simeq 10\,\mathrm{mm}$. Focusing using MCPs with tilted channels has also been considered, where the curvature of the substrate is created by slump-forming a parallel-channel square or circular pore MCP to a defined curvature.

Square MCP focusing optics

The square MCP-type optics investigated will behave in an identical manner to the double reflection channel pair previously described by figure 2.10, with a single reflection from each orthogonal surface contributing to the focus spot. In this description however, the orthogonal channels are overlapping within the same plane ($z_\mathrm{s} = 0$), and so reflection is possible from either channel wall.

Circular MCP focusing optics

While the reflecting channels of a MOA are currently produced as an array of planar channels limiting the focusing effect due to a single reflection to 1-D, an MCP consisting of array of circular pores will automatically approximate a point-like image. This is due to the outer reflecting surface always redirecting radiation radially back towards the optical axis. In addition to this, the reflecting surface of each pore will also behave as a cylindrical lens, with the circular profile of the pore creating a

further focusing effect of radiation from each channel.

The Multi-Foil Optic (MFO)

Focusing from an array of channel-like structures may also be achieved by reflection from shaped surfaces [4, 17], where the double reflection from a pair of orthogonal, elliptical mirror arrays reflect EUV radiation towards a common focus. The channel arrays in this example are constructed from segments of gold coated glass producing a Multi-Foil Optic (MFO), and may be considered to be a similar technology to a MOA. The MFO is however is contained within a much larger and more complex structure, and the shaped channels define a fixed focal length for the optic.

Lobster-eye optics

The use of grazing incidence reflective arrays are not limited to laboratory applications; there is significant interest in such reflecting structures for astronomical use due to the potentially large apertures that may be achieved, collecting more radiation into the focused image. Such lenses, typically referred to as "lobster-eye" optics [18] are again significantly larger than the dimensions of a MOA. There has also been interest in producing arrays of channels in silicon [19, 20] for lobster-eye optics, using either electrochemical, or chemical etching to produce the focusing arrays.

Alternative focusing optics

Each of the grazing incidence reflection optics discussed so far has considered single reflections from orthogonal planes to produce 2-D focusing of X-ray radiation, in a similar manner to that shown in figure 2.10. Comparison may also be made between the focusing properties from a reflective channel pair with Wolter optics and polycapillary optics where many reflections occur along the X-ray path. This

is shown in figure 2.18, where focusing from a type I Wolter microscope [1] is shown to behave in a similar manner to a pair of channels with appropriate tilt. While a Wolter microscope optic contains a continuous curved surface, the channels approximate the surface with short linear segments. The resulting distribution from the channels may be slightly broader at the detector plane. The description given for reflecting channels may also be extended to consider multiple reflections along the optical path, and used to describe polycapillary X-ray optics, again by approximating the continuous curved surface by short linear segments.

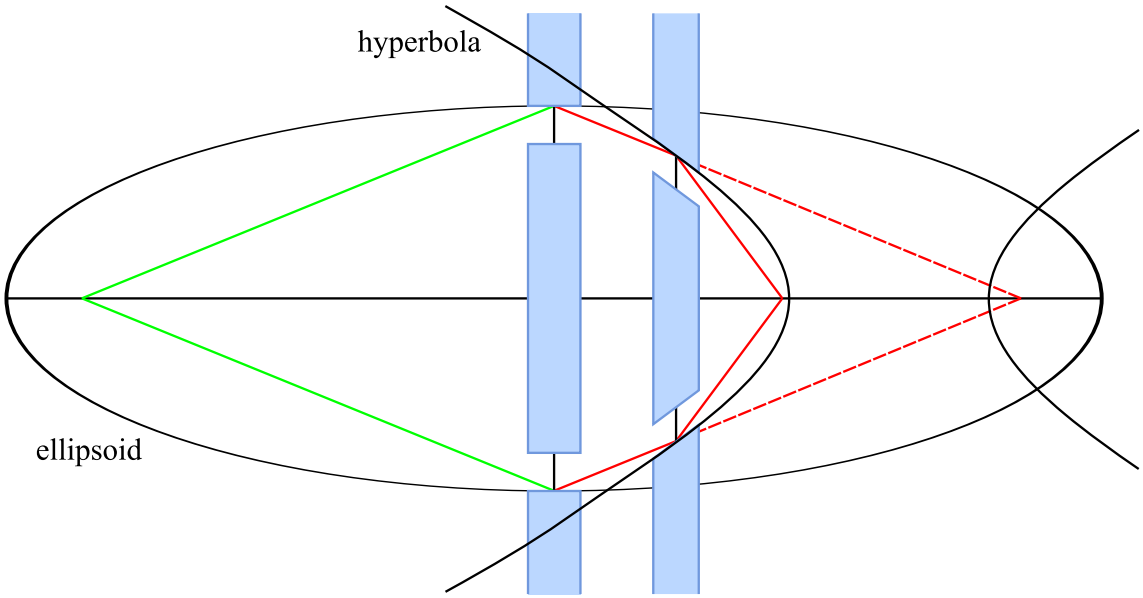

Figure 2.18: The focusing ability from a pair of reflecting channels may be used to approximate a Wolter microscope, within a small region.

While the descriptions within sections 2.2 to 2.4 may be used to describe the focusing effect from MOAs both in single and double reflections it is also applicable to many different reflective optics, particularly using grazing incidence reflection. These additional optics however generally consist of much longer reflecting surfaces, and often may allow a much larger aperture to be used. One potential advantage of the MOA however is the adaptive control of the focal length, achieved by bending the thin substrate, and the control of aberrations when using multiple reflections along the optical path (section 2.4.1).

2.6.1 Comparison of MOAs to diffractive optics

One of the primary applications for a MOA is for use within a soft X-ray microprobe, creating a high intensity focused spot of X-rays. In order to assess the advantages gained through the use of MOAs, comparison will be made between the focusing properties of a zone plate and a MOA within the microprobe geometry, for a range of incident radiation energies. For the following example the focal length for each optical element described is constant, allowing a comparison to be made between the focusing properties. A constant source to optic distance (z) of 160 mm, typical of current microprobe experiments will also be used [21].

The soft X-ray microprobe used for radiobiological experiments at GCI focuses radiation from an electron bombardment source to a small spot using the zone plate described in table 2.2. Although the microprobe was initially used with C K radiation, its use has since been extended [22] to include a range of different target materials, allowing higher (and therefore more penetrating to cellular material) energy X-rays to be produced. For the same zone plate, of diameter $D = 200\,\mu\text{m}$, and outermost zone width of $d_\text{n} = 100\,\text{nm}$, there is a large variation in the focal length as the incident radiation energy is increased.

Table 2.2: Focusing properties of a zone plate for a range of incident X-ray energies.

Characteristic emission	C K (0.277 keV)	Al K_α (1.487 keV)	Ti K_α (4.511 keV)
First order focal length (f) [mm]	4.5	24.0	73.0
z' [mm]	4.6	28.2	133.5
Geometric magnification ($\frac{z'}{z}$)	0.03	0.18	0.83

The downstream distance from the zone plate to the focused spot of the microprobe (z') will increase with the energy in the region where the geometric magnification of the source remains below 1 ($z > 2f$). The requirement of the

microprobe to position the sample at the focus of the X-rays results in a large range of travel of a manipulation stage required in order to cover this distance. There is also a significant difference in the geometric magnification of the source due to the change in focal length at different energies. While the focal length may be kept approximately constant at different energies by replacing the zone plate for one either with a different diameter or outer zone width, this will result in a complicated procedure to change the X-ray source energy – the zone plate and target will both require changing and alignment.

The above description assumes the zone plate is illuminated by a monochromatic source of X-rays, corresponding to the characteristic emission line of the target material. The zone plates used within the microprobe will however suffer from chromatic aberration, both due to the finite width of the characteristic lines, and also due to the bremsstrahlung emitted from the X-ray source. This chromatic aberration results in a different focal length for each energy contained within the spectra, and the first order radiation focused by the zone plate will be spread across the optical axis. In order to achieve a small focused spot using a zone plate, monochromatic radiation from a single diffraction order is therefore required. This was achieved within the microprobe using a grazing incidence reflection from a planar silica mirror to remove high energy bremsstrahlung. An aperture positioned between the zone plate and focused microprobe was also used to remove the unwanted high orders of diffraction.

As the reflectivity at grazing incidence from a MOA channel remains constant for all incident X-rays below the critical angle, there is no requirement to provide a monochromatic source in order to produce a microprobe. The focal length will be constant for all incident energies, and all radiation reflected below the critical angle will be re-directed towards a common focus. This will eliminate the need to position the sample at different axial distances, and also ensure a consistent

geometric magnification of the source for different X-ray energies. It may also increase the available flux of X-rays used within the microprobe through the use of a polychromatic source. The overall outer aperture available to efficiently reflect X-rays will however depend on the incident energy, as the critical angle is smaller for higher energy X-rays. As the angle decreases with increasing X-ray energy, the aperture may be reduced for high energy X-rays.

The focusing properties for both single and double reflection MOAs with a common focal length of 23.99 mm (corresponding to the first order focal length of the microprobe zone plate at Al K_α) are summarised in table 2.3. In each example shown, the distance z is assumed to be 160 mm, with the optical path passing through the outermost channel of an array at a distance $h = 1\,\text{mm}$ from the optical axis. Where a double reflection is described, the axial separation between the two channels is assumed to be $z_s = 1\,\text{mm}$, resulting in $h_1 \approx h_2$. Also the axial deflection due to the curvature of the MOA is assumed to be negligible, and so reflection from the upstream channel occurs at a distance z_1 along the optical axis, with the radius R described for each channel by equation (2.12).

It can be seen from table 2.3 that both single and double reflection MOA configurations are suitable for use within a microprobe providing at least one of the channel arrays can be actuated to below $R = 100\,\text{mm}$. It is shown that the smallest radius of curvature of a single MOA is required for the geometry where $\theta_1 = \theta_2$, and so producing the largest reflecting aperture (due to the lowest grazing angle at the outer edge of the active area) will be the most demanding on the actuator. The requirement for a small radius R is relaxed if both MOA substrates are actuated. Such a configuration results in $\alpha_1' > 0$, a result not observed in any of the other configurations. This setup does however result in the largest grazing angle (for the second array), within a double reflection MOA focusing system.

This small value of R may also be relaxed by allowing a longer focal length to be

Table 2.3: Summary of MOA parameters required to define an optical element with $f = 23.99\,\text{mm}$, using both single and double reflection geometries.

Parameter	Single Reflection	Double reflection ($\varphi_1 = 0$)	Double reflection ($\theta_1 = \theta_2$)	Opposite tilt ($+\varphi_1$, $-\varphi_2$)
		Distances [mm]		
z_1	160.00	160.00	160.00	160.00
z_2'	(z_1') 28.22	28.22	28.22	28.22
z_s	N/A	1.00	1.00	1.00
h_1	1.00	1.00	1.00	1.00
h_2	N/A	0.99	0.99	1.00
		Angles [deg.]		
α_1	0.36	0.36	0.36	0.36
$\alpha_1' = \alpha_2$	-2.03	-0.36	-0.84	0.10
α_2'	N/A	-2.02	-2.00	2.03
θ_1	1.19	0.36	0.60	0.13
θ_2	-N/A	0.83	0.60	1.07
φ_1	-0.84	0.00	-0.24	0.23
φ_2	N/A	-1.19	-1.43	-0.97
		Radius of Curvature [mm]		
R_1	68.56	∞	239.93	-250.00
R_2	N/A	47.94	39.40	59.39

considered, as a smaller tilt angle φ reflects radiation further from the optical axis. While the grazing angle θ may be close to the critical angle for an energy of 1.487 keV (Al K_α), this is calculated for the outer edge of the MOA. The grazing angles will be reduced for reflections occurring closer to the optical axis. If the grazing angle at the outer edge of the MOA is above the critical angle, only the X-ray reflectivity changes – the axial location of the focus spot will remain unchanged.

One of the requirements for a useful microprobe is the ability to produce a high flux of X-rays at the focus. A simple estimate of the performance of a single reflection MOA and a zone plate now follows. This may be used to compare the

X-ray flux redirected into the focused spot of the microprobe. Figure 2.19 highlights the method used in order to estimate the X-ray flux for both a MOA a), and a zone plate b).

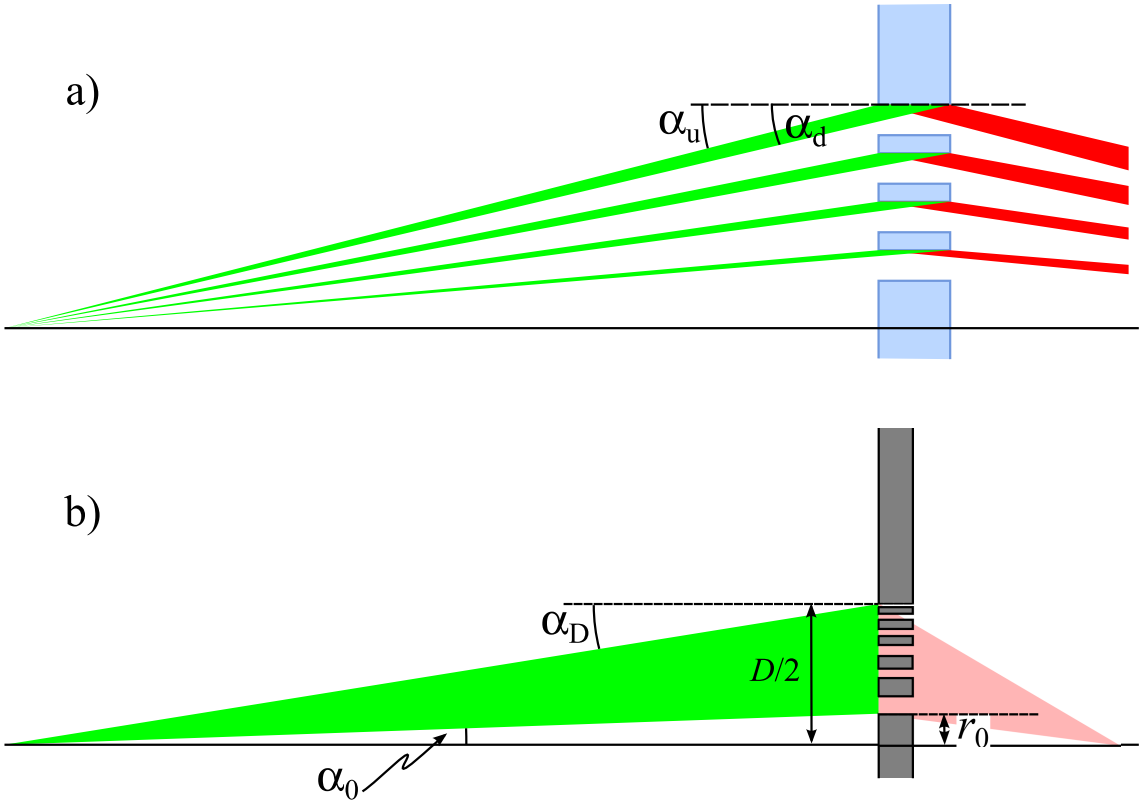

Figure 2.19: Schematic showing the solid angle for a) a single reflection MOA and b) a zone plate. This solid angle may be used to compare the ability of different optical elements to efficiently focus X-rays.

Regions where incident X-rays may be focused are represented for each of the optical elements by the colour green in figure 2.19. For the MOA, this depends on the angular range falling on the reflecting surface of each channel (shown for the outermost channel as $\alpha_u - \alpha_d$), while for the zone plate the total area of the zones is considered to contribute to the focused spot, and may be calculated by $\alpha_D - \alpha_0$. Assuming a constant flux of X-rays falls uniformly over the active area of each of the optical elements, the focused X-ray flux redirected towards the focus will depend on the total solid angle (indicated by the green regions) combined with a focusing efficiency, potentially reducing the X-ray flux reaching the focus spot.

There are assumptions made within the model described, used in order to better highlight the comparisons made. For example, the diffraction efficiency of the zone plate is assumed to be given by equation (1.20) (i.e. there are no phase effects). The reflectivity of the channels is also assumed to be perfect, and therefore all X-rays incident on a MOA channel will be re-redirected towards the focus. Table 2.4 shows the total solid angle for the zone plate described for the microprobe at the beginning of this section ($D = 200\,\mu\text{m}$, $d_\text{n} = 100\,\text{nm}$). The corresponding solid angle calculated for both an actuated and unactuated MOA, each using a single reflection, are shown. The actuated MOA is selected in order to achieve a focal length of 23.99 mm (as shown in table 2.3), the same as the zone plate. Each optical element is positioned a distance $z = 160\,\text{mm}$ from the source. Finally, a zone plate with a diameter matched to the active area of the MOA is presented. This therefore means that the large diameter zone plate and actuated MOA have the same numerical aperture, and are therefore directly comparable.

	Zone Plate ($D = 100\,\mu\text{m}$)	MOA (untilted)	MOA ($f = 23.99\,\text{mm}$)	ZP ($D = 2.00\,\text{mm}$)
Solid angle [mrad]	0.55	0.10	0.34	5.54
Efficiency	0.1	1.0	1.0	0.1
Solid angle $\times$ efficiency	0.06	0.10	0.34	0.55

Table 2.4: Summary of X-ray throughput for both a single reflection MOA and zone plate

It can be seen that although the total solid angle illuminating the small diameter zone plate is higher than that calculated for the MOA, the poor diffraction efficiency means that more X-rays from both the actuated and unactuated MOAs considered are redirected towards the focus. By matching the numerical aperture of the zone plate to that of the actuated MOA, a larger focused flux of X-rays is obtained. Considering equation (1.18), with a constant focal length and energy, an increase in D leads to a decrease in d_n. For the diameter specified ($D = 2.0\,\text{mm}$), the zone

plate is required to have an outer zone width of $d_n = 10\,\text{nm}$. As described in section 1.4.1.1, this outermost diameter is close to the state of the art dimensions. Table 2.3 shows that for a MOA using a single reflection, the grazing angle at the outer edge (where $h = 1.0\,\text{mm}$) is 1.19°. This is close to the critical angle for grazing incidence reflection for Al K_α, however the reduction of the grazing angle shown by use of a double reflection may increase the reflecting aperture of the MOA further.

2.7 Simulation routines describing a single reflection MOA

The focusing properties of MOAs have been described for a reflecting channel of a very short length. The short reflecting surface limits the range of optical paths that may pass through the channel, and has allowed a complete description to be given for the focusing properties. It is however impossible to produce an infinitely thin channel wall, and it has been shown in section 2.5 that typical channel lengths of $\sim 200\,\mu\text{m}$ may be produced within a silicon substrate. As the finite reflecting surface will produce a broader distribution of X-rays at the focused image, it is therefore useful to simulate the effects of a finite channel wall length on the X-ray distribution. This will allow both the size of the focused spot to be estimated, and also direct comparison between the simulated and experimental distributions to be made.

As previously shown in section 2.2, it is possible for the radiation from a point source to enter the channel, and either be reflected from the outer channel wall, or pass through the channel without reflection. If the channel is moved further from the optical axis, there may be a combination of high grazing angles producing poor reflectivity, as well as shadowing of the X-rays by the inner channel wall that will reduce the total X-ray flux reflected towards the focus spot.

Routines have been written in IDL in order to describe the extent of the intensity distribution from a single channel in the plane of a detector. Previous simulations of the distribution of reflected X-rays within the image plane of the MOA have been achieved using both ZEEMAX [7], and "Q" [23, 24] ray tracing software. These have been used extensively to predict the focusing properties for both single and double reflection focusing MOA systems. A simplified description of the IDL routines now follows. A single reflection from a MOA channel is shown in figure 2.20, occurring at the outer, downstream channel edge. Each of the ray paths describing this reflection may be accurately described by a vector, with the resulting intersection of the ray path with the detector plane shown to occur at the co-ordinates (z, y). Similar vectors may also fully describe intersection of a reflection from the outer, upstream wall, and also the unreflected light intersecting the outer downstream and inner upstream corners of the channel.

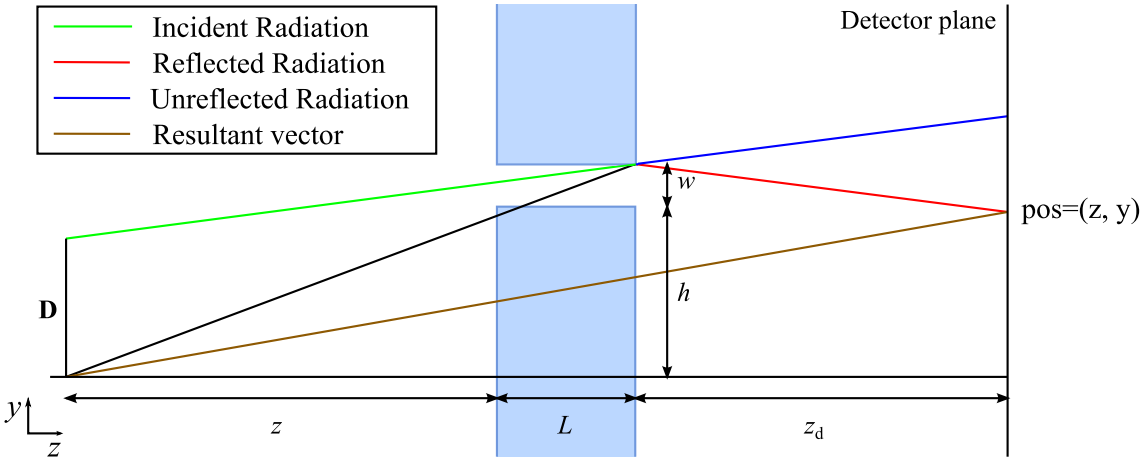

Figure 2.20: The position of a reflection from the Outer Downstream edge of a channel can be described at the detector plane by a single vector

The resulting set of four vectors therefore describe the boundaries of the optical paths, which may be reflected or transmitted through the channel. For an isotropic point source, the intensity between the boundaries where radiation may be detected is assumed to be constant.

An initial approach to calculate the optical path uses a MOA channel parallel to

the optical axis. This results in a simple calculation for the grazing angle, as there is no tilt applied to the channel. To simplify calculations further, as the grazing angle for a MOA is generally small, the reflectivity of the channel wall is assumed to be constant for all grazing angles. The reflectivity may be modified in an extension to the model to depend upon the grazing angle, potentially reducing the intensity detected for higher grazing angles. However, this will require further information about the substrate material, surface roughness and X-ray energy to be included in the calculation.

At higher grazing incidence angles, the shadowing effects described in section 2.2 may be included by calculating the intersection of the ray path for the inner channel edges with the plane of the reflecting surface. If this intersection occurs within the channel wall, the available reflecting surface is shorter than the full length of the wall, and the "shadowed" segment is discounted.

The cumulative intensity distribution from an array of MOA channels may then be modelled by considering the focusing effect from an array of reflecting surfaces. An example of a modelled intensity distribution is shown in figure 2.21, where the radiation emerging from an array of MOA channels has been determined for a single line of CCD detector pixels with a 13.5 μm period. The simulated detector corresponds to the CCD detector described in section 3.3 designed for high efficiency collection of soft X-rays. Simulating the distribution on a detector in this way will allow a direct comparison to be made between the simulated and experimental results obtained in chapter 4. The experimental distributions obtained appear as a constant line of intensity over a 2-D plane due to the extent of the planar channels. The simulated distribution shows that for a point source on the optical axis, the X-ray focus is created due to the combined effect from the array of channels within the shadowed region of the central stop as expected, with a symmetric pattern to either side where radiation passes through the channels without reflection.

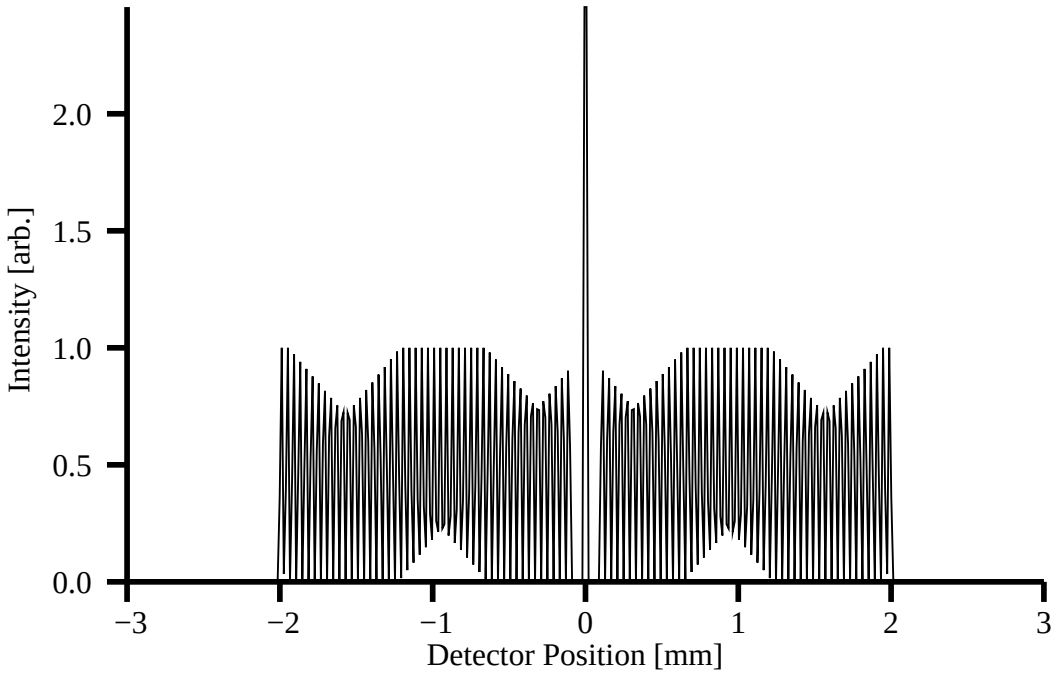

Figure 2.21: Simulated intensity distribution resulting from focusing by a single reflection MOA at $z = z' = 160\,\text{mm}$.

The simulated distribution in figure 2.21 shows the extent of the X-rays at the focused image, when $z = z'$. The routines developed allow the detector to be positioned at any distance downstream of the substrate, allowing the X-ray distribution to be determined at a plane away from the image plane of the MOA. This provides further insight into the focusing properties of MOAs, and allows comparison with experimentally measured distributions, allowing the performance of MOAs to be examined.

The simulated X-ray distribution resulting from a MOA may be presented as an image showing the effect of translating the detector plane away from the downstream channel surface. It is possible to observe the physical size of this distribution through the image plane of the MOA. This is shown in figure 2.22. As previously described, the reflected radiation (red) will converge to a focused spot within the shadow of the central stop. As the width of the beams reflected by each channel is small compared

to the radiation passing through the channel without reflection, the focused X-ray intensity is only bright in the region where the converging X-rays meet within a single CCD pixel.

As the MOA is positioned at a constant distance $z = 160\,\text{mm}$ from the X-ray source in figure 2.22, the total flux of X-rays focused onto the detector should remain constant. It follows from this that as the detector is translated further from the diverging point source, the intensity of the distribution will fall as the extent increases. This effect is not considered within figure 2.22 as the intensity of the distribution measured at each pixel of the detector is always considered to be constant regardless of the distance from the source to the detector. Neglecting the change in intensity allows any changes in the distribution to be more easily determined.

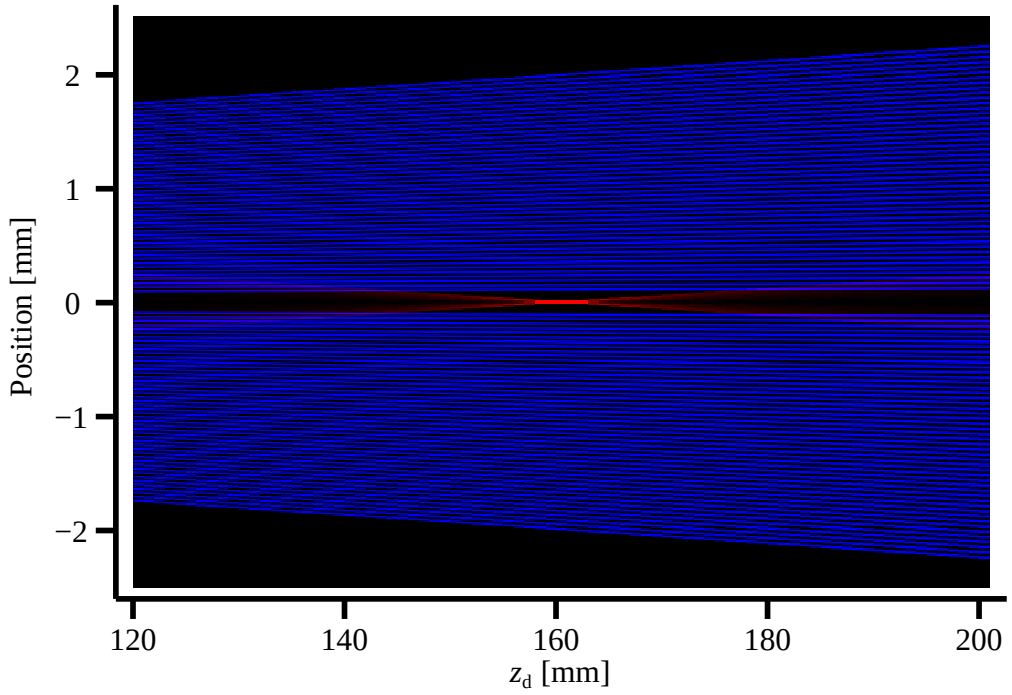

Figure 2.22: Translation of the detector through the plane containing the focused image from a MOA. The reflected radiation (red) converges from each channel to a bright central spot in the shadow of the central stop masking radiation passing through the channels without reflection.

In order to approximate a finite sized X-ray source, the cumulative contribution from several non-axial point sources may be used. The simulation routines developed allow an extended source to approximate either a Gaussian distribution, or alternatively a linear source (of constant intensity). The resulting focused distributions from each source are shown in figure 2.23. Both the Gaussian and linear sources are approximated by 30 individual point sources, with a total width of 80 μm, well below the width of the central stop of the MOA.

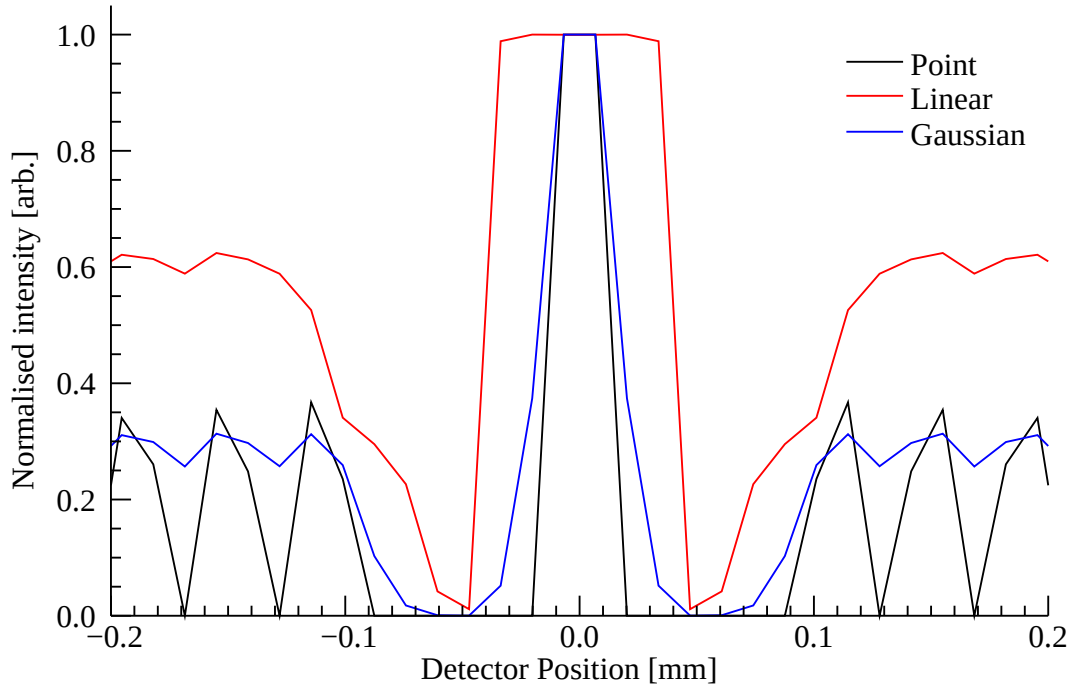

Figure 2.23: Comparison of incident sources with images at the detector plane following reflection

The simulation of a finite source size described above allows a direct comparison to experimental results made for a single reflection MOA. This may be useful when considering the distribution of X-rays further downstream of the focused spot. The changes in the distribution (for example as the detector is translated through the X-ray focus) may also be more easily determined for comparison with experimental results.

While the simulation routines described here are applicable only to single reflection MOAs, where the channel walls are all parallel to the optical axis, it may be possible to extend the model to consider both actuated, and double reflection systems. One possible method of simulating actuated MOAs may be achieved by tilting the channels, or alternatively by rotating the optical axis to consider channels parallel to the optical axis. Double reflection systems will involve more complex shadowing effects from both arrays, so the routines developed to simulate the distribution becomes complicated. In practice, standard ray tracing methods may be more suitable for a MOA focusing optic using a double reflection.

2.8 Summary

Microstructured Optical Arrays have been developed by the SXO consortium as a focusing optic for soft X-rays, using grazing incidence reflections from a fabricated array of small planar channels etched into a silicon substrate. It has been shown that the use of reflections from two arrays of channels enhances the focusing ability by control of aberrations, and also increasing the reflecting aperture. Initial MOA structures have been manufactured, and actuation of the channel structure has been demonstrated using piezoelectric actuators bonded to the substrate. The use of such reflective optics has been discussed with the aim of replacing zone plates in X-ray microprobe experiments, where a high intensity focused spot is required for radiobiological studies.

Simulation routines have been developed, allowing the X-ray distribution to be modelled, at a detector plane downstream of a MOA substrate. Such simulations will be of direct use in chapter 4, where the optical performance of fabricated MOAs is discussed.

References

[1] E. Spiller. *Soft X-ray Optics*. SPIE Press, 1994.

[2] H. N. Chapman, K. A. Nugent, and S. W. Wilkins. "X-Ray Focusing Using Square Channel-Capillary Arrays". In: *Review Of Scientific Instruments* 62.6 (June 1991), pp. 1542–1561.

[3] S. W. Wilkins, A. W. Stevenson, K. A. Nugent, H. Chapman, and S. Steenstrup. "On The Concentration, Focusing, And Collimation Of X-rays And Neutrons Using Microchannel Plates And Configurations Of Holes". In: *Review Of Scientific Instruments* 60.6 (1989), pp. 1026–1036.

[4] L. Pina. *Modern Developments in X-ray and Neutron Optics*. Ed. by A. Erko, M. Idir, T. Krist, and A. G. Michette. Springer, 2008. Chap. 20, pp. 319–329.

[5] M. K. Joy. *Handbook of Optics*. Ed. by M. Bass. Vol. 3. McGraw-Hill, 2001. Chap. 28.

[6] C. A. MacDonald and W. M. Gibson. *Handbook of Optics*. Ed. by M. Bass. Vol. 3. McGraw-Hill, 2001. Chap. 30.

[7] A. Michette, T. Button, C. Dunare, C. Feldman, M. Folkard, D. Hart, C. McFaul, G. R. Morrison, W. Parkes, S. Pfauntsch, A. K. Powell, D. Rodriguez-Sanmartin, S. Sahraei, T. Stevenson, B. Vojnovic, R. Willingale, and D. Zhang. "Active micro-structured arrays for X-ray optics - art. no. 670502". In: *Advances In X-ray EUV Optics and Components II* 6705 (2007), pp. 70502–70502.

[8] R. Willingale, C. Feldman, A. Michette, T. Button, C. Dunare, M. Folkard, D. Hart, C. McFaul, G. R. Morrison, W. Parkes, S. Pfauntsch, A. K. Powell, D. Rodriguez-Sanmartin, S. Sahraei, M. T. Shand, T. Stevenson, B. Vojnovic, and D. Zhang. "Active Microstructured Optical Arrays of Grazing Incidence Reflectors". In: *X-Ray Optics and Instrumentation* 2010, 56836 (2010), p. 856836. DOI: 10.1155/2010/856836.

[9] A. G Michette. *Optical Systems For Soft X-rays*. Plenum, 1986.

[10] D. Rodriguez Sanmartin, D. Zhang, T. Button, C. Meggs, C. Atkins, P. Doel, D. Brooks, C. Feldman, R. Willingale, A. Michette, S. Pfauntsch, S. Sahraei, M. Shand, A. James, G. Willis, C. Dunare, T. Stevenson, W. Parkes, and A. Smith. "Development of spider micro-structured optical arrays for X-ray optics". In: *Proceedings of the SPIE - The International Society for Optical Engineering* (2010), 780306 (11 pp.) DOI: 10.1117/12.860420.

[11] C. Dunare, W. Parkes, T. Stevenson, A. Michette, S. Pfauntsch, M. Shand, T. Button, D. Rodriguez Sanmartin, D. Zhang, C. Feldman, R. Willingale, P. Doel, H. Wang, A. Smith, and A. James. "Micromachining optical arrays". In: *2010 International Semiconductor Conference (CAS 2010)* (2010). DOI: 10.1109/SMICND.2010.5650215.

[12] F Laermer. "Method of anisotropically etching Silicon". Pat. 5501893. 1996.

[13] B. Wu, A. Kumar, and S. Pamarthy. "High aspect ratio silicon etch: a review". In: *J. Appl. Phys.* 108 (2010), p. 051101. DOI: 10.1063/1.3474652.

[14] C. Dunare, W. Parkes, T. Stevenson, A. Michette, S. Pfauntsch, S. Sahraei, M. Shand, D. Zhang, D. R. Sanmartin, T. Button, C. Feldman, R. Willingale, P. Doel, H. Wang, and A. James. "Microstructured optical arrays for smart X-ray optics". In: *Proceedings of the SPIE - The International Society for Optical Engineering* (2009), 736015 (12 pp.) DOI: 10.1117/12.820598.

[15] F. Sami. *Introduction to microfabrication*. 2nd ed. John Wiley & Sons, Ltd., 2010. Chap. 20, pp. 237–254.

[16] D. R. Sanmartin. "Smart Piezoelectric devices for X-ray optics applications". PhD thesis. The School of Metallurgy, Materials, Engineering, and Physical Sciences, The University of Birmingham, 2011.

[17] L. Sveda, L. Pina, A. Inneman, V. Semencova, J. Marsik, R. Hudec, A. Bartnik, H. Fiedorowicz, R. Jarocki, J. Kostecki, R. Rakowski, and M. Szczurek. "Multi-foil optic condenser for a laser plasma EUV source". In: *Physica Scripta* T123 (2006), pp. 131–134. DOI: 10.1088/0031-8949/2006/T123/019.

[18] A. Peele, G. Fraser, A. Brunton, A. Martin, R. Rideout, N. White, R. Petre, and B. Feller. "Recent studies of lobster eye optics." In: *X-Ray Optics, Instruments, and Missions* 3444 (1998), pp. 404–415.

[19] A. G. Peele. "Investigation of etched silicon wafers for lobster-eye optics". In: *Review of Scientific Instruments* 70.2 (1999), pp. 1268–1273.

[20] Y. Ezoe, M. Koshiishi, M. Mita, K. Mitsuda, A. Hoshino, Y. Ishisaki, Z. Yang, T. Takano, and R. Maeda. "Micropore x-ray optics using anisotropic wet etching of (110) silicon wafers". In: *Applied Optics* 45.35 (2006), pp. 8932–8938.

[21] G. Schettino. "Development of a focused X-ray source as a microprobe of cellular radiation response". PhD thesis. University of London, 2000.

[22] K. Atkinson. "An improved soft X-ray microprobe for irradiating subcellular targets". PhD thesis. University of London, 2009.

[23] *Q help index*. http://www.star.le.ac.uk/~rw/q_v6/index.html. Sept. 2011.

[24] C. Feldman. "Smart X-ray optics for large and small scale applications". PhD thesis. University of Leicester, Space Research Centre, Department of Physics and Astronomy, 2009.

Chapter 3

Development of a microfocus X-ray source for optical characterisation

3.1 Overview of X-ray source development

In order to experimentally characterise the optical performance of a MOA for use within a microprobe experiment, a suitable X-ray source must be used. Previous X-ray microprobes have been developed using the small sized source generated by bombarding a solid target with a tightly focused electron beam, and are therefore well suited for use with MOAs. One such microfocus X-ray source producing characteristic C K radiation has previously been described [1], and will be used within this thesis as the basis for the optical characterisation experiments described in chapters 4 and 5. Previous microprobe experiments performed using this source using zone plate optics are also compared to MOAs in section 2.6.1.

This chapter will summarise the main properties of the microfocus X-ray source, as well as highlighting the performance of the source through characterisation measurements. Several recent modifications made to the source are also reported,

allowing it to be used to assess the optical properties of MOAs. The microfocus source assembly will discuss the integration of the source with the CCD detector and rotating shutter, used as an essential mechanism to improve the quality of images obtained. The handling, manipulation and alignment of optical elements such as MOAs within the optical path from microfocus source to the detector will also be described in this chapter.

3.2 The microfocus X-ray source

The X-ray generation processes described in section 1.2.1 where energetic electrons bombard a solid target are frequently used to produce X-rays within small scale laboratories. The emitting size of the X-ray source is defined primarily by the distribution of incident electrons at the surface of the target, with factors such as scattering of electrons within the target material, and the quality of the target surface changing the size and flux of the emitting source. Such factors have previously been discussed [2], during the development of an improved microfocus source intended for use in a microprobe geometry. Within this thesis, the definition of a microfocus X-ray source is one that is capable of producing small ($\sim 20\,\mu\text{m}$) size spots of electrons on the surface of a target. Such sources are commercially available [3, 4], with the parameters of such X-ray tubes within this range, delivering X-rays up to an energy of $E_{\text{max}} \approx 100\,\text{keV}$.

The microfocus X-ray source currently in use at KCL is shown schematically in figure 3.1. This source was installed at KCL during 2008, having previously been developed for use in radiobiological experiments at the Gray Cancer Institute (GCI) using the microprobe geometry. While several modifications have recently been included in order to allow the optical characterisation of MOAs, the path of electrons from the source to the X-ray generating target remains unchanged, and a summary will now follow.

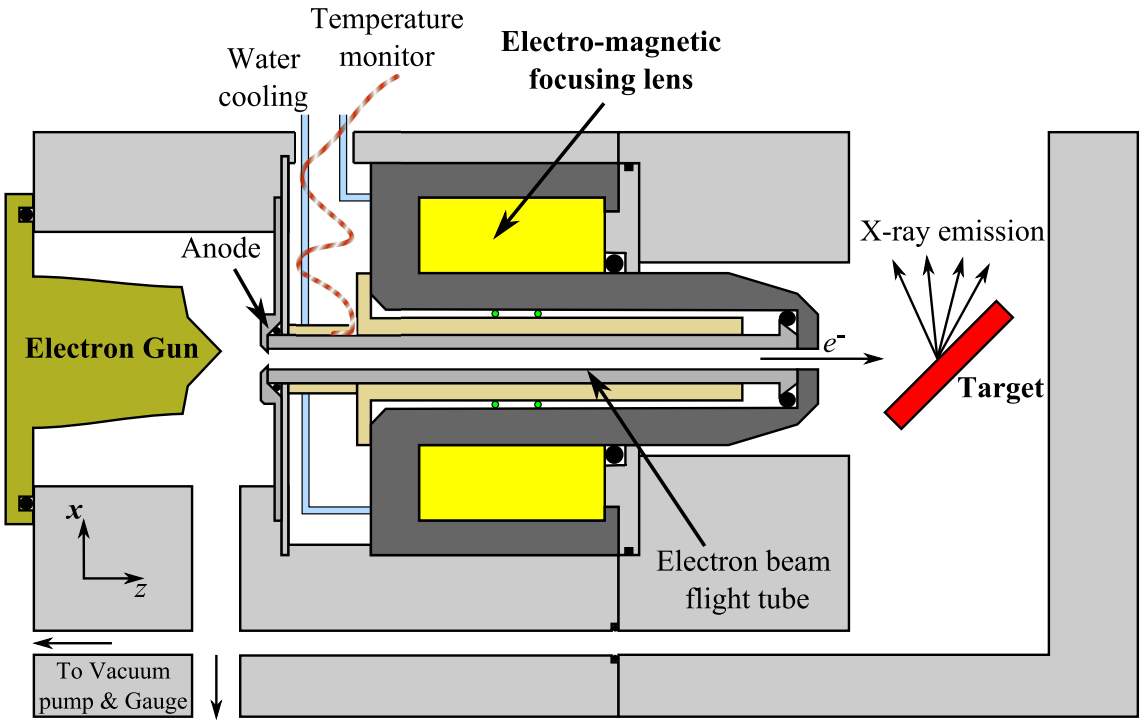

Figure 3.1: Schematic of the microfocus X-ray source at KCL. Accelerated electrons produced by an electron gun travel along the flight tube, and are focused by the electromagnetic focusing lens onto the solid target producing X-rays.

The path of the electron beam used to produce the X-ray source is confined within two separate blocks, joined by an electron flight tube. These blocks support the electron emission gun, magnetic focusing lens and electron target (at the point where X-ray generation occurs), while allowing vacuum to be maintained along the electron flight path, preventing attenuation of both the electron and X-ray beams. The path of electrons through the microfocus source is described by three separate sections, shown in bold in figure 3.1. Firstly, electrons are generated and accelerated using an electron gun assembly and anode. These accelerated electrons are then focused as they travel along the path by an electro-magnetic focusing lens, onto the solid target. Each section along the electron beam path is described in sections 3.2.1 to 3.2.3.

3.2.1 The electron gun assembly

The source of electrons to be accelerated towards the target is an electron gun. This consists of a hairpin tungsten filament wire bent to form a sharp point, surrounded by a Wehnelt cap, as shown in figure 3.2. As current passes through the filament heating the wire, electrons are lost to the surrounding vacuum. These electrons are then accelerated towards the anode plate located along the beam path. In order for the acceleration of electrons to occur, the anode must be at a positive potential with respect to the filament wire. In the implementation of the microfocus source, the anode is held at 0 V along with the main body of the source, with the potential of the filament wire at $-\Phi_{e^-}$. The difference between these two potentials determines the final kinetic energy of the accelerated electrons beyond the anode (E_{e^-}).

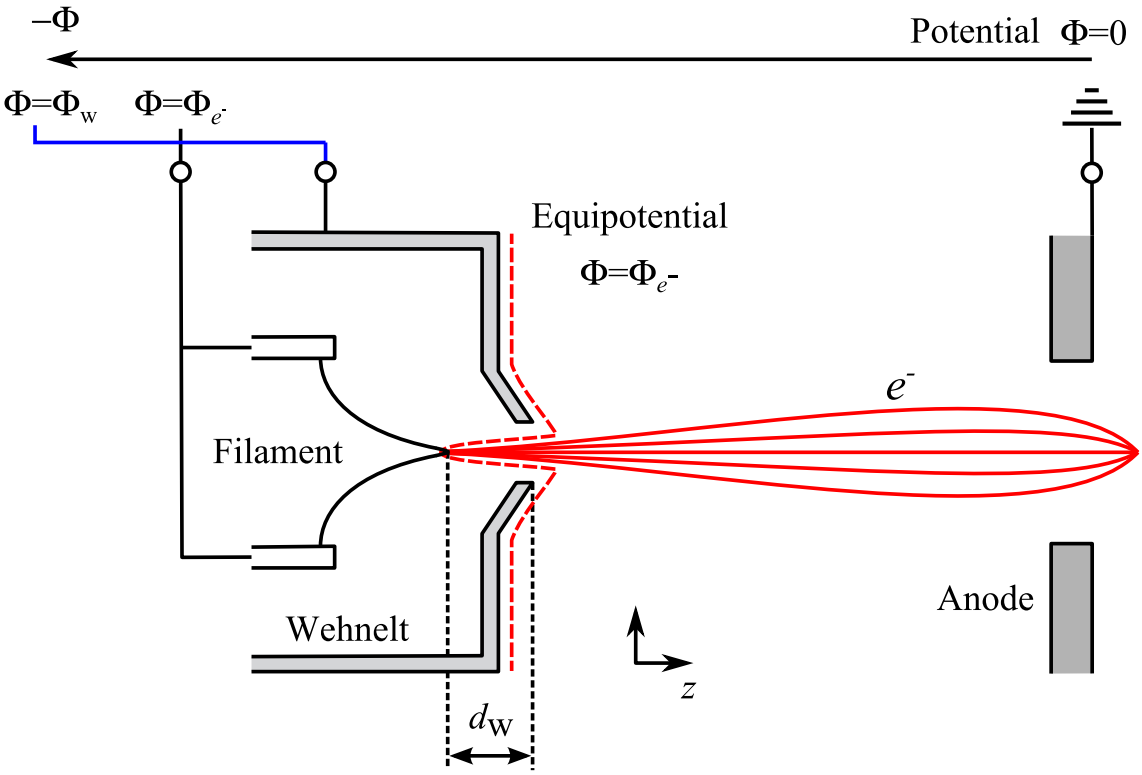

Figure 3.2: The electron gun and anode for the microfocus X-ray source, showing the electron path (red) from the filament to the anode (diagram adapted from [5])

A central hole within the anode plate allows the accelerated electrons to pass

through towards the electromagnetic focusing lens. While the anode plate is fixed to the main body of the X-ray source, the electron gun assembly may be mechanically translated about a plane perpendicular to the electron beam (z) axis, allowing fine-control of the electron beam alignment through the central hole of the anode plate. This alignment mechanism has been replaced as part of the redevelopment of the microfocus source, allowing the electron beam to be positioned and aligned much more repeatably when necessary adjustments are required.

The addition of a "Wehnelt" or "grid" cap surrounding the filament allows fine control over the properties of electrons accelerated towards the anode. The potential of the Wehnelt (Φ_{w}) is typically close to that of the filament, and is at a higher negative potential than the filament in the example shown. The Wehnelt cap distorts the electric field surrounding the filament, confining the region where electrons can be accelerated only to the tip of the hairpin filament. The equipotential surface corresponding to the potential of the filament [5] (shown by the dashed line in figure 3.2) describes the region where acceleration may occur from the filament tip. The resulting electron beam accelerated from this region is shown in figure 3.2. Increasing the bias potential between the Wehnelt and filament reduces the depth that this surface penetrates towards the filament, reducing the area of the filament surface from which electrons may be accelerated. The electron acceleration may be eventually suppressed completely by increasing this bias potential further. The physical separation between the filament tip and end of the Wehnelt cap (d_{w}) will also affect the bias voltage for which the electron beam is suppressed.

3.2.2 The electromagnetic focusing lens

Following the beam path of the accelerated electrons past the anode leads to the electromagnetic focusing lens, the purpose of which is to focus the diverging beam of electrons from the electron gun down to a small spot on the surface of the target.

The lens in the microfocus source is constructed of a single iron pole piece with a conical end protruding into the vacuum chamber containing the solid X-ray target. The flight tube maintains a vacuum through the central bore of the pole piece, allowing electrons to travel through the central axis of the magnet. The solenoid magnet itself is contained within the pole piece, and is surrounded by a cooled water bath to remove excess heat generated as current is passed through the magnetic coil. The magnitude of the magnetic flux density B, close to the electron beam axis (estimated from comparison with similar electron focusing lenses [6]) as current is passed through the solenoid is shown in figure 3.3 a). The flux density is shown to reach a peak value slightly beyond the end of the magnetic pole piece. Figure 3.3 b) highlights the corresponding radial distance of the electron path from the electron beam axis, and shows that the electron intersect the axis close to the position of the peak magnetic flux density.

As the electrons travel along the flight tube, they experience a force perpendicular to both the direction of motion and the magnetic field lines of the electromagnet. The electrons in the flight tube always travel approximately parallel to the magnetic field lines, and so are influenced by a force in a plane perpendicular to the direction of motion. This force is directed towards the axis of rotational symmetry of the magnet. The electrons therefore spiral around this axis, and are re-directed towards it as they travel beyond the conical pole piece. The force on each electron also increases as B gets larger, further increasing the focusing effect. The axial distance beyond the pole piece for which the electrons meet at a common point on the optical axis therefore depends on the force on each electron, determined by the field density B, and the kinetic energy of the accelerated electrons E_{e^-}. While the description of the electromagnetic focusing lens included within this section describes the focusing of electrons to a small point, symmetrically centred on the axis of the electromagnetic lens, an exact estimate of the distribution of the electron beam at the focus will not

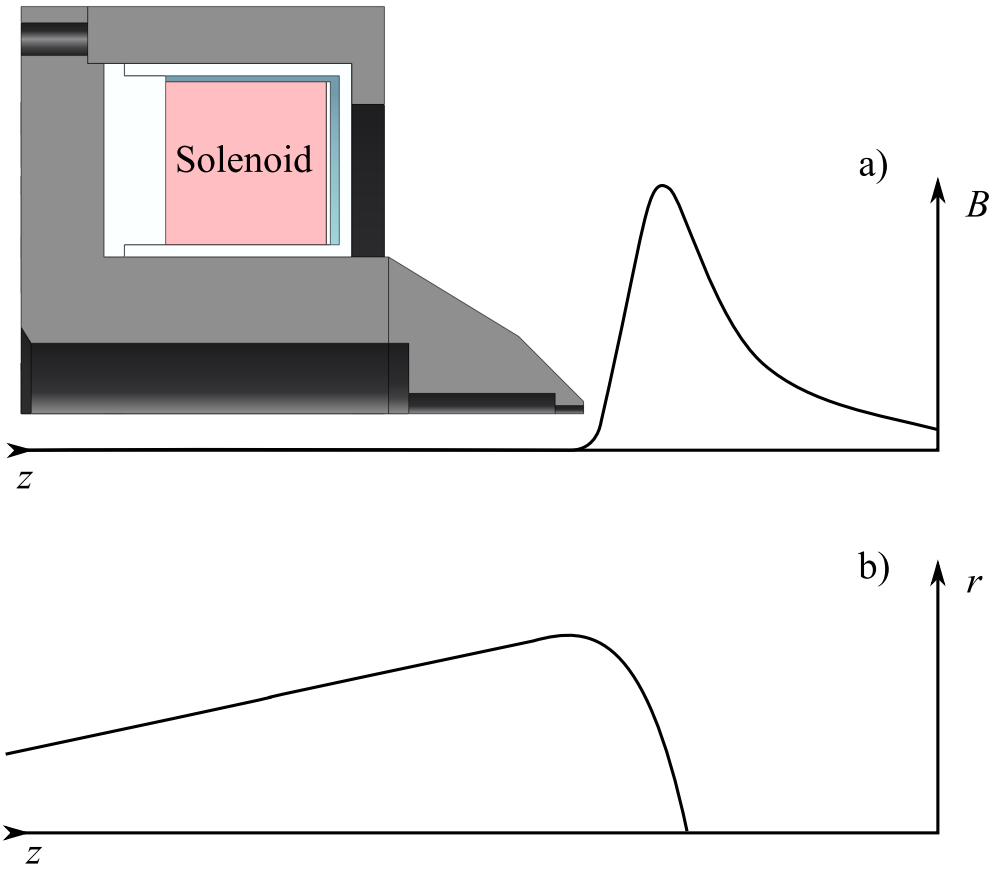

Figure 3.3: Focusing of electrons by the electromagnetic lens. a) Estimated magnetic flux density B along the axis of the focusing lens. b) Corresponding radial position of electrons accelerated by the electron gun.

be given, as the exact structure of the pole piece is undocumented. An experimental estimate of the electron spot size focused by the electromagnetic lens is however included in section 3.5.

Electromagnetic deflection coils also surround the flight tube, allowing the electron beam to be translated perpendicular to the electron optical axis. This provides additional alignment of the electron beam as it passes along the flight tube, increasing the flux of electrons that pass through the narrow exit aperture of the magnetic pole, thereby producing the highest X-ray flux. A thermocouple also rests against the outer wall of the flight tube, providing a useful indicator of electron beam misalignment along the flight tube, as the electrons impacting the thin sides

of the tube quickly causes heating of the walls.

3.2.3 The target geometry

The target for the microfocus source is rigidly mounted with the front surface presented towards the electron beam at an angle of 45°, slightly beyond the end of the magnetic focusing lens. Ideally, the surface of the target should coincide with the smallest diameter of the electron beam as it is focused by the electromagnetic lens, thereby generating the smallest possible spot emitting X-rays. The exit port for the microfocus source where X-rays may travel towards the detector is also at an angle of 45° to the target, and is therefore perpendicular to the electron beam. The target materials currently available for use within the microfocus source are carbon and aluminium, resulting in characteristic X-rays of 0.277 and 1.477 keV emitted through the exit port. As the microfocus X-ray source was originally used for studies using soft X-rays, the target was initially a solid disc of carbon. This has later been exchanged for an aluminium target, generating higher energy X-rays. Other target materials may easily be substituted in the future, allowing higher energy X-rays to be produced when required.

The target of the microfocus source was initially mounted with the X-ray path along a vertical axis relative to the target block. This configuration was used in order to allow the exposure of cells to X-rays from underneath, using a small ($< 1\,\mu$m diameter) focused spot of a microprobe formed using zone plate optics, while allowing imaging to be performed using UV microscopy from above [7]. A vertical X-ray beam is not suitable for the characterisation of MOAs as manipulation of both the optical element and detector is required. While this is possible in a vertical mode, a large support structure would be required in order to support the detector above the X-ray source.

In order to integrate an optical manipulator and detector with the microfocus

source while maintaining vacuum along the X-ray path, the target chamber has been redesigned at KCL, introducing flexibility in the target mounting position. The target may now be mounted using either a horizontal or vertical port, allowing the X-rays to exit the source chamber through the opposite port. A set of interchangeable adapter plates allows this to occur. The exit port of the chamber has also been redesigned to allow a standard vacuum fitting to be used as the output, resulting in an adaptable X-ray source for which the X-ray path may be defined about the horizontal or vertical axis. The X-ray source is now shown in cross section in figure 3.4, showing the path of the electron beam.

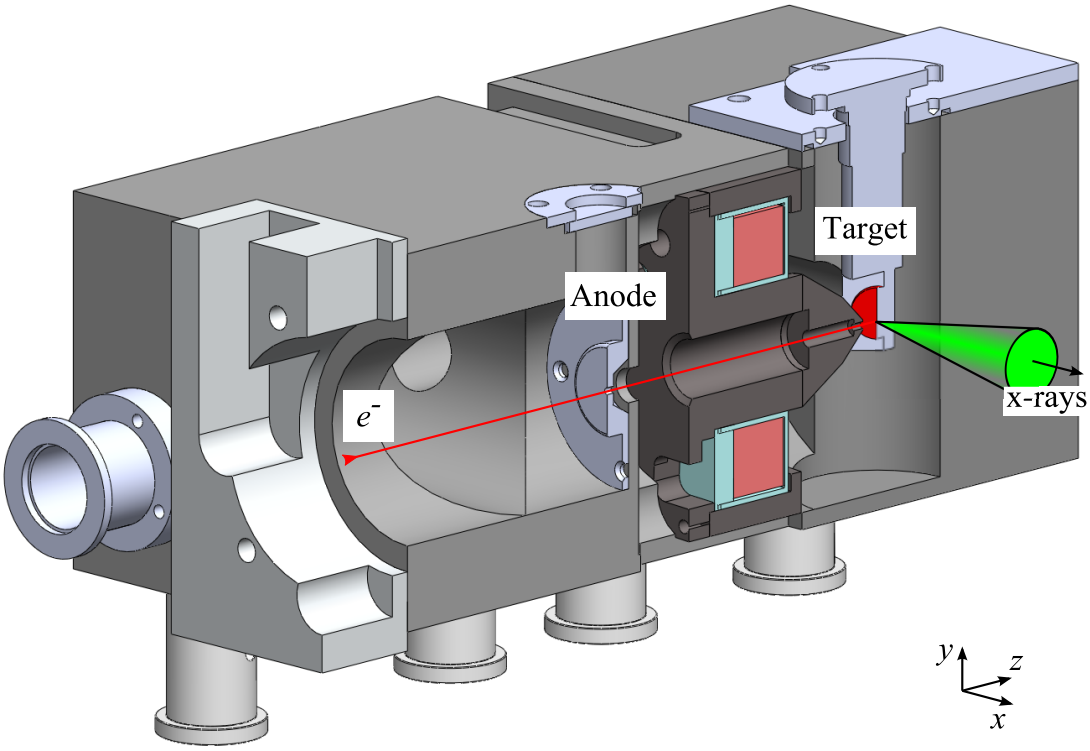

Figure 3.4: Cross section of the microfocus X-ray source along the electron beam path. The electron gun and flight tube are not shown for clarity.

One of the advantages of using a standard exit port in this way is that any length of X-ray path can be coupled to the system, with potentially any combination of optical elements, samples of interest or filters that may inserted at any point along

the path. The extra volume created due to the extension of the path length has required an upgrade of the turbomolecular vacuum pump, to preserve the total vacuum achieved. The pressure of the system is required to be below the interlock pressure of 5×10^{-5} torr, set to prevent damage to the filament and detector. Several replacements to the vacuum O-ring seals have also been made, and a vacuum lower than 5×10^{-6} torr is routinely achieved in operation using the larger volume, an order of magnitude lower than the lowest pressure seen when the source was installed at KCL (2×10^{-5} torr). In addition, the entire microfocus source system can now be raised above the optical table. This allows the X-ray path to be raised when the use of larger manipulators is required.

3.3 The CCD detector for use with the microfocus source

A vacuum compatible X-ray Charged Coupled Device (CCD) detector has been successfully coupled to the microfocus source, at the end of the X-ray path. This direct detection, back-illuminated (Princeton Instruments PI-MTE in vacuum [8]) detector used is specifically designed for in vacuum use, and is optimised for applications requiring detection of soft X-rays. The performance of the CCD chip has been described [9], with the overall performance of the detector summarised in table 3.1. It should be noted that the high energy X-rays (Ti K_α) have been included within this table, for consideration with the argument presented in section 2.6.1.

The entire body of the detector (including the CCD chip, electrical and water coolant connectors) may be placed within a vacuum system. While this may be ideal for certain applications, it requires a large vacuum chamber with additional internal manipulators, allowing positioning of the detector relative to the X-ray beam. As only the CCD chip is required to be contained within the vacuum chamber, a custom

Table 3.1: Summary of the X-ray CCD properties when coupled to the microfocus X-ray source

Pixel array size	2048 × 2048
Pixel size	13.5 µm
Detection efficiency at C K (0.277 keV)	50%
Detection efficiency at Al K_α (1.477 keV)	70%
Detection efficiency at Ti K_α (4.511 keV)	55%
Maximum operating energy	10 keV
Detector chip temperature (typical)	−40°C

interface was designed in order to couple the detector to the microfocus X-ray source. This ensures the CCD chip is under vacuum conditions while the main body of the detector remains at atmospheric pressure.

The CCD chip is then cooled via a Peltier cooler, ensuring a low dark current in the detected image. The vacuum system ensures that condensation does not form on the CCD chip at cold temperatures. Operation of the detector at atmospheric conditions is also undesirable, due to the high attenuation of the incident soft X-rays. It is also essential that contaminants are kept away from the active area of the CCD chip. A hand operated gate valve is therefore located immediately before the CCD chip along the X-ray path isolating the chip from the remaining vacuum system, and maintains a clean, debris free environment between experiments. The gate valve also provides protection for the CCD chip during transportation and installation on the microfocus source. The assembly of the detector system is shown in figure 3.5, including the custom interface and protective gate valve.

3.3.1 Development of the X-ray shutter

Initial experiments using the microfocus source and detector showed a distinct band of constant intensity visible in the detected images. This was caused by the continuous exposure of the CCD chip to radiation as the collected data is read out

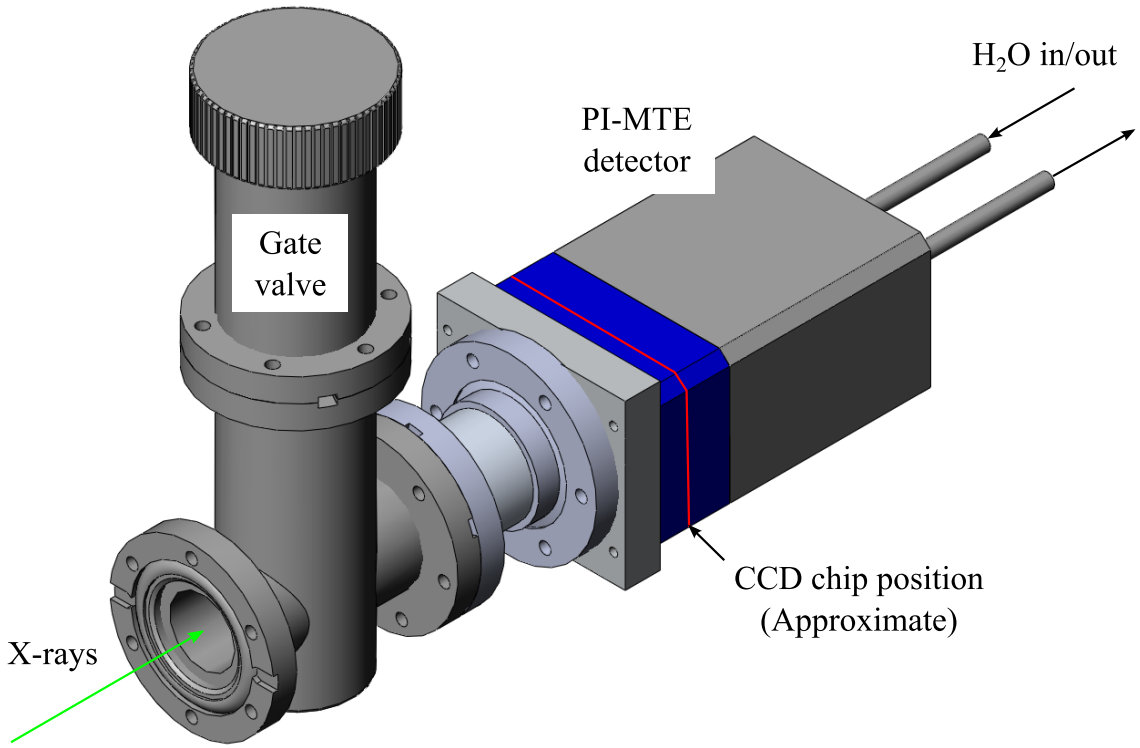

Figure 3.5: Schematic of the soft X-ray CCD detector system, showing the gate valve used to protect the CCD chip.

to the computer – X-rays are detected during the readout time, where the rows of pixels are sequentially digitized using the shift register [10]. This effect became more pronounced at shorter image exposure times, or where a selected region of interest on the CCD chip is large, as the length of time taken to read out the image becomes comparable to the exposure time of the image. A residual image has also been observed in the dark background signal recorded by the detector after prolonged exposure to the X-rays. This increase may be due to the trapping of electrons within the surface of the CCD [11]. This background does decay over time (over a period of around 30 minutes) to the original flat background, however it became clear that the exposure of the CCD to X-rays must be limited to the exposure of the image only.

In order to reduce the exposure of the CCD chip to X-rays as images are collected, a rotating shutter was designed and installed into the X-ray path. The ideal place for

the shutter was within the target block of the X-ray source, immediately downstream from the target. The shutter rotates within the vacuum by 90°, allowing X-rays to either pass through or be completely blocked from exiting the microfocus source via the exit port. This motion is controlled externally using a solenoid coupled to a rotary vacuum feedthrough. This transfers the rotary motion to the shutter, allowing external control. The shutter design implemented (shown in cross section in figure 3.6) also blocks stray light from the source at the detector.

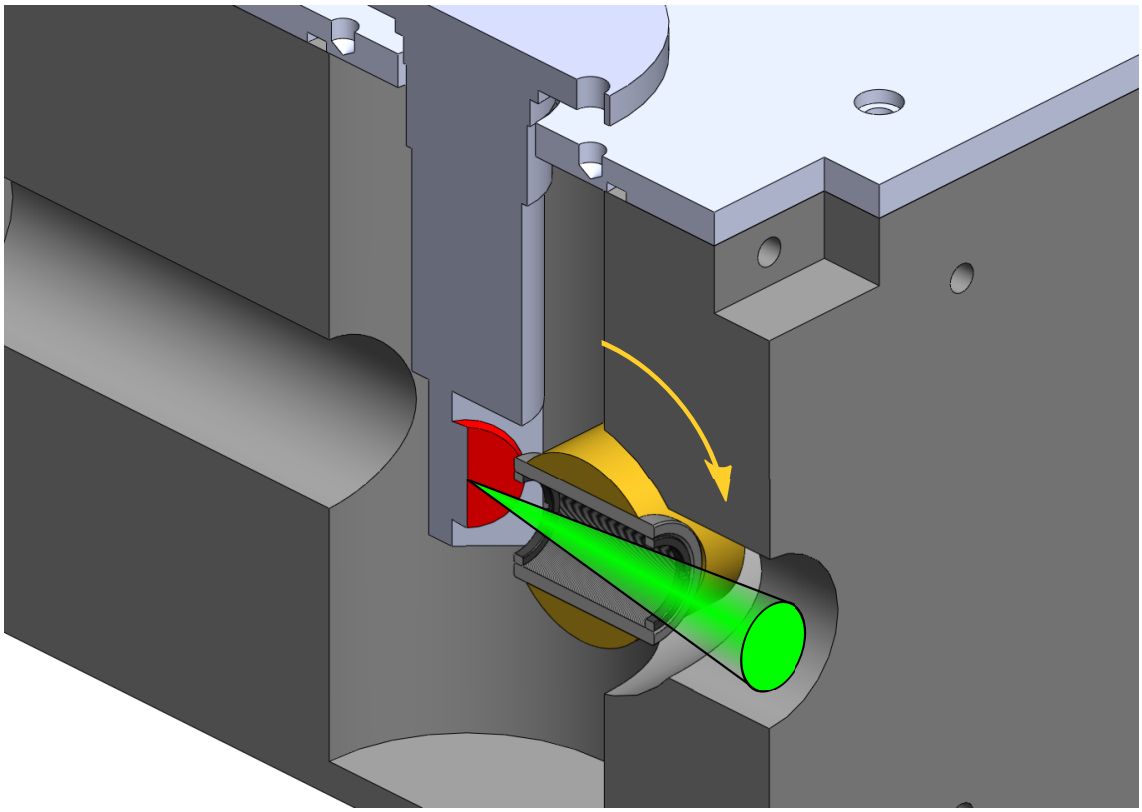

Figure 3.6: The shutter mechanism for the microfocus source. Rotation of the shutter (yellow) obstructs X-rays (green) from leaving the source through the exit port.

The rotating shutter contains a threaded tube, which is aligned parallel to the X-ray optical axis when the CCD is exposed. Along this tube, a range of interchangable apertures, pinholes, filters or additional optical elements may be inserted into the beam path, mounted on a circular disc of diameter 0.25 inch. Any combination of these may be inserted and held within the shutter by retaining rings.

All experiments described within this thesis (unless stated) will use an aperture of diameter 1 mm, retaining a square (1 mm×1 mm) titanium filter (40 nm thick) to absorb the visible light generated by both the filament and X-ray spot. This filter is supported on a 50 nm thick silicon nitride membrane.

Operation of the shutter is controlled by a TTL signal to switch between the open and closed states. The default operation is driven by the output of the control unit of the CCD detector, opening the shutter only during the defined exposure time of the image. This external control prevents exposure of the CCD to the continuous X-ray beam produced by the microfocus source. It is also possible to lock the shutter into either the open or closed state. This is especially useful in the closed state, as it permits a background image to be recorded without changing the emission of the source. Holding the shutter in the open state allows the effect of continuous exposure to be measured. The performance of the shutter is shown in figure 3.7, where a 2 μm thick circular titanium filter is inserted into the X-ray path. It should be noted that this filter was not placed on the shutter assembly, and was located further downstream on a manipulator arm (section 3.4).

The horizontal band caused by continuous exposure during the readout time is clearly visible in figure 3.7 a), with the boundary corresponding to the top and bottom edges of the aperture. The small insets shown in figure 3.7 show the full range of the CCD, and only the bright aperture can be seen. The horizontal band may therefore only be considered to be an issue at low intensities.

3.4 Development of a sample manipulator

Optical elements may be inserted into the X-ray path using a manipulator arm, providing external control over the position. The manipulator itself is a vacuum feedthrough allowing linear translation, coupled to a rigid rod with the sample holder mounted at the end. Different samples may be examined using this system,

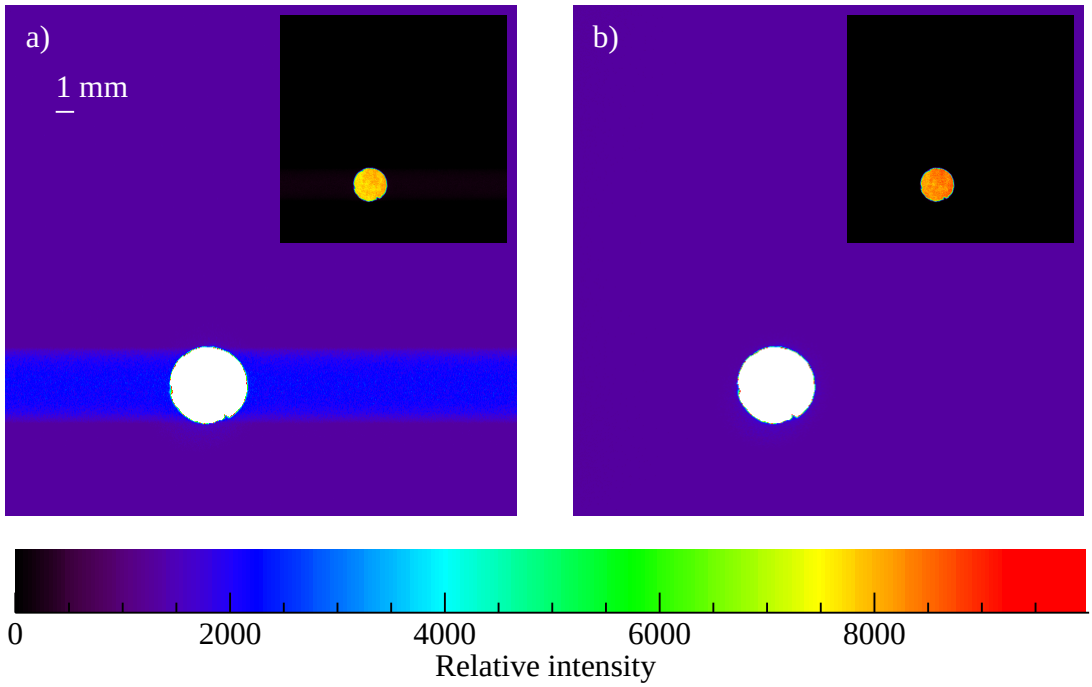

Figure 3.7: Comparison of X-ray image of a Ti filter produced by the microfocus X-ray source. a) Full detector chip image with the shutter continuously open. b) An identical image with shutter closed during the data readout. Insets in each case show the same image with a larger intensity scale (55000 counts)

supported within a 1 inch threaded holder, and are held with a retaining ring. The rod is also designed to allow testing of actuated MOAs [12]. Translation of the manipulator is possible in a plane perpendicular to the axis of the X-ray beam, with sufficient travel to allow the sample to be completely removed from the path.

The total optical path from X-ray source to detector can be changed by introducing combinations of linear translators, and rigid vacuum pipe along the optical path. The distances between the source, manipulator and detector is therefore potentially very versatile, with a few limitations due to the physical path lengths (for example from the X-ray source to the exit port of the microfocus source). Due to the physical size of the source, manipulator and detector, the minimum possible path length is 160 mm between the source and sample manipulator, and a corresponding minimum distance of 165 mm separates the sample and detector. The

full optical path is shown in figure 3.8, where the microfocus source is configured for optical testing.

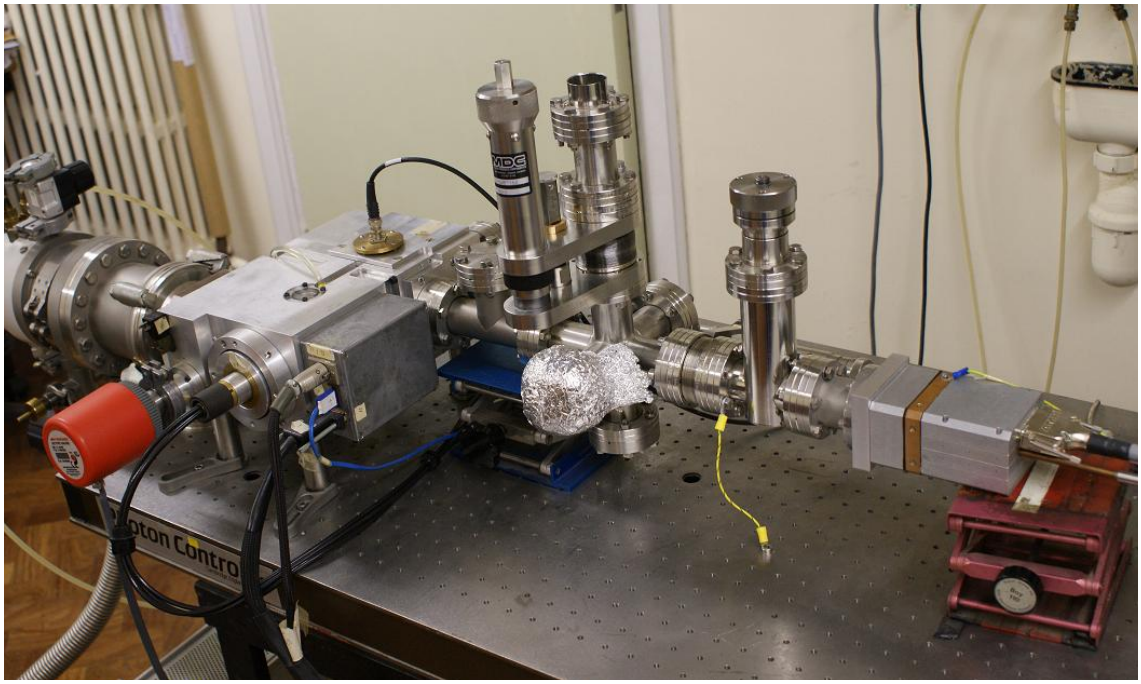

Figure 3.8: The microfocus soft X-ray source configured for optical testing. X-rays emitted by the source pass the shutter and manipulator on towards the detector.

3.5 Performance and characterisation of the microfocus X-ray source.

As discussed in section 3.1, the performance of the microfocus source has been previously described, using a carbon electron beam target for soft X-ray production. This characterisation provided valuable information regarding the source size and spectral range, along with the overall X-ray flux recorded in the focused spot of the microprobe. Previous calibration also described typical parameters used to control the source, specifically the accelerating potential and current of the electron gun, as well as the Wehnelt potential Φ_w, and distance d_w. Optimisation of these control parameters allows the current measured at the target to be maximised, therefore

giving the highest possible X-ray flux emitted from the source. There are, however significant discrepancies between the optimal parameters previously described [1] with those currently in use, and it is currently unclear why these differences arise. The settings have therefore been re-optimised for the redeveloped microfocus source and a summary will now follow.

The current detected at the target due to the focused electron beam changes with the properties of the Wehnelt and the electron gun. This is shown in figure 3.9, where the electrons focused through the small aperture of the electromagnetic lens onto the target are recorded for an increasing Wehnelt potential. The effect of altering the separation d_{w} is also shown in figure 3.9. A constant filament potential of 10 keV is used throughout, with a filament current of 2.95 A. For each result taken, the electron beam was focused using a lens current of 10.7 A, and the electron gun was mechanically aligned each time to maximise the target current. It is shown that the peak value of the focused target current remains constant as d_{w} is changed, for different Wehnelt potentials. This is expected from section 3.2.1, as the equipotential of the filament penetrates a larger distance into the Wehnelt at a higher potential.

The trend of figure 3.9 indicates that the electron beam current (+) from the filament decreases consistently as the Wehnelt potential is increased. This current indicates the electron flux accelerated by the electron gun, and is different to the filament current described in section 3.2.1. Clearly this is much larger than the focused target current ($\diamond$), indicating a loss of electrons along the beam path. In general however, the electron beam current must be kept low to avoid excessive heating of the anode plate. A high beam current has previously led to a failure of the vacuum seal located behind the anode plate in the past, and must be avoided. The Wehnelt potential that gives the highest target current is therefore used for the remainder of the thesis.

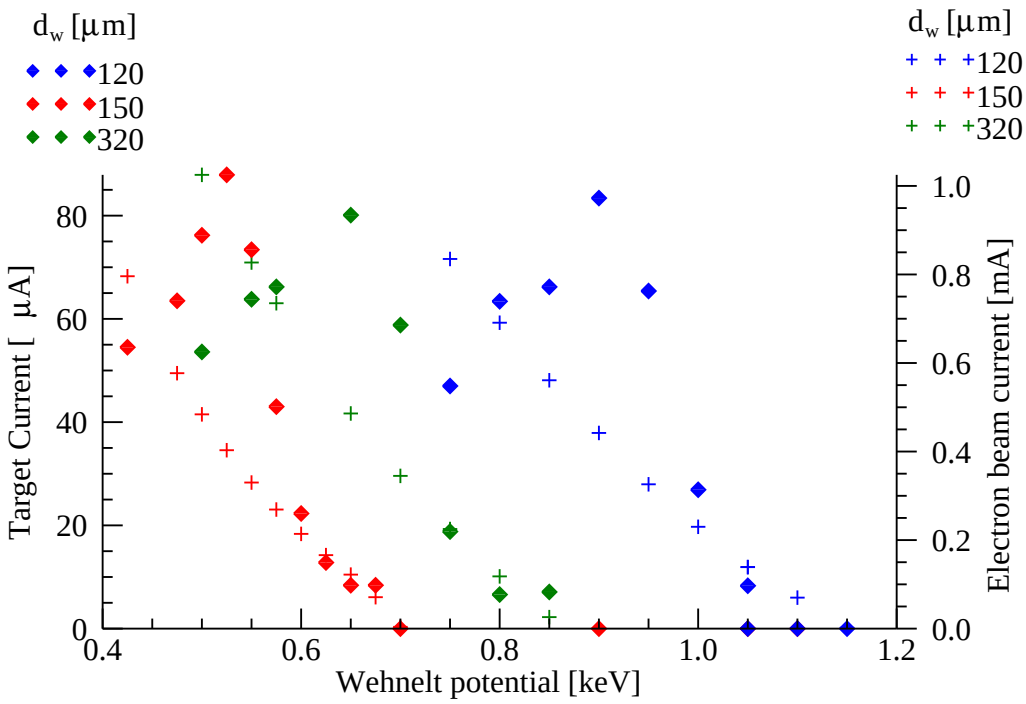

Figure 3.9: Emission characteristics for the focused electron gun. Electron beam currents emitted by the electron gun (RHS) are compared with the maximum current focused onto the target (LHS).

3.5.1 Source size measurements

Estimates of the micro-focus X-ray source size have been made using two separate methods, evaluating both the electron and X-ray distributions. Measurement of the electron distribution has been achieved using a phosphor scintillator screen, converting the energy of incident electrons falling on the target to visible light. The visible light produced may then be imaged using visible light CCD, with a zoom lens focused onto the target. Installation of a clear glass window directly on the exit port of the microfocus source allows the CCD to be positioned close to the source. By changing the current passing through the solenoid of the magnetic focusing lens, the smallest distribution of electrons incident on the target may be determined, allowing the properties of the electromagnetic focusing lens to be evaluated. This is shown in figure 3.10, where the visible image produced by the phosphor screen is

recorded in both the horizontal and vertical direction. In order to avoid damage to the phosphor screen, the filament current of the electron gun was limited to 1.6 A, reducing the current contained within the electron beam.

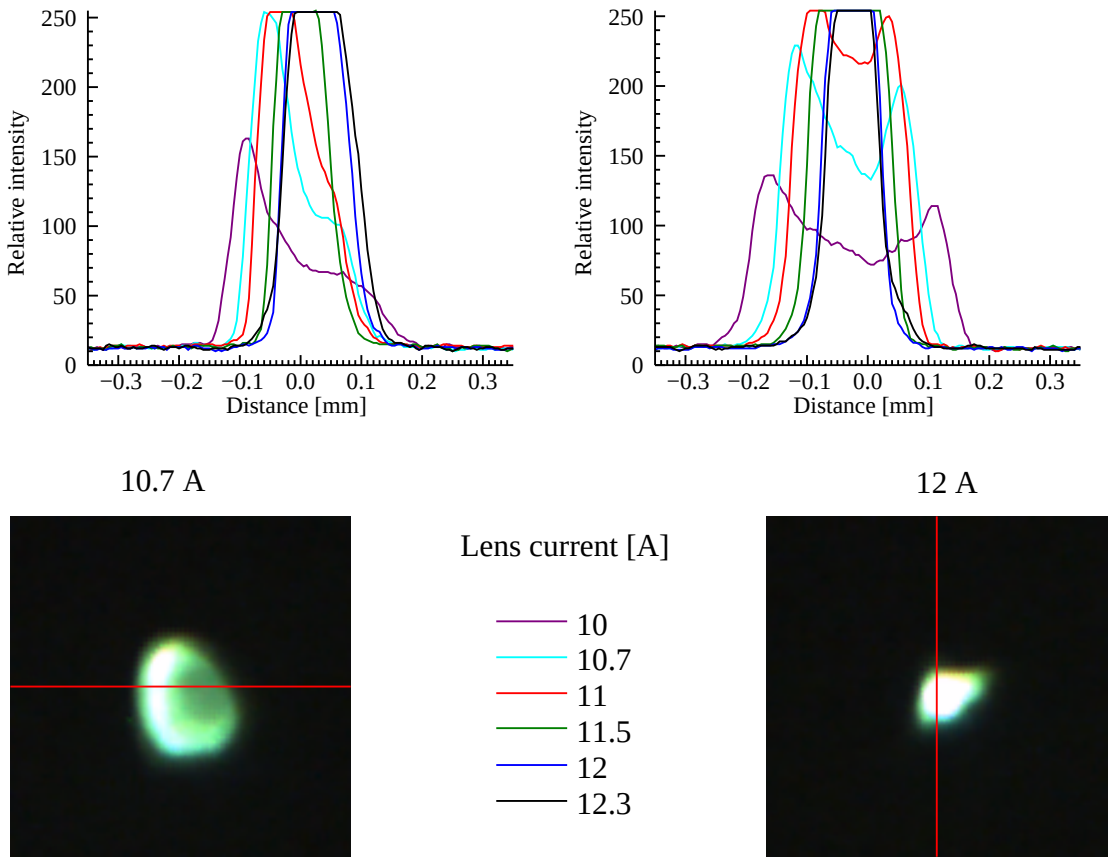

Figure 3.10: Electron distribution at the X-ray target, estimated by conversion to visible light using a scintillator screen in both the horizontal (LHS) and vertical (RHS) directions. The diameter of the focused electron spot decreases as the focusing lens current is increased.

Figure 3.10 shows that the smallest diameter of the electron beam has a width of $\approx$ 200 µm obtained at a focusing lens current of 12 A and an electron beam energy of 10 keV. This is the distribution produced as the electrons interact with the scintillator screen, and so multiple interactions and scattering, as well as broadening may increase the diameter. The distribution shown at 12 A does however show a slight distortion from the circular distribution obtained at 10.7 A. The more circular

distribution produced at 10.7 A may be more suitable for use with the X-ray source, although may produce a slightly larger diameter in the focused electron spot. The image shown for 10.7 A does however show some variation in intensity, resulting in a slightly asymmetric distribution. The optimum lens current is lower at a reduced filament potential, however this will not be discussed as an energy of 10 keV has been used consistently throughout this thesis.

The physical size of the X-ray source has also been estimated using a pinhole inserted in the manipulator arm to remove most of the X-ray signal. This acts as a pinhole camera when used with the CCD detector. The resulting X-ray distribution produced by the pinhole camera is shown in figure 3.11, as X-rays emitted by the aluminium target pass through a pinhole of diameter 50 μm. The visible light filter used in this example is a 2 μm thick titanium film mounted directly before the pinhole. Only the focusing lens current of 10.5 A is presented here, however a similar effect to that observed in figure 3.10 is observed, where X-rays are emitted over a wider area of the target due to the defocused electron beam.

The total width of the X-ray distribution shown in figure 3.11 is approximately 300 μm. Considering the distance from the source to pinhole is 160 mm, and the corresponding distance from pinhole to detector is 250 mm, the size of the X-ray emitting spot is ≈ 200 μm in diameter.

Previous measurements of the electron distribution [1] have been made by measurement of the target current. Scanning the focused electron spot across the surface of the target using the deflection coils contained within the magnetic lens results in rapid changes in the target current when a grid is placed directly in front of the target. Such a grid, containing struts of a comparable width to the electron beam (5 μm) placed before the target resulted in regions where the electron beam is completely blocked by the grid as it is scanned across the surface, leading to a large variation in the target current. This has led to an approximate electron beam size

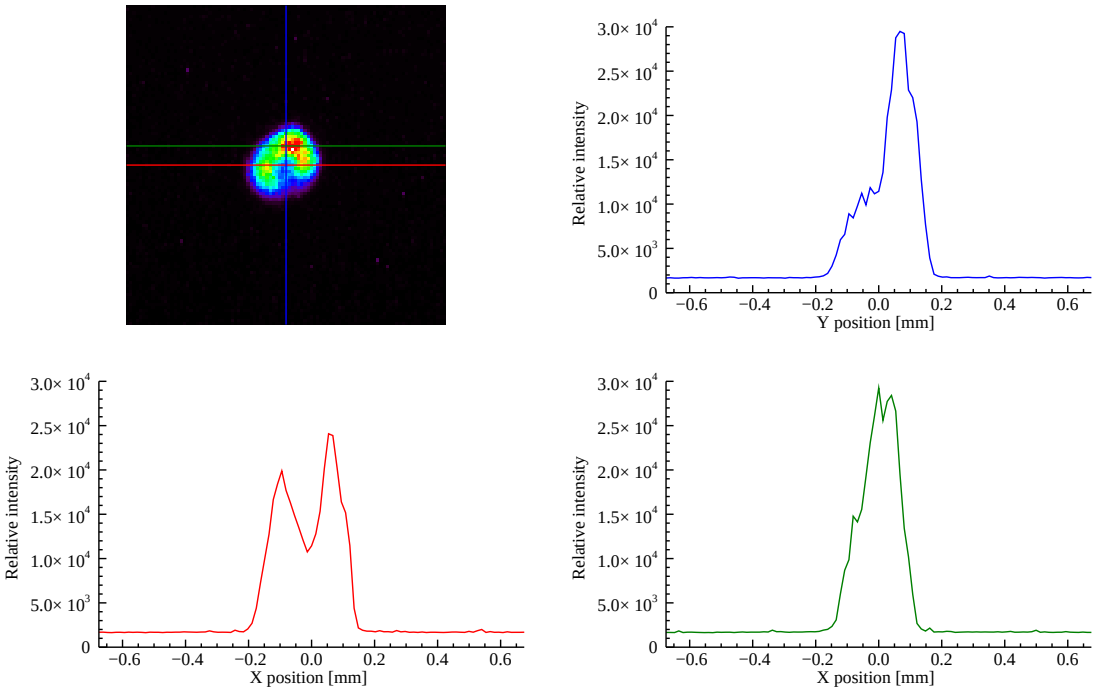

Figure 3.11: The typical X-ray distribution measured using the X-ray pinhole camera. The distribution was produced using a focusing lens current of 10.5A and the aluminium target.

of 4 µm being determined. The source sizes measured here however are significantly larger, by over an order of magnitude. While this may be due to an undocumented modification to the source, it may also be due to poor sensitivity to the target current at low values, resulting in the measurement of the very small central distribution, and not the full width. The X-ray pinhole camera measurements taken here however should provide a good estimate of the working size of the X-ray source, as they are taken within normal operating parameters.

3.5.2 Future developments

The spectral emission of the microfocus X-ray source has not been considered within the characteristic measurements described. In order to measure the spectrum produced, a transmission diffraction grating (produced by Silson Ltd.) has been manufactured, and is currently awaiting testing. The tungsten transmission grating

has a 500 nm period. The grating has been designed to fit within the sample manipulator described in section 3.4, and so installation and alignment is simple.

In conjunction with the development of the diffraction grating, a grazing incidence mirror assembly is also in development, designed to remove the high energy bremsstrahlung produced by the microfocus source. Such evidence for hard X-rays is shown in chapters 4 and 5. This mirror was an original feature of the microprobe [1] to reduce chromatic aberration caused by the zone plate, and is now being redeveloped in order to integrate with the microfocus source as an in-line module, located directly following the exit port of the target chamber. The operation of the grazing incidence reflection mirror is shown in figure 3.12.

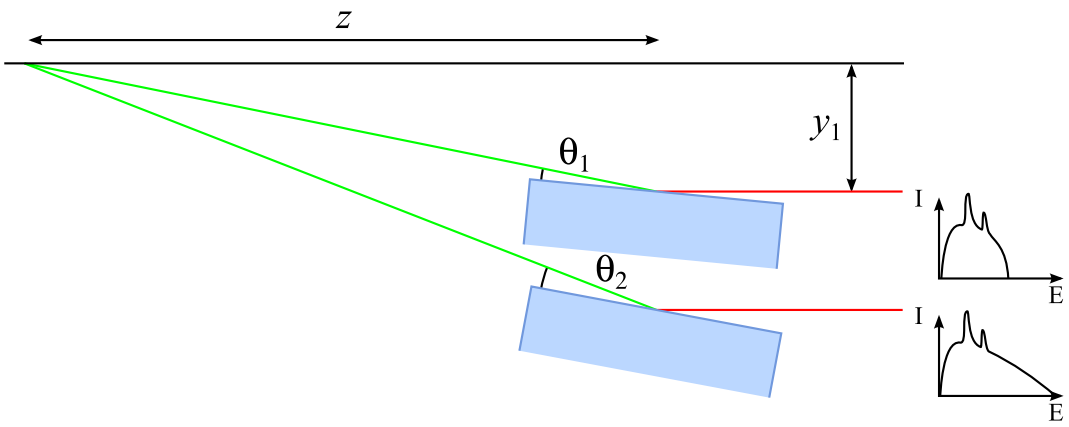

Figure 3.12: A single grazing incidence reflection removes the high energy bremsstrahlung from the X-ray spectrum. Manipulating the grazing reflection angle allows the maximum energy reflected to be altered. The X-ray reflectivity from the mirror may be found for each target energy through figure A.2, in appendix A.

The mirror used at grazing incidence is highly polished silica, providing high reflectivity at soft X-ray energies. Additional development is being incorporated to potentially allow multilayer reflecting mirrors to be included in the future, further increasing the ability to monochromate and define the X-ray beam.

3.6 Summary

The microfocus X-ray source has been developed in order to allow the integration of a CCD detector and optical manipulator in order to allow optical characterisation experiments to be performed. The complete optical system has been described, including the structure of the source, shutter, sample manipulator and CCD detector. Characterisation measurements have shown the performance of the source by maximising the target current. Optimisation experiments evaluate the performance of the electromagnetic focusing lens, and have shown that the size of the X-ray source is typically $\approx 200\,\mu\text{m}$ in diameter. The microfocus X-ray source will now be used within chapters 4 and 5 to demonstrate optical characterisation experiments.

References

[1] G. Schettino. "Development of a focused X-ray source as a microprobe of cellular radiation response". PhD thesis. University of London, 2000.

[2] K. Atkinson. "An improved soft X-ray microprobe for irradiating subcellular targets". PhD thesis. University of London, 2009.

[3] *Hamamatsu Microfocus X-ray Source (MFX) Product information page.* http://sales.hamamatsu.com/en/products/electron-tube-division/x-ray-products/microfocus-x-ray-source-mfx.php. Sept. 2011.

[4] *Rigaku Micromax 007 HF Product information page.* http://www.rigaku.com/generators/micromax007.html. Sept. 2011.

[5] P. W. Hawkes and E. Kasper. *Principles of Electron Optics: Applied geometrical optics.* Vol. 2. Academic Press, 1989, pp. 907–912.

[6] T. Mulvey. *Magnetic electron lenses.* Ed. by H. P. W. Springer-verlag, 1982, p. 394.

[7] M. Folkard, G. Schettino, B. Vojnovic, S. Gilchrist, A. G. Michette, S. J. Pfauntsch, K. M. Prise, and B. D. Michael. "A focused ultrasoft X-ray microbeam for targeting cells individually with submicrometer accuracy". In: *Radiation Research* 156.6 (2001), pp. 796–804.

[8] *PI-MTE in-vacuum CCD detector*. http://www.princetoninstruments.com/Uploads /Princeton /Documents /Datasheets /Princeton_Instruments_ PI-MTE 2048B _Rev_N1_2.22.2011.pdf. Sept. 2011.

[9] *Datasheet for CCD chip*. http://www.e2v.com/assets/media/files/documents/imaging-space-and-scientific-sensors/08-42-40-FI-AIMO-Cpak.pdf. Sept. 2011.

[10] *PI-MTE System manual*. 3.D. Princeton Instruments. Mar. 2006.

[11] B. G. Magorrian and N. M. Allinson. "Soft X-ray Damage In CCD Detectors". In: *Nuclear Instruments & Methods In Physics Research Section A-accelerators Spectrometers Detectors and Associated Equipment* 273.2-3 (Dec. 1988), pp. 599–604. DOI: 10.1016/0168-9002(88)90062-9.

[12] D. Rodriguez Sanmartin, D. Zhang, T. Button, C. Meggs, C. Atkins, P. Doel, D. Brooks, C. Feldman, R. Willingale, A. Michette, S. Pfauntsch, S. Sahraei, M. Shand, A. James, G. Willis, C. Dunare, T. Stevenson, W. Parkes, and A. Smith. "Development of spider micro-structured optical arrays for X-ray optics". In: *Proceedings of the SPIE - The International Society for Optical Engineering* (2010), 780306 (11 pp.) DOI: 10.1117/12.860420.

Chapter 4

Characterisation of Microstructured Optical Arrays

4.1 Introduction

The majority of this chapter deals with experimental tests performed to evaluate the focusing characteristics of MOAs using the microfocus source described in chapter 3. A MOA mounted within the manipulator described in section 3.4 may be translated and aligned with respect to the X-ray source, and the CCD detector will record the resulting X-ray distribution. Translating the MOA relative to the optical axis in this way allows the X-rays focused using single reflections from the channels to be identified and isolated from radiation passing through the structure without reflection, at the detector plane. The initial experiments presented within this chapter use the broadband aluminium X-rays produced by the microfocus source to estimate the performance of both a first and a second generation MOA. One of the key advantages of measuring the reflectivity of MOAs in this way is that results may be compared with the simulation routines described in section 2.7, where all reflecting channels are assumed to lie parallel to the optical axis.

The chapter also describes other methods used to test the performance of MOAs.

This includes a summary of alternative experiments, used to estimate the reflectivity of MOAs, allowing comparison to be made with the results obtained using the microfocus X-ray source. The methods described within this chapter to optically characterise MOAs may also be extended, allowing measurement of both actuated and multiple reflection MOA systems.

4.2 Methods for characterisation of MOAs

Two methods for producing MOAs have been outlined in section 2.5.1. These have been successfully used to produce three generations (also described in section 2.5.1) of MOA channel structures [1]. Of these two production methods, the anisotropically etched (TMAH) second and third generation MOAs have been found to contain smoother channel walls than the first generation (DRIE).

The physical dimensions of the three MOA generations produced are summarised in table 4.1. While each of the three generations may be characterised using the microfocus X-ray source, the third generation will not be considered experimentally within this thesis as it is assumed that the channel structure (and therefore surface quality) will be comparable to that of the second generation. All MOAs evaluated within this chapter are also unactuated, and therefore a parallel channel structure that lies approximately along the optical axis defined by the X-ray source and CCD detector may be assumed. While the third generation will not be considered, this type of MOA will be most useful for experiments performed in the future when actuated MOAs are examined, as they are able to achieve the smallest radius of curvature currently measured.

The performance of a MOA is characterised within this chapter by two main factors, both of which may be extracted from the total intensity distribution resulting at the detector plane using only single reflections from the channel walls of a MOA. More specifically, the physical width of the distribution redirected by the MOA at

Table 4.1: Summary of dimensions for each of the three MOA generations. Where a rectangular shape is indicated, the long dimension corresponds to the direction of curvature (figure 2.16).

Generation	first	second	third
Production method	DRIE	TMAH	TMAH
Thickness [μm]	200	100	100
MOA size [mm]	20×10	20×10	20×20
Channel width [μm]	10	10	4
Pitch [μm]	20	20	12
Active area [mm]	3×3	2×2	2×2

the detector allows the size of a typical focused image to be estimated, while the intensity of this distribution indicates the efficiency of the reflecting channels, by comparison to the unreflected radiation passing through the open channels of the MOA. It is therefore convenient to obtain an intensity distribution containing only X-rays reflected once by the MOA. Figure 2.22 shows the simulated X-ray intensity distribution, when both the source and MOA are located on the optical axis. This simulation shows the changes in this distribution as the detector plane is translated along the optical axis, and the focused image of a point source is shown to fall within the shadow of the central stop of the MOA (where the distance between the MOA and detector z' is equal to the source to MOA distance z). At a MOA to detector distance of z_{d} either side of this image, the reflected radiation will overlap with the unreflected "background". While figure 2.22 describes the simplest scenario, the finite size of the microfocus X-ray source, as described by chapter 3 will produce a reflected distribution larger than the shadow of the central stop, and the focused image reflected by the MOA will overlap with the background passing through the MOA channel.

An alternative method to separate the reflected radiation from the unreflected background translates the entire array of MOA channels from the optical axis by

a distance y_T, as shown in figure 4.1. This will produce an asymmetric focusing effect of the radiation about the optical axis. As the channels remain parallel to the optical axis at all times as y_T is increased, the array of channels will still behave as an unactuated MOA, only with a slightly larger grazing angle at the outermost channel. The sample manipulator of the microfocus source is capable of producing such a translation, and so by scanning the MOA vertically across the X-ray optical axis, changes in the position and distribution of the reflected radiation may be observed. When the detector is located at the image plane of the MOA ($z = z'$), and the reflecting channels are all parallel to the optical axis, the position of the focused radiation reflected onto the detector will remain constant as the MOA is vertically translated – only the unreflected background projected through the channels will fall at different positions on the detector.

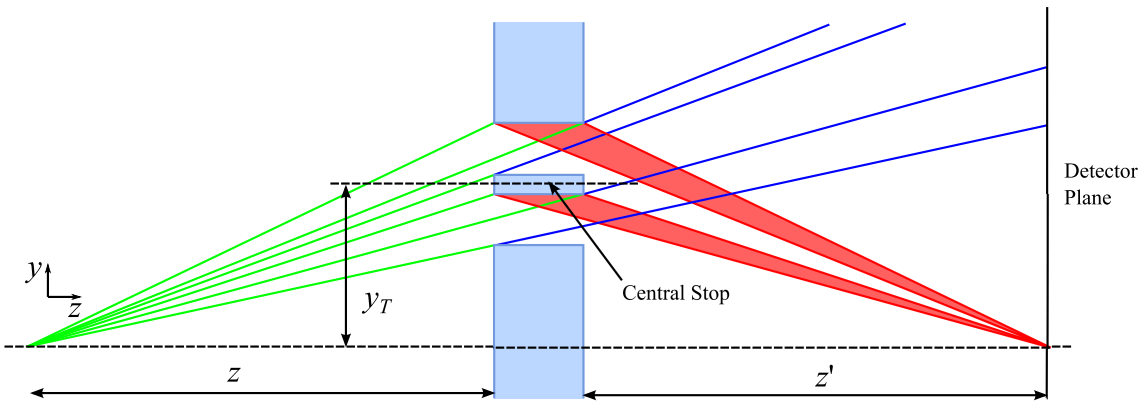

Figure 4.1: Translating the MOA by a distance y_T from the optical axis will separate the focused (single reflection) from the unreflected background at the detector plane.

Placing the detector in a plane at a position either before or after the image plane (where a focused image of the point source is not achieved as $z_d \neq z'$), and translating the MOA perpendicular to the optical axis in a similar manner will change the position of both the reflected and background distributions, while still separating the singly reflected X-rays from the background. The position of the focused X-rays will not remain constant as the reflected X-rays will converge towards

the image plane where $z_d < z'$, and diverge from the focused spot beyond the focus ($z_d > z'$). This has been simulated using the routines described in section 2.7, with the resulting positions shown for a second generation MOA in figure 4.2, where $z = 170\,\text{mm}$, and $z_d = 250\,\text{mm}$. The position of the resulting distribution reflected (red) by the channels moves in the opposite direction to the unreflected background (as $z < z_d$), and is quickly separated from the background after a vertical MOA translation y_T of about 1 mm. The further away the detector is from the image plane of the MOA, the larger this movement of the reflected distribution becomes.

It should also be noted that the width of the distribution of reflected radiation is smallest at the image plane of the MOA (figure 2.22). If the detector is far from this focused spot, this results in a lower intensity signal detected. It may therefore not be suitable to position the MOA far from the image plane, as the X-rays will be spread over a larger area.

4.3 Experimental characterisation of MOAs using the microfocus X-ray source

Initial focusing tests performed using second generation MOAs with the microfocus source are shown in figure 4.3. The measurements allow a comparison to be made between the simulation shown in figure 4.2 by translating the MOA across the optical axis of the microfocus source, where the axial distances are set to $z = 170\,\text{mm}$, and $z_d = 250\,\text{mm}$. Figure 4.3 shows a sequence of images taken as the MOA is translated using the sample manipulator, changing the separation between the MOA central stop and the optical axis. The intensity scale, exposure time and emission properties of the microfocus source are kept constant for each image within the sequence.

Figure 4.3 shows a central bright (white) region, where X-rays are able to pass through the open channels of the MOA to the detector without reflection. This

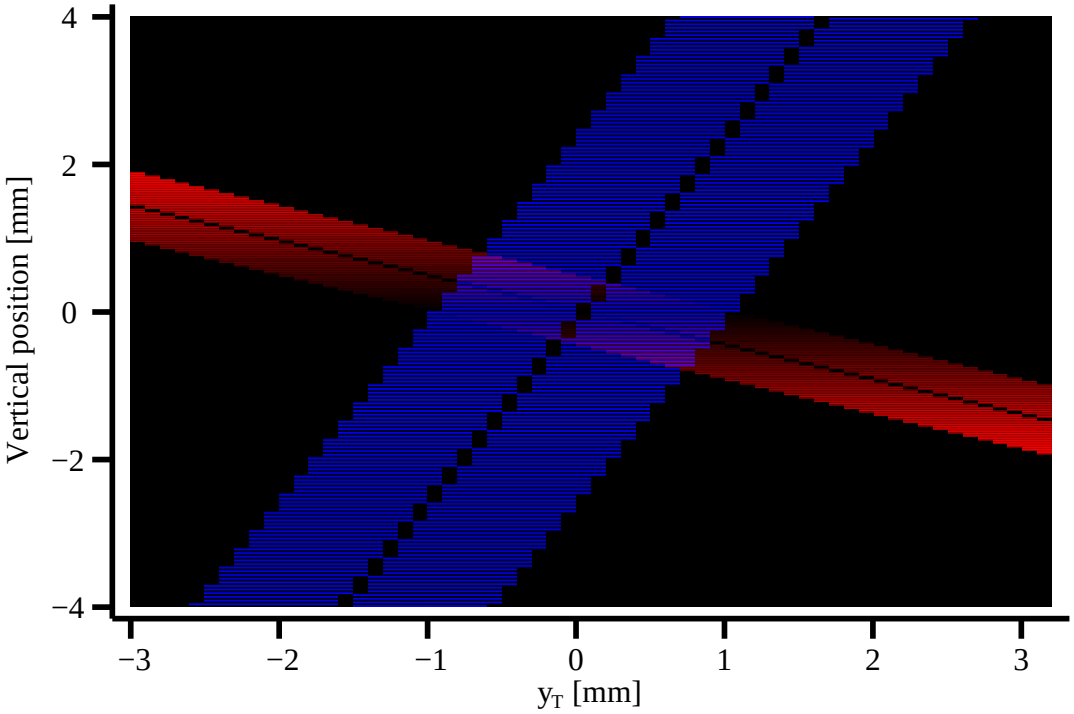

Figure 4.2: Simulation of the translation of MOA channels across the optical axis where the detector is positioned beyond the image plane of the MOA ($z < z_d$). Radiation reflected (red) by the channels quickly becomes separated from the unreflected (blue) background at the detector plane. Where the detector is positioned at the focal plane of the MOA, there is no change in the position of the reflected radiation as y_T is translated.

central band is equivalent to the blue band shown in figure 4.2. Directly above the central unreflected region in each image is a low intensity band of radiation, the horizontal width of which is the same as the active area of the MOA, as determined by the unreflected background. This band has been identified as the X-ray distribution resulting from the combined single reflections from the MOA channel walls. In order to show the position of this low intensity reflected band, the intensity scale of each image has been limited to a value well below the full range of the CCD, with all intensity values recorded above this limit displayed as white. As the MOA is translated vertically using the manipulator, the position of the central unreflected region at the CCD moves in the same direction. This is expected, as radiation passing straight through the channel structure will project a shadow image

of the MOA onto the detector. The position of the reflected band also appears to shift vertically by a small amount, as predicted by figure 4.2. However, in order to confirm the focusing effects described, the band of reflected intensity needs to be observed at positions both above and below the central unreflected region.

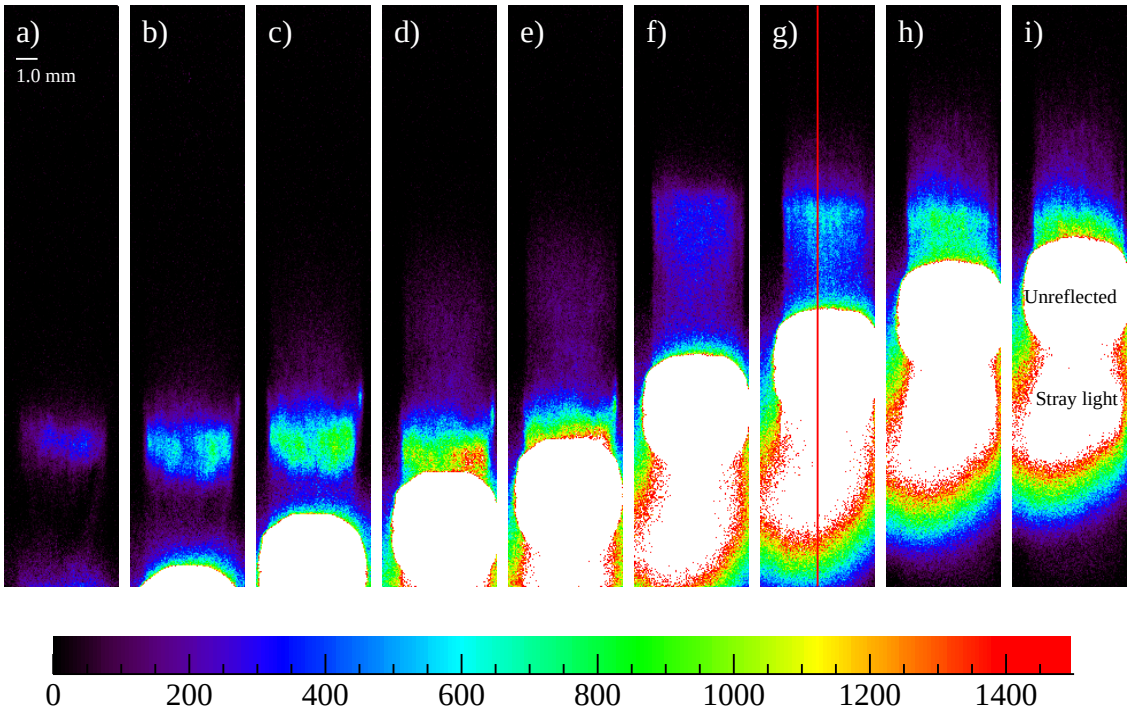

Figure 4.3: Initial testing of second generation MOA shows a horizontal band in each image panel above the unreflected radiation that grows in intensity as the MOA is translated vertically across the optical axis. This band has been identified as the radiation focused by reflection of the MOA channel walls. This reflected band is not visible below the unreflected region due to the large level of stray light passing through the MOA.

As the images shown in figure 4.3 were taken before installation of the X-ray shutter, only the central segment of the detector is recorded as a region of interest. This reduces the readout time of the image to the PC, minimising the horizontal band shown in figure 3.7 a), and allows the low intensity band due to the reflected X-rays to be more easily observed at a position above the higher intensity unreflected background. As shown in figure 4.2 however, the reflected band should be visible both above and below the background. Despite the visible light filter (2 μm thick Ti

foil) placed directly upstream of the active area of the MOA, the reflected band is not observed below the unreflected background due to the large level of stray light. The position of the reflected band that is visible appears to shift dramatically as the MOA is translated between images e) and f) in the sequence. This is believed to have been caused by a mechanical instability in the vacuum feedthrough of the manipulator, causing the angle between the optical axis and MOA (therefore the grazing reflection angle) to change, and reflecting the radiation towards a different position on the detector. This feedthrough has since been replaced, and all further results presented within this chapter do not show this instability.

While the preliminary results shown in figure 4.3 may not be used to fully characterise a MOA, comparisons can be made with simulated results [2]. This is shown in figure 4.4, for the region highlighted by a vertical red line in figure 4.3. By selecting an appropriate MOA displacement (y_{T}), the reflected distributions overlap when the shadow of the central stop is aligned between the simulated and experimental distributions.

The simulated distribution (black) in figure 4.4 shows the separation of reflected and unreflected radiation at the detector plane when the MOA channels are displaced from the optical axis by $y_{\mathrm{T}} = 2.5\,\mathrm{mm}$. When the shadow of the central stop for both experimental and simulated data are aligned, the central position of signal due to single reflections also approximately overlap. A significant difference in both the intensities and physical distribution on the detector is evident between the simulated and experimental results. For example there is a difference greater than an order of magnitude between the peaks (reflected and transmitted) measured experimentally, while the simulated results show a comparable intensity between the two distributions. The distribution due to radiation reflected by the MOA is found to be broader than that simulated. While the simulation only considers a point source, the size of the microfocus X-ray source is far larger ($\approx 200\,\mu\mathrm{m}$) in diameter.

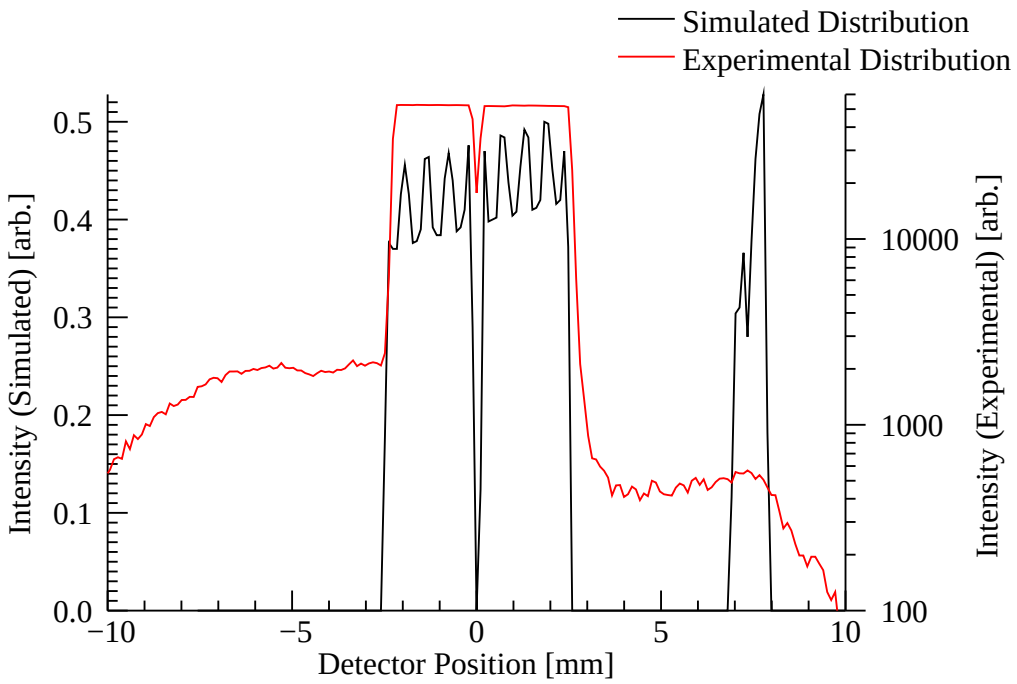

Figure 4.4: Comparison of resulting intensity distributions of a MOA. The region taken for the experimental distribution (red) is highlighted by the vertical line in figure 4.3. It is shown that the two distributions overlap at approximately the same place on the detector when the simulated MOA is displaced by a distance of $y_T = 2.5\,\text{mm}$ from the optical axis.

This will broaden the distribution of the focused radiation significantly (see figure 2.23).

Following installation of the X-ray shutter described in section 3.3.1 the stray light passing through the MOA was drastically reduced, allowing the reflected radiation to be separated on the detector from the unreflected background as the MOA is translated across the optical axis. The shutter also eliminated the horizontal band recorded by the detector due to the continuous exposure during readout of the collected image to the PC, allowing the full CCD chip to be recorded at each position of the manipulator. A sequence of the intensity distributions obtained is shown in figure 4.5. The stray light previously observed below the unreflected background in figure 4.3 has been eliminated from the final images, and visible light from the

X-ray source has been prevented from reaching the CCD by a 40 nm thick Ti filter coated on a 50 nm thick silicon nitride membrane mounted on the shutter.

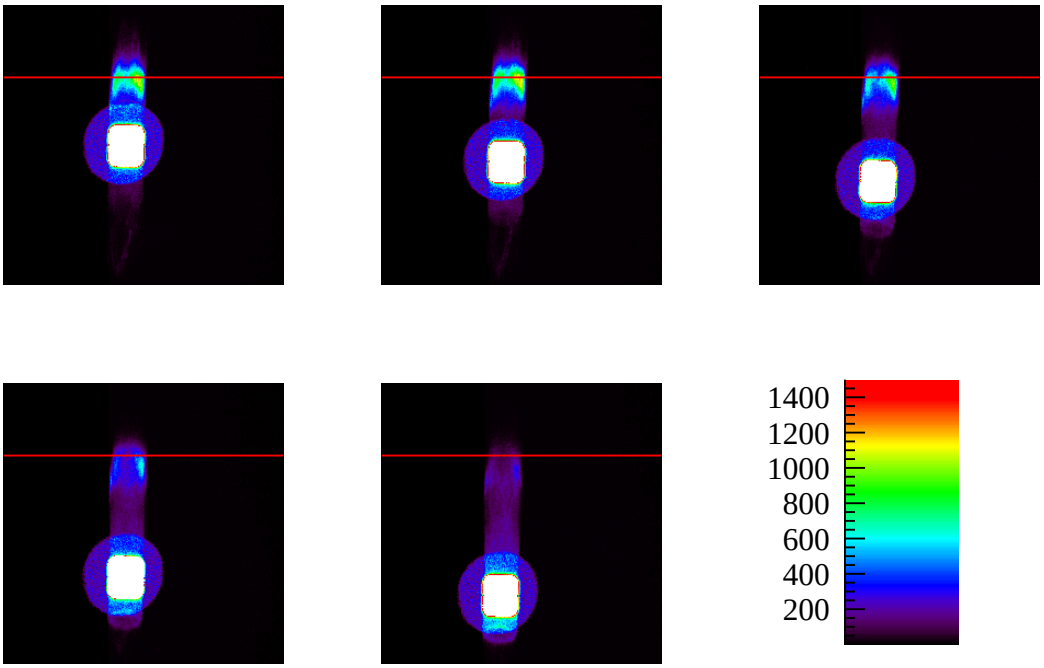

Figure 4.5: MOA reflectivity images for a second generation MOA captured after installation of the CCD detector and X-ray shutter. Hard X-rays penetrating through the silicon substrate of the MOA are visible as a low intensity disc surrounding the (white) unreflected radiation. In each image, the central vertical position of the reflected band is identified by a horizontal red line.

Each of the images within the sequence shown in figure 4.5 is contaminated by a circular disc of a constant low intensity surrounding the unreflected central region. This corresponds to the dimensions of the circular aperture (of diameter 3 mm) of the mount supporting the MOA in the manipulator. This additional background is due to the higher energy X-rays emitted by the microfocus source that penetrate through the 100 µm thick silicon substrate of the second generation MOA and travel to on the detector. As shown in the preliminary results (figure 4.3), the band of reflected radiation was once again observed, with the centre of the distribution approximately indicated by the red horizontal line for each image in the sequence. The position

of the central peak of reflected radiation does not appear to move significantly as the MOA is translated as expected, as the detector is positioned close to the image plane of the MOA, as $z \approx z' \simeq 300\,\text{mm}$.

The improved sequence of images presented in figure 4.5 shows that X-rays reflected by the MOA may be spatially separated at the detector from radiation passing through the channel structure without reflection. This may be observed at a manipulator position both above and below the optical axis following installation of the X-ray shutter. The focusing properties of typical MOA structures can now be estimated, by analysis of the shape and size of the reflected distribution produced.

4.3.1 Optical performance of MOAs

The sequences of CCD images shown within section 4.3 may be used to evaluate the focusing properties of a MOA when the distribution due to single reflections by the channel walls is separated at the detector plane from radiation passing through the MOA without reflection. A sequence of reflection images produced using a first generation MOA is shown in figure 4.6.

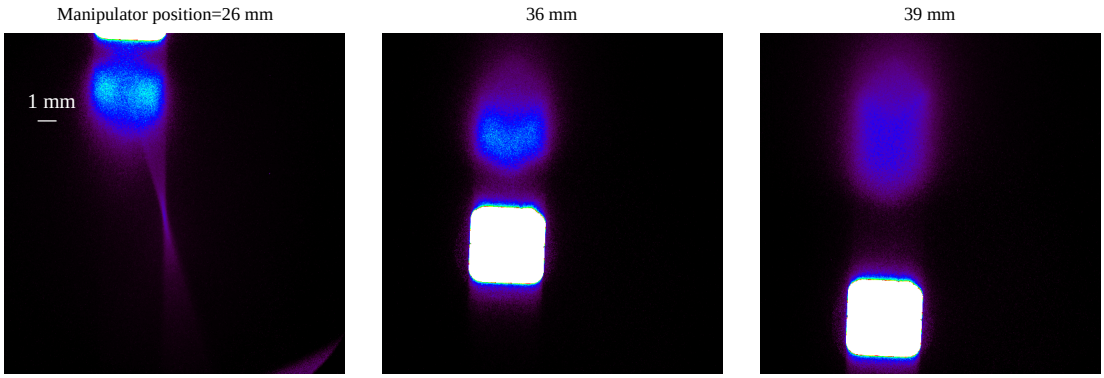

Figure 4.6: Reflectivity images produced using a first generation MOA.

Each of the images shown here is linked to the position of the linear manipulator. Radiation reflected by the MOA is also clearly visible at positions both above and

below the unreflected background. The left hand image at a manipulator position of 26 mm shows the unreflected radiation at the very top of the detection area of the CCD, with a stray light signal visible. This stray light is caused by X-rays passing underneath the sample manipulator, and is undesirable, however this particular position has been selected as the reflection is clearly isolated from the background.

The reflected radiation has been approximated to a Gaussian distribution for each reflectivity image shown in figure 4.6, thereby allowing the width (FWHM), peak intensity and central position on the vertical axis of the CCD detector to be examined further. This then allows comparisons to be made across the range of travel of the manipulator. The Gaussian function is fitted using the GAUSSFIT function in IDL, computing the fit using a non-linear least squares fit, specifying three resultant terms.

A vertical intensity line-profile through each of the reflectivity images introduced in figure 4.6 are shown in figure 4.7, with the corresponding Gaussian fit plotted as a dashed line. It is seen that the Gaussian fits do approximately describe the intensity profile of the reflected radiation. At each manipulator position, the distribution due to the unreflected background reaches a plateau of constant intensity, with a long tail extending most of the width of the CCD. This tail therefore overlaps with the reflected distribution, potentially distorting the fitted Gaussian curve.

In order to characterise the tail of the unreflected background, an exponential fit has been applied to a region of the line profile where the reflected radiation is not observed. This was chosen for the manipulator position of 26 mm, shown in by the red line in figure 4.7, between 0 and 10 mm. This fitted line may then be subtracted from the original distribution, with the aim of improving the fitted Gaussian. The best exponential fit obtained for the example given was found to be,

$$y = 2.7 \times 1.2^{x} + 10.9. \tag{4.1}$$

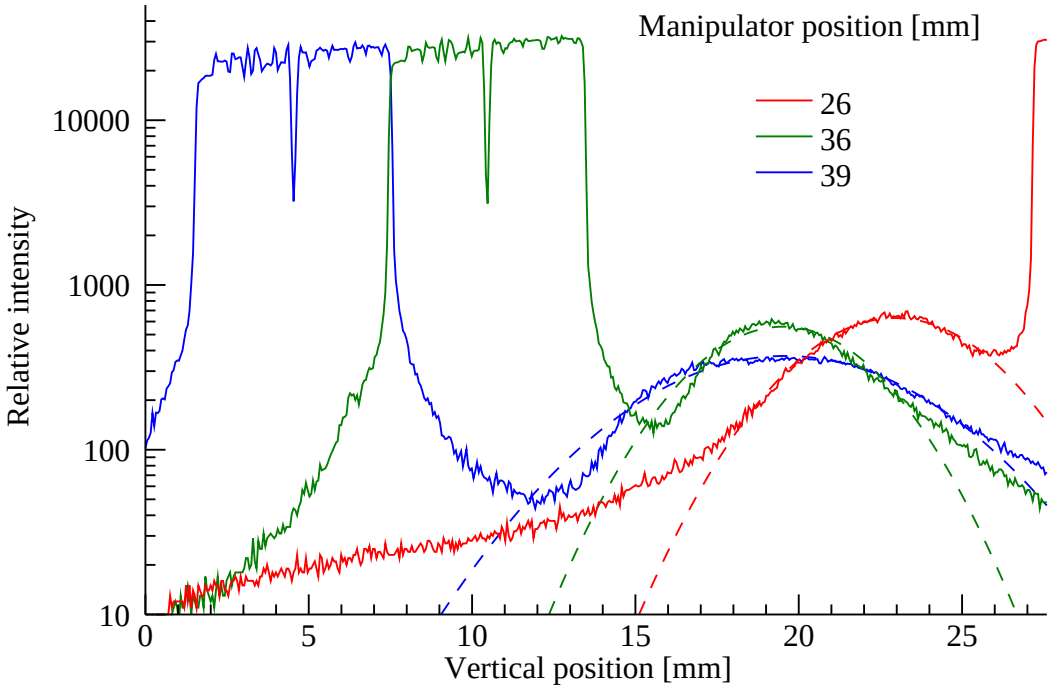

Figure 4.7: Cross-sectional intensity distributions (solid lines) produced by a first generation MOA, for a range of different manipulator distances. For each position of the manipulator the distribution due to the reflected X-rays has been fitted to a Gaussian curve (dashed lines).

This fitted line was subtracted from the original, and the difference between original and fitted Gaussian distributions is shown in table 4.2.

Table 4.2: Comparison between original and subtracted Gaussian fits for the reflected contribution from a first generation MOA.

Gaussian Parameter	Original line (fitted)	Subtracted line (fitted)
Intensity [counts]	630.1	446
CCD position [mm]	22.95	22.39
FWHM [mm]	6.4	4.4

The Gaussian fits are shown in figure 4.8, for the original line, and the resulting Gaussian distribution profile following subtraction tail. The fitted line shown in blue corresponds to the exponential fit. Table 4.2 shows that it is possible to alter the Gaussian fit applied, potentially achieving a closer result to the actual distribution of

reflected radiation. In order to perform this, the tail of the unreflected background needs to be clearly observed to allow fitting to occur. As this is only seen when the manipulator position is 26 mm, such processing will not be considered further within this chapter.

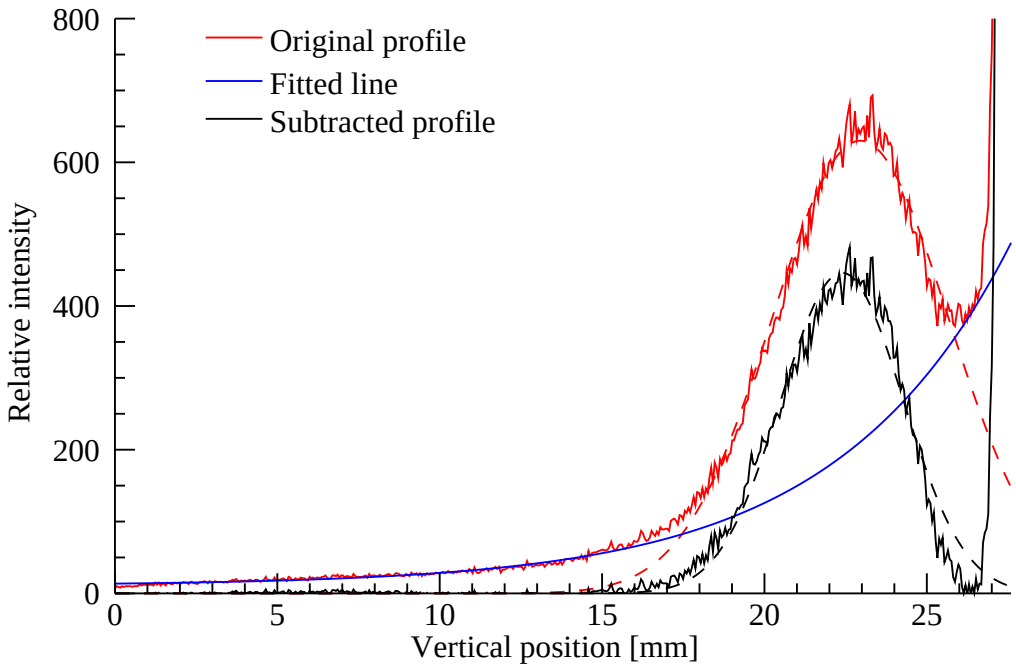

Figure 4.8: Comparison between the original and subtracted Gaussian fits to the reflected radiation.

As the MOA is translated across the optical axis, any changes in the position of the reflection falling on the detector may be determined. Figure 4.9 shows this change in position for a first generation MOA, where the detector is positioned approximately at the image plane of the MOA ($z \approx z' \simeq 300\,\text{mm}$). At each position of the manipulator, the centre of the Gaussian distribution fitted to the reflected radiation is plotted, along with the centre of the unreflected background, identified by the position of the central stop shadow. The position of the reflected distribution is shown to move linearly across the detector about each side of the optical axis, however to a lesser degree than the central stop. As described in section 4.2, where

the MOA is positioned such that $z = z'$, the position of reflected radiation on the detector does not change. The linear translation of the reflection across the detector plane therefore indicates that the detector is positioned slightly beyond the image plane of the MOA, ($z < z_{\mathrm{d}}$). The slope of both the reflection and background shown in figure 4.9 does follow that shown in figure 4.2, however as the detector is positioned well beyond the focus of the MOA in the simulated results, the slope is larger than that observed experimentally.

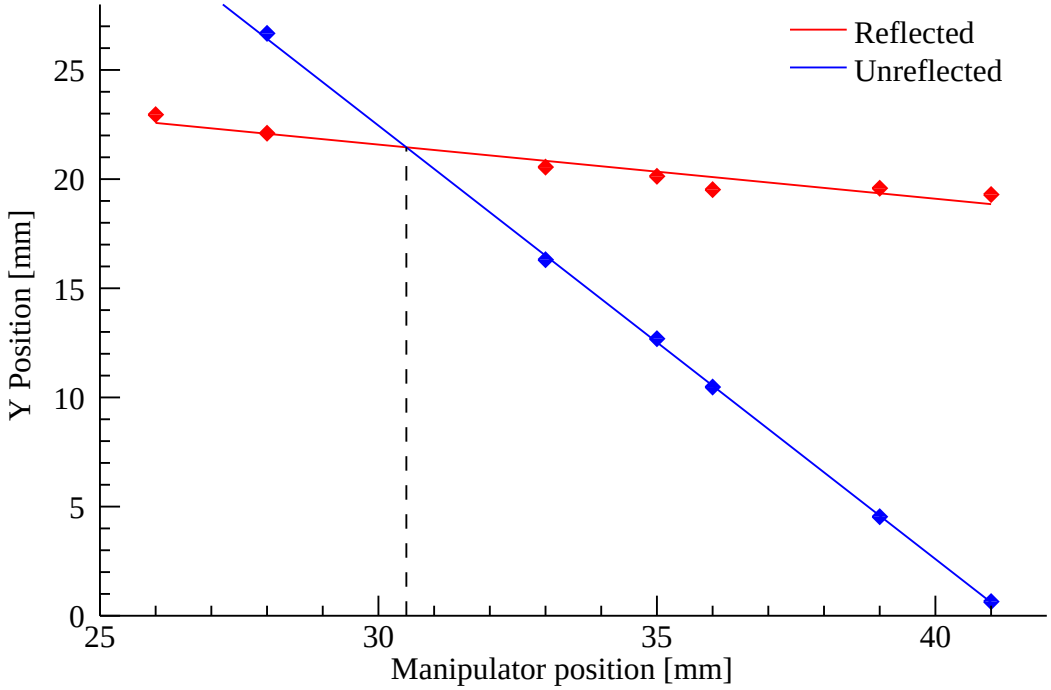

Figure 4.9: Fitted central peaks for both distributions both reflected and unreflected by a first generation MOA.

The intersection of the lines of best fit shown in figure 4.9 may be used to the manipulator position where $y_{\mathrm{T}} = 0\,\mathrm{mm}$, and the central stop of the MOA lies on the optical axis. This is shown by the dashed line to occur at a manipulator position of 30.5 mm. Using this intersection as a calibration factor, the manipulator positions may be displayed in terms of y_{T}. As the translation y_{T}, and z are known, the grazing reflection angle (θ) for channels close to the central stop of the MOA may be

estimated at each position of the manipulator. The typical grazing angles calculated are shown in table 4.3, and are displayed with the corresponding reflectivity of silicon at the characteristic emission energy of the microfocus source (Al $K_\alpha = 1.487\,\text{keV}$). The grazing angles calculated are shown to be both above and below the critical angle for grazing incidence reflection, as the reflectivity is low for large values of y_T. This should be represented by a substantial decrease in the X-ray intensity observed at the detector at large values of y_T.

Table 4.3: Approximate grazing angles for the DRIE etched MOA translated across the optical axis, presented in figure 4.9. Reflectivities given are approximated for Si at Al K_α=1.487 keV.

Manipulator position [mm]	y_T [mm]	θ [deg.]	Reflectivity
41	10.5	2.07	0.01
39	8.5	1.67	0.02
36	5.5	1.09	0.5
35	4.5	0.89	0.9
33	2.5	0.49	0.95

The same methods have been applied to the reflected radiation from a second generation MOA, with the results shown in figure 4.10. The translation of the manipulator is over the same range as those presented in figure 4.9, with identical distances of z and z_d. As shown for a first generation MOA, the position of the Gaussian distribution fitted to the reflected radiation translates linearly about each side of the optical axis as the MOA is moved.

Unlike a first generation MOA however, figure 4.10 shows that there is a shift in the vertical position of reflections on either side of the optical axis, highlighted by the two red lines of best fit. This is clearly different to the behaviour previously shown in figure 4.2 for an array of parallel reflecting outer channel walls, where radiation is re-directed towards a common point on the detector when the MOA is above or below the optical axis. The shift in the reflected image about each side

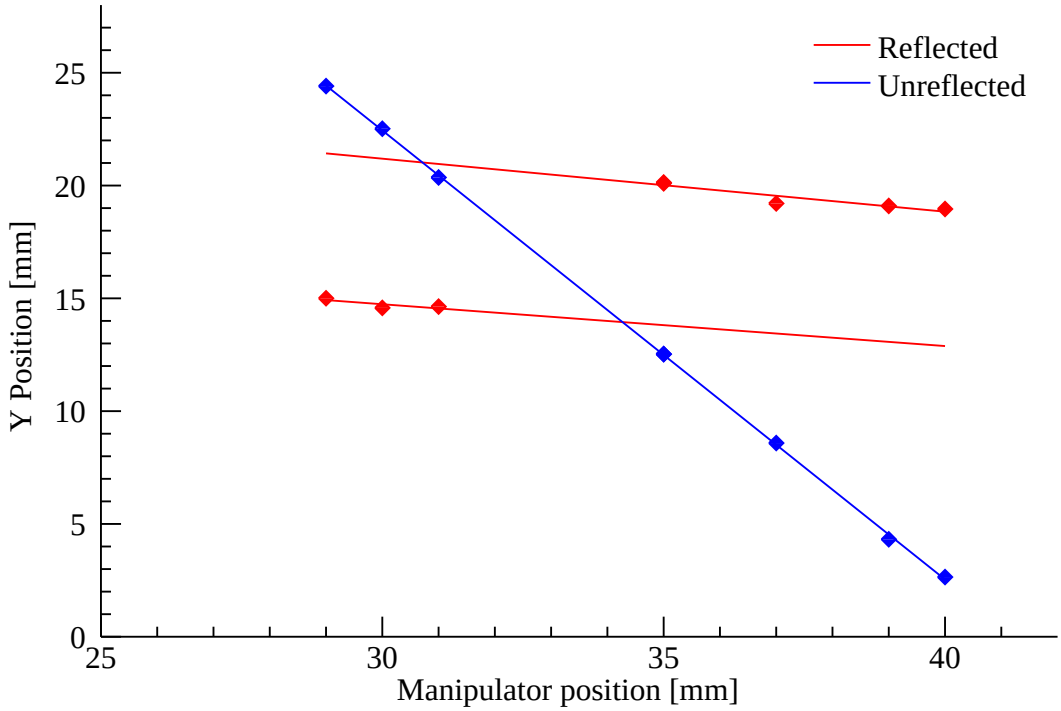

Figure 4.10: Fitted central peaks for both distributions both reflected and unreflected by a second generation MOA. Radiation is reflected towards a different point on the detector depending on the position of the MOA with respect to the optical axis.

of the optical axis may be explained by introducing a small angular misalignment of around $< 1°$ between the channel walls, describing a slight taper to the channel structure. The reflecting channel walls will therefore no longer be parallel to each other (or the optical axis). If the MOA is translated asymmetrically about one side of the optical axis, the position of the radiation remains in a constant position on the detector as the reflection occurs from the outer channel wall. As the MOA is translated to a position on the other side of the optical axis, the reflection then occurs from the opposite channel wall. This tapering of the channel walls therefore separates the reflections into two images, each of which is focused to a different image position (where $z = z'$). This double image will only be formed when the active area containing the reflecting channels of the MOA is crossing the optical axis, and reflection will occur at both sides of the tapered channel. As the intended

configuration for MOAs is to position the central stop of the MOA on the optical axis, with the focused spot formed within the shadow of the central stop, this effect must be understood further before second generation MOAs are used within a microprobe.

Once the reflected radiation has been separated from the unreflected background by displacing the MOA from the optical axis, the detector may also be translated axially through the image plane of the MOA, once again changing the X-ray distribution, allowing investigation of the focusing properties of the array. The change in separation between the distributions (reflected and unreflected) resulting from the MOA will also change as the detector is translated. This is shown for a second generation MOA in figure 4.11, for a fixed manipulator position of 3.2 mm. As the detector is translated along the optical axis, the separation between the centres of the two distributions increases from 6.2 mm to 7.6 mm.

As the X-rays passing through the MOA without reflection are diverging from the microfocus source, the shadow image of the MOA projected onto the detector will both increase in size and shift in position as the detector is translated away from the MOA. Using the same argument for reflected X-rays diverging away from the image plane of the MOA means that the separation between the centres will also increase.

4.3.2 Comparison between first and second generation MOAs

The focusing effect for both first and second generation MOAs has been characterised in section 4.3.1 by plotting the central position of the Gaussian distribution fitted to the reflected radiation as the MOA is translated in a direction perpendicular to the optical axis. The change in position has been shown to be linear for the first generation (figure 4.9), and linear about each side of the optical axis for a second generation MOA (figure 4.10) with the shift potentially caused by a tapered channel

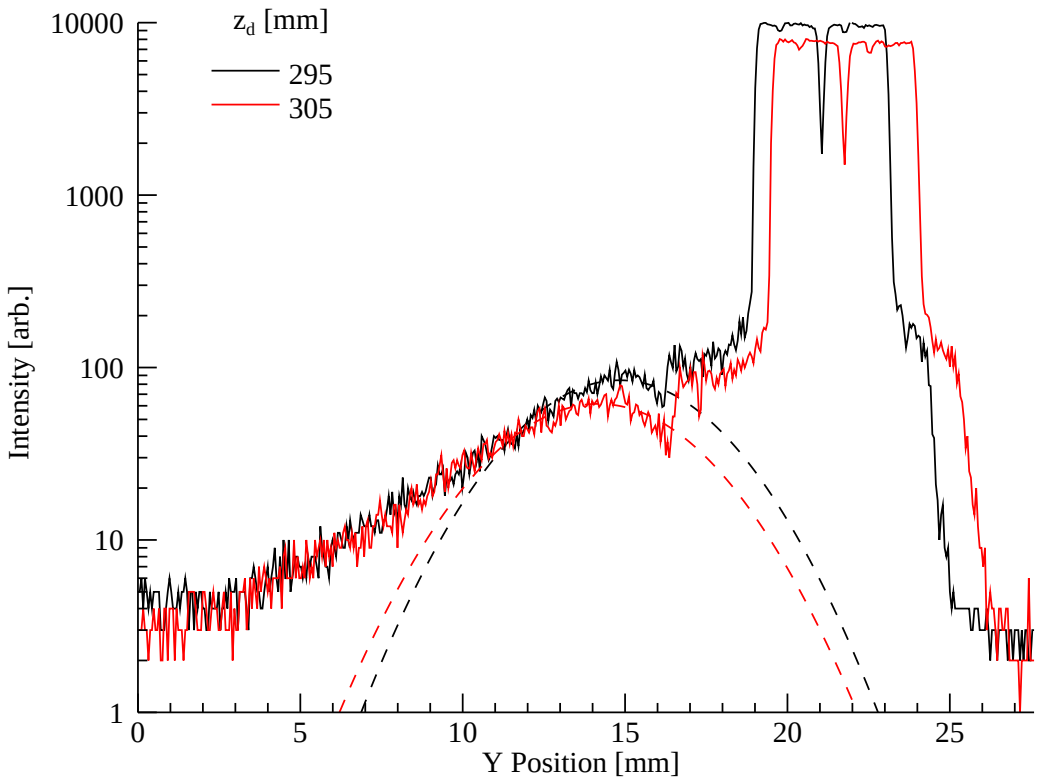

Figure 4.11: Translation of the MOA along the optical axis will change the separation between the centre of the two distributions.

structure. This has not however described either the size of the focused distribution obtained or the relative efficiency.

Figure 4.12 shows the FWHM of the reflected Gaussian distribution fitted to both the first and second generation MOAs described in section 4.3.1, as the MOA is translated across the optical axis using the sample manipulator.

The Gaussian FWHM obtained for both first and second generation MOAs are shown in figure 4.12 to follow a similar curve, with the smallest width for each occurring at a manipulator position corresponding approximately to $y_T = 0\,\text{mm}$. Figure 2.1 has shown that the X-ray distribution reflected towards the focus increases in width as it travels along the optical axis. This width is determined by the range of angles for which a reflection may potentially occur within a single channel, and will

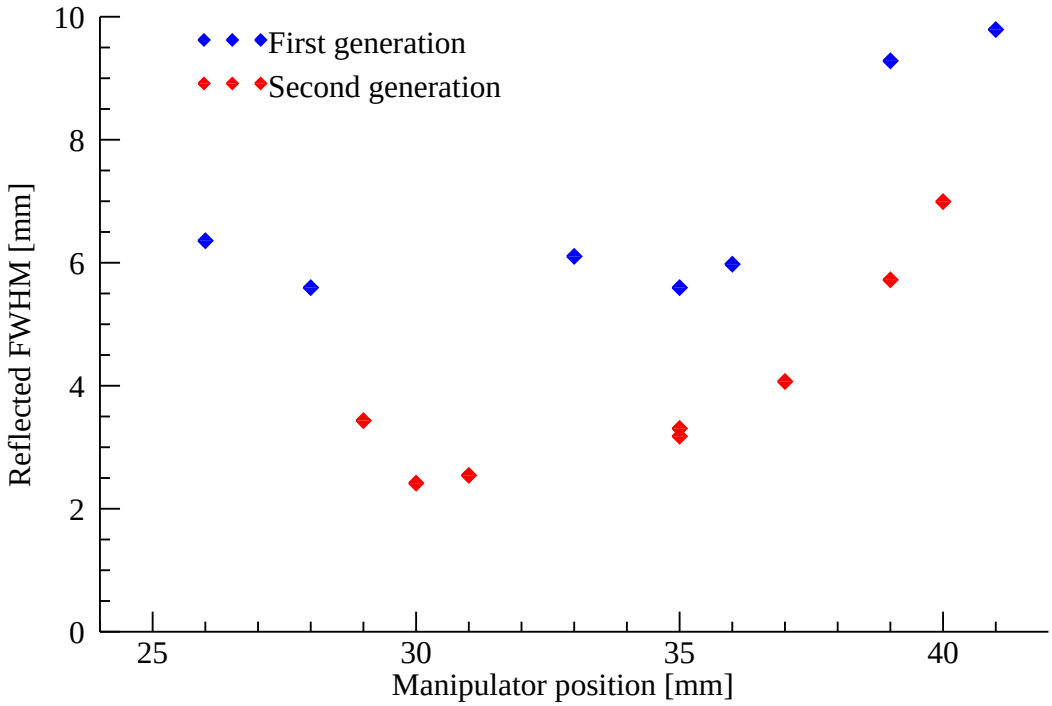

Figure 4.12: Comparison of the Gaussian FWHM obtained for both first and second generation MOAs.

increase as the channel is displaced further from the optical axis. As this is true both for the active area of the MOA, and also as the entire array of channels is translated, large displacements of y_{T} show the largest distributions of reflected radiation. Table 4.1 shows that the substrate thickness of first generation of MOAs produced is double that of a second generation, resulting in twice the reflecting channel length. This will also increase the width of the Gaussian distribution obtained for the first generation MOA, as the range of angles from the source with the potential for reflection is also increased.

Comparison may also be made of the relative efficiency between first and second generation MOAs. To describe this, the intensity of the central peak (I_{r}) will be compared to the average intensity obtained within the plateau of the background (I_0). The efficiency is then described by the fraction $\frac{I_{\mathrm{r}}}{I_0}$. The efficiency is shown in figure 4.13 for both first and second generation MOAs. This figure shows that the

peak efficiency for each generation tested is obtained again where $y_T \approx 0\,\text{mm}$. This is consistent with table 4.3, as the reflectivity of Si for incident Al K_α X-rays quickly falls as y_T is increased. As only low energy X-rays are reflected at the larger grazing angles, they should only be present in the reflected distribution. The unreflected background however passes through the channels of the MOA without obstruction, and so the plateau of the projected image at the detector contains contributions from the broadband X-rays.

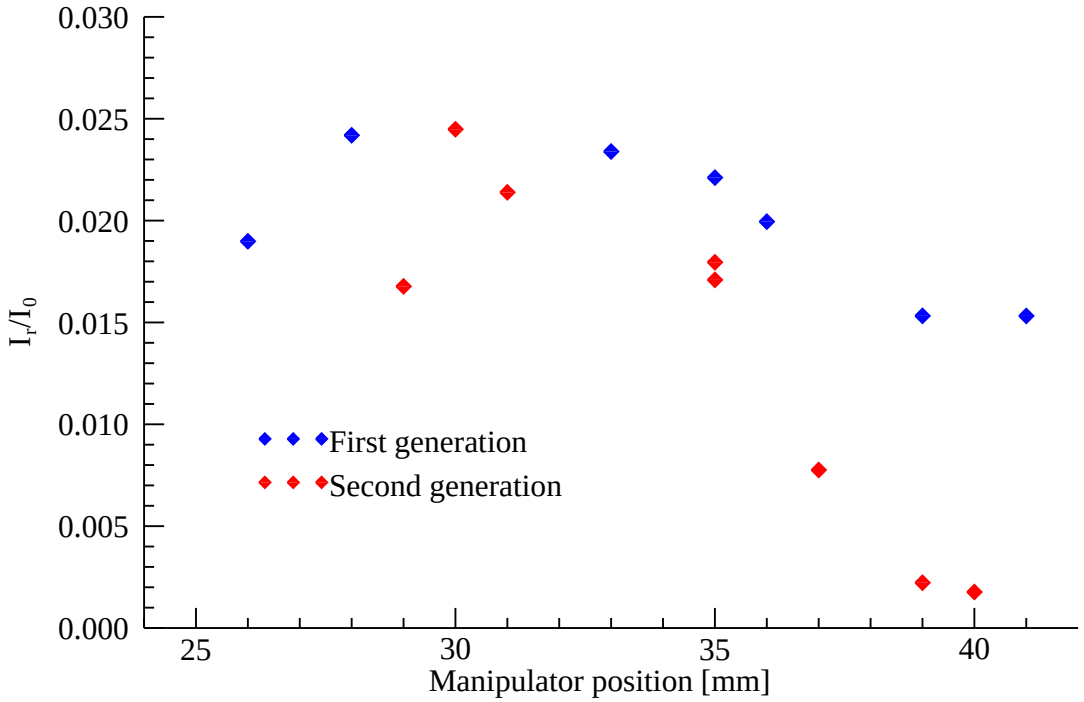

Figure 4.13: Comparison of the peak intensities obtained between first and second generation MOAs.

Between the first and second generation MOAs shown in figure 4.13, both appear to show a comparable efficiency, with a maximum at around 0.025. At large manipulator displacements from the optical axis the efficiency does appear to fall, indicating the removal of higher energy X-rays as previously described. The efficiency is only based on the peak values calculated for both the reflected Gaussian distribution, and background. A better estimate of the efficiency will include all

radiation contained within each distribution. In order for this to occur, further work is required in order to better determine the distribution of the background radiation, including the removal of the low intensity tail that has been shown in figure 4.8 to distort the reflected radiation.

4.4 Additional methods of optical characterisation

Optical testing of MOA samples has so far been performed on both first and second generation MOAs. Each of the test procedures has used rotation of the MOA in order to determine the reflectivity of the channel walls. Experimental results obtained both at the STFC Daresbury Laboratory, and at the University of Leicester have estimated reflectivities of $\sim 3\%$ for DRIE etched MOAs, and $\sim 5\%$ for the second generation [3]. Second generation MOAs have also been tested at the KMC-2 [4] beamline at the BESSY-II synchrotron. This used a collimated beam of 5 keV X-rays incident on a MOA, positioned at a centre of an axis of rotation. This allows the MOA to be rotated, introducing a defined tilt between the channels and the X-ray optical axis. A detector arm may also rotate around the axis, determining the angle of X-rays reflected from the channel walls relative to the optical axis. Considering equation (2.3) and figure 2.3, where $\alpha = 0$, the angular change in the X-ray path should follow the line $\alpha' = 2\varphi$. An example of the reflectivity map obtained by scanning the detector arm is shown in figure 4.14. This shows the X-ray intensity resulting as α' is scanned around the MOA, for a range of tilt angles φ is changed. The central white region corresponds to the unreflected X-rays passing though the MOA channels.

The diagonal dashed lines in figure 4.14 track the central position of the reflected X-rays as the MOA is rotated. The angle $\alpha' = 0$ indicates that radiation is parallel

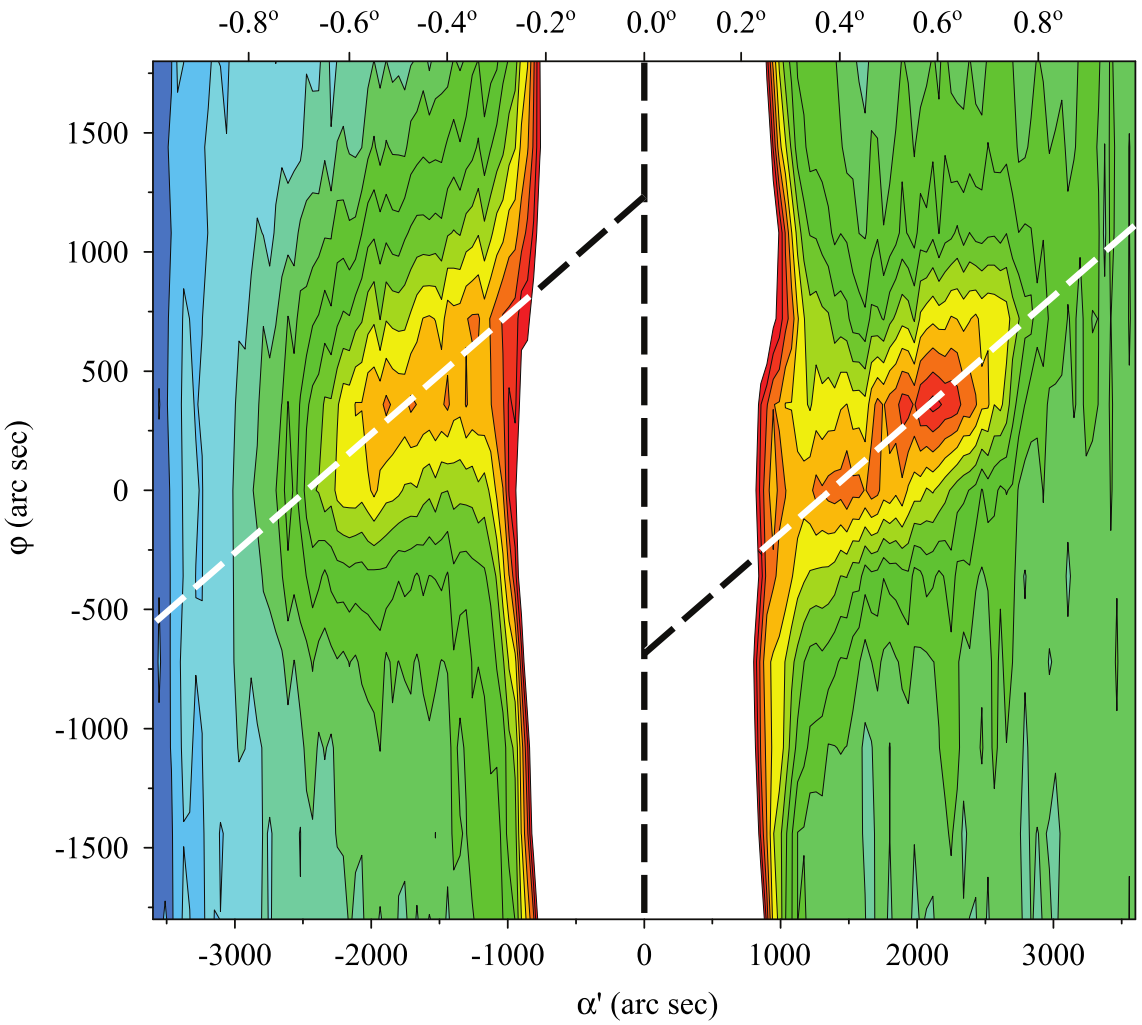

Figure 4.14: Angular distribution map obtained using the KMC-2 beamline at BESSY. 5 keV X-rays are reflected by a second generation MOA tilted to a fixed angle φ, while the detector is rotated through an angle α' (*Image provided by* A.Smith, STFC Daresbury).

to the optical axis upon reflection. This also corresponds to the tilt angle $\varphi = 0$. Where an offset in the angle φ is required to produce reflected radiation parallel to the optical axis, the channels therefore must be misaligned from the optical axis. A discontinuity indicates a misalignment between different channels within the array. The separation between the intersections of the lines with $\alpha' = 0$ may be used to estimate the total misalignment between the opposite channel walls. The separation between the dashed line indicates an angular misalignment of 0.56° between individual channel walls. This is a similar tapering effect within the channel

structure as seen in section 4.3.1 for a second generation MOA. Turning the MOA over, and illuminating the reflecting channels from the opposite side produces a similar result, with the effect of the misalignment still evident [5].

4.5 Summary

This chapter reported initial results on the characterisation of MOAs using the microfocus X-ray source. X-rays reflected by the MOA are shown to produce a Gaussian distribution, that may be isolated from the unreflected background on the detector by using a linear translation of the active area of the MOA. This effect has been shown for both first and second generation MOAs. Second generation MOAs indicate the formation of a double image, potentially introduced by a tapered channel structure. This tapering has been further supported by synchrotron measurements at BESSY-II.

References

[1] C. Dunare, W. Parkes, T. Stevenson, A. Michette, S. Pfauntsch, M. Shand, T. Button, D. Rodriguez Sanmartin, D. Zhang, C. Feldman, R. Willingale, P. Doel, H. Wang, A. Smith, and A. James. "Micromachining optical arrays". In: *2010 International Semiconductor Conference (CAS 2010)* (2010). DOI: 10.1109/SMICND.2010.5650215.

[2] M. T. Shand, G. R. Morrison, A. G. Michette, S. J. Pfauntsch, D. Hart, T. Stevenson, W. Parkes, C. Dunare, R. Willingale, C. Feldman, T. Button, C. Meggs, and D. Rodriguez-Sanmartin. "Characterization of Micro-structured Optical Arrays". In: *The 10th international conference on X-ray microscopy* 1365 (2011). Ed. by I. NcNulty, C. Eyberger, and B. Lai, pp. 453–456. DOI: 10.1063/1.3625400.

[3] C. Feldman. "Smart X-ray optics for large and small scale applications". PhD thesis. University of Leicester, Space Research Centre, Department of Physics and Astronomy, 2009.

[4] A. Erko, I. Packe, C. Hellwig, M. Fieber-Erdmann, O. Pawlizki, M. Veldkamp, and W. Gudat. "KMC-2: the new X-ray beamline at BESSY II". In: *AIP Conference Proceedings—AIP Conference Proceedings* no.521 (2000), pp. 415–18.

[5] A. Smith. Private Communication. Aug. 2010.

Chapter 5

Characterisation of a laboratory scale soft X-ray microscope

5.1 The McXI soft X-ray microscope

The McXI [1] (**Mic**roscope **X**-ray **I**n-vitro) project is a collaborative programme to develop a commercial tabletop soft X-ray microscope for in-vitro cellular imaging. This microscope is designed to deliver imaging of small biological samples using soft X-rays within the water window region, down to resolutions of 30 nm [2], allowing high resolution imaging to be routinely performed within a laboratory environment. Development of the microscope is undertaken within the project by three SMEs (Small and Medium Enterprises) with NANO-UV [3] (Paris, France), developing the soft X-ray source and integration within the prototype McXI-II system, Silson Ltd. [4] (Northampton, UK) delivering high resolution diffractive optics, filters and sample supports, and Delong Instruments [5] (Brno, Czech Republic) developing the vacuum system and mechatronics providing control and alignment of the microscope.

The work described within this chapter began at NANO-UV, undertaken as part of a Short Term Scientific Mission (STSM), supported by the COST MP0601 action, with the goal of characterising the performance of a prototype (McXI-I) microscope

system. Further work presented within this chapter has since been undertaken using the microfocus X-ray source and detector system at KCL (described in chapter 3). The aim of this work was to provide assistance in developing alignment techniques for the prototype microscope, and later to provide information on the focusing properties of diffractive optics developed by Silson Ltd. as part of the McXI project. Prior to discussing results obtained using the McXI-I system, a brief introduction to the properties of the McXI-II microscope will be given.

5.2 McXI microscope description

The McXI-II microscope is designed to provide X-ray imaging within the water window region (λ = 2.3 to 4.4 nm) to resolutions of 30 nm. This is implemented within a laboratory scale system, providing high resolution imaging without the use of large scale X-ray facilities such as synchrotrons. The water window X-rays used within the McXI-II microscope are produced by the CYCLOPS™ source, delivering both high brightness and low beam divergence [3]. The optical layout of the McXI-II microscope is identical to the TXM geometry shown in figure 1.9 a), whereby X-rays emitted by the source are focused by the Condenser Zone Plate (CZP) onto the specimen. A small diameter aperture, the Wavelength Selecting Aperture (WSA), positioned between the CZP and specimen is used to monochromate the X-ray beam [6] converging towards the focused spot, and to remove the unwanted diffraction orders. The resulting transmission image from the sample is magnified by the Micro Zone Plate (MZP) onto a scintillator screen converting the soft X-rays to visible light. This intermediate stage of magnification allows the overall system to be compact, as large path lengths are not required to produce the large magnifications [7]. This magnified image of the specimen is then further magnified by visible light optics. The McXI-II has been developed as a fully integrated, turnkey system in a vertical configuration, as shown in figure 5.1, with advantages such as a load lock

system providing simple and fast specimen handling within a small, compact table top design. The total height of the instrument is $\sim 2.0\,\mathrm{m}$, and is comparable in scale with an electron microscope.

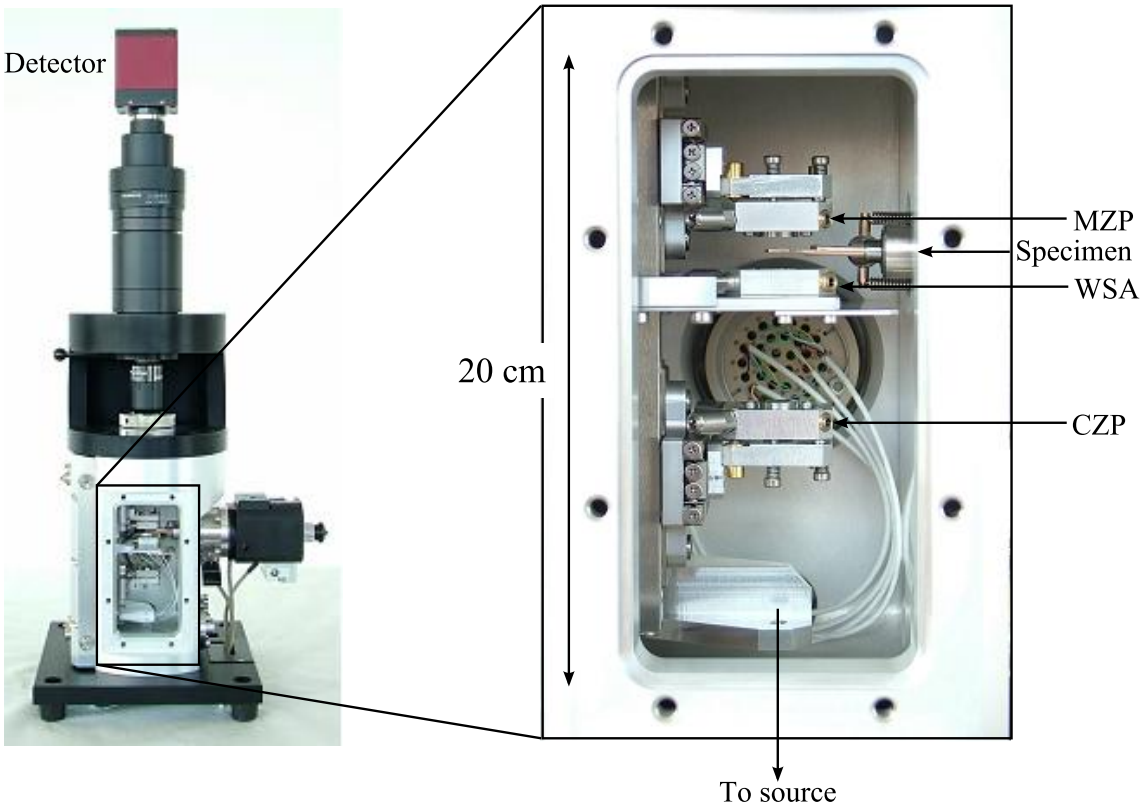

Figure 5.1: The McXI-II microscope developed by the McXI project. Soft X-rays from the source (not shown) pass through the small volume chamber (right), containing the optics, and form a magnified image of the sample of interest at the detector (*Images provided by* NANO-UV).

In order to aid the development of the McXI-II microscope, a prototype system (McXI-I) was produced. This prototype has been developed with a larger vacuum chamber and a horizontal configuration, with all of the optical elements and mechanical systems contained within representative of the final McXI-II design. The horizontal configuration of the McXI-I allowed the prototype microscope chamber (i.e. without the source and detector system) to be very easily coupled to the microfocus X-ray source and detector system in use at KCL. The McXI chamber installed on the microfocus source is shown in figure 5.2.

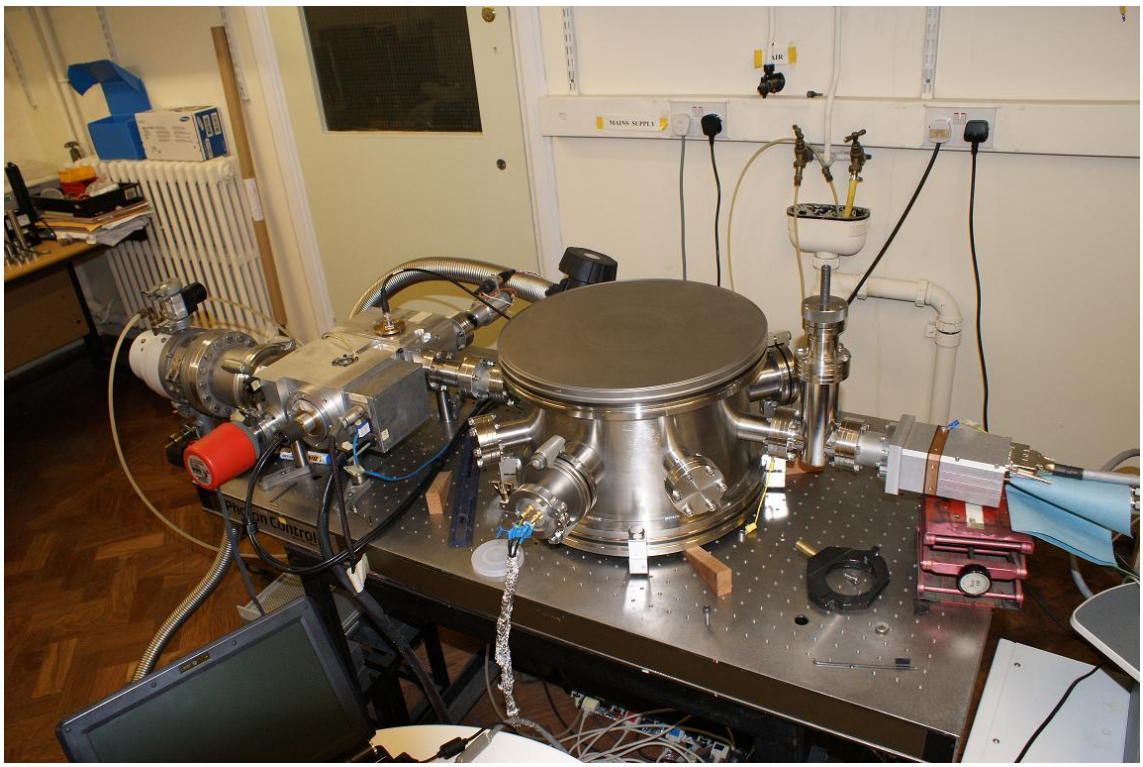

Figure 5.2: The McXI-I chamber installed on the microfocus X-ray source at KCL.

Within the McXI-I vacuum chamber all optics and apertures required to produce the final image are mounted on a removable platform, and are mechanically pre-aligned to a common axis using a laser. The focusing optics are mounted on piezoelectric stages, allowing each optical element to be positioned with sub micron accuracy while the microscope is under vacuum. Independent translation of both the CZP and MZP is possible, both along the optical axis (z) from source to detector, and also the horizontal (x) axis. Using the horizontal x translation, each of the zone plates may be removed completely from the optical path allowing X-rays to travel unobstructed towards the detector. This allows the effect of each optical element to be examined individually. The z translation of the CZP is used to select the X-ray energy focused onto the specimen, by changing the separation between the CZP and WSA, while the equivalent translation of the MZP is used to focus the magnified image onto the scintillator screen. The WSA is positioned at a fixed distance between the X-ray source and detector, and mechanical adjustments may only be made by

venting the McXI-I vacuum chamber. The diameter of the WSA may however be exchanged for different diameters, allowing a wider or narrower range of X-ray energies to be focused onto the specimen. The optics platform containing the optical components of the microscope including the specimen manipulation stage is shown in figure 5.3, with the optical axis (defined using laser alignment between the entrance and exit posts) passing through each optical element.

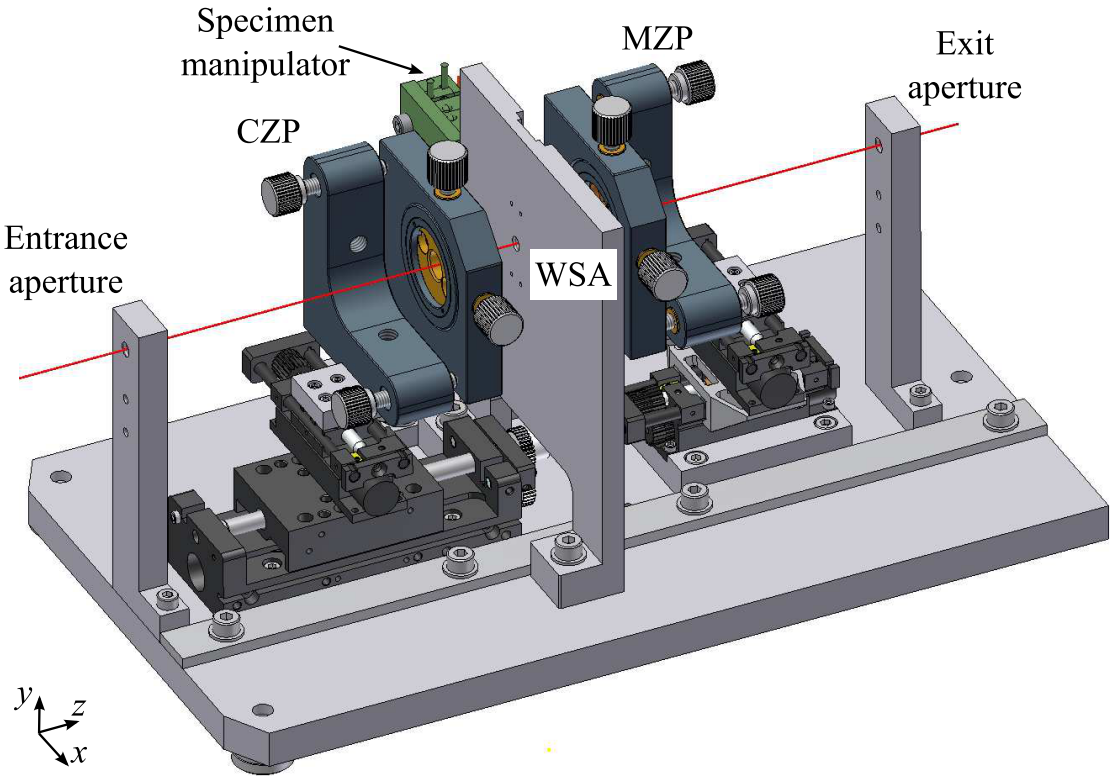

Figure 5.3: The McXI-I optics platform. This platform provides both mechanical and piezoelectric manipulations required to control the McXI-I microscope. The optical elements held on the platform are laser aligned to a common axis set by the entrance and exit posts outside the vacuum chamber. The platform is then installed as a single unit (*Image provided by* Delong Instruments).

Both the CZP and MZP used within the McXI-I system are designed with an outermost zone width of $d_n = 82\,\text{nm}$, and consist of 140 nm thick tungsten zones supported on a 100 nm thick silicon nitride membrane. The diameter of the CZP is $D = 1\,\text{mm}$, with a corresponding MZP diameter of $D = 0.2\,\text{mm}$. The zone structure of the CZP consists of 940 regions of linear gratings, arranged within a

circular pattern approximating the structure of a zone plate [8]. Each grating of the CZP consists of a $20\,\mu\text{m} \times 20\,\mu\text{m}$ square.

5.2.1 Characterisation of the McXI microscope

The aim of testing the McXI-I system using the microfocus X-ray source was to obtain the magnified image of a test specimen on the CCD detector, using the characteristic carbon K X-rays produced by the source. The test specimen identified was a Siemens star, allowing the resolution and performance to be assessed. It was first useful to examine the diffraction pattern produced as X-rays are focused by the CZP. This was achieved using both the carbon and aluminium solid targets with the microfocus source. The properties of the focused radiation are shown for each of the characteristic X-ray energies in figure 5.4. The circular symmetry of the zone plate produces an annular ring of diffracted light, that converge towards the focus spots corresponding to each order of diffraction.

Figure 5.4 shows the result as each of the diffraction orders is detected beyond the focus. It is shown that the orders $m = \pm 1$ for carbon K X-rays may overlap at the detector plane if the detector is positioned far beyond the focus. The higher orders of diffraction (not shown) will each produce a similar ring structure, with a larger diameter due to the shorter focal length as indicated by equation (1.19). The first order aluminium K_α is also shown to allow comparison. As the focal length of the CZP is much longer due to the higher energy X-rays, the diameter of the diffraction annulus will be smaller than that shown for C K. The plane located at a distance z'_{WSA} from the zone plate corresponds to the approximate position of the WSA.

The distances z'_{C} and z'_{Al} from the CZP to the focused spot due to the first order diffraction may be calculated using equation (1.17), with the focal length calculated by equation (1.18). These distances are summarised along with the

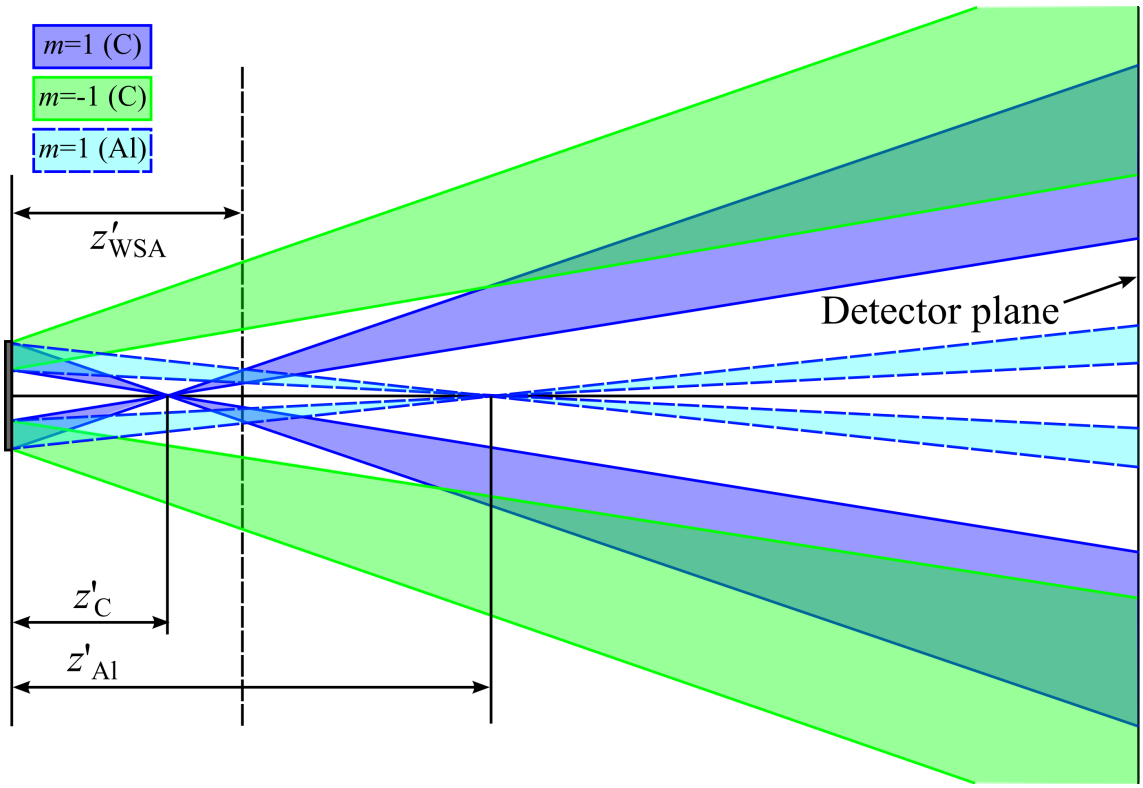

Figure 5.4: Diffraction from the CZP produces an annulus converging towards the focus. Diffracted light is shown for C K X-rays ($m = \pm 1$), and also Al K_α ($m = 1$).

separation between the CZP and WSA in table 5.1. The distances z correspond to the total range of travel possible for the z axis translation stage of the CZP.

Table 5.1: Summary of CZP characteristics for the McXI-I microscope using the microfocus source at KCL.

Energy [keV]	Focal length [mm]	z [mm]	z' [mm]	z'_{WSA} [mm]
0.227 (C K)	18.32	403	19.19	37.0
0.227 (C K)	18.32	421	19.15	18.6
1.487 (Al K_α)	98.33	403	130.07	37.0
1.487 (Al K_α)	98.33	421	128.26	18.6

As the WSA may be located both upstream and downstream of the focus, there must be a position allowing the focused spot and WSA to lie in the same plane ($z' = z'_{\mathrm{WSA}}$). It should therefore be possible to position the WSA at the focus, and

only allow the diverging X-rays from this focus to travel towards the detector. As the focal length for the Al K_α X-rays is much longer, the first order focus will always be located beyond the WSA.

The diffraction pattern obtained as the CZP is illuminated with the broadband X-rays produced by the microfocus source using the carbon target is shown in figure 5.5. This image shows the rings of diffracted light acquired with both the WSA and MZP removed from the McXI-I chamber, and so the filtering effect identified in table 5.1 will not occur.

The central diamond of figure 5.5 shows that X-rays are passing through the silicon nitride window (and zone plate), and travel towards the detector without deviation. The small inset b) shows this central region on a larger intensity scale (as the scale has been severely limited to a maximum of 150 counts in a) to allow the diffraction rings to be displayed, and all higher values are displayed as white), with the zone plate structure outlined in red. A small change in the transmission of X-rays through the zone plate is indicated by the small red circle in figure 5.5 b). This shows a region where the X-rays are blocked on the zone plate, either by debris or damage.

Surrounding the projection image of the silicon nitride window, an annular ring of low intensity "pinholes" was observed. This annulus corresponds to the light diffracted by the CZP, as shown in cross section in figure 5.4. The observed ring was an array of points rather than a continuous band of constant intensity due to the segmented structure of the CZP, and each point corresponds to diffracted light from each individual linear grating. The diffracted ring observed may be separated into each diffracted order, as the distances to the focus and detector from the CZP are both known (19.9 mm and 452 mm respectively). The boundaries of the diffraction rings are shown in figure 5.5 a), where $m = +1$ (blue) and $m = -1$ (green). The inner and outer diameters of the rings approximately describe the annular diffraction

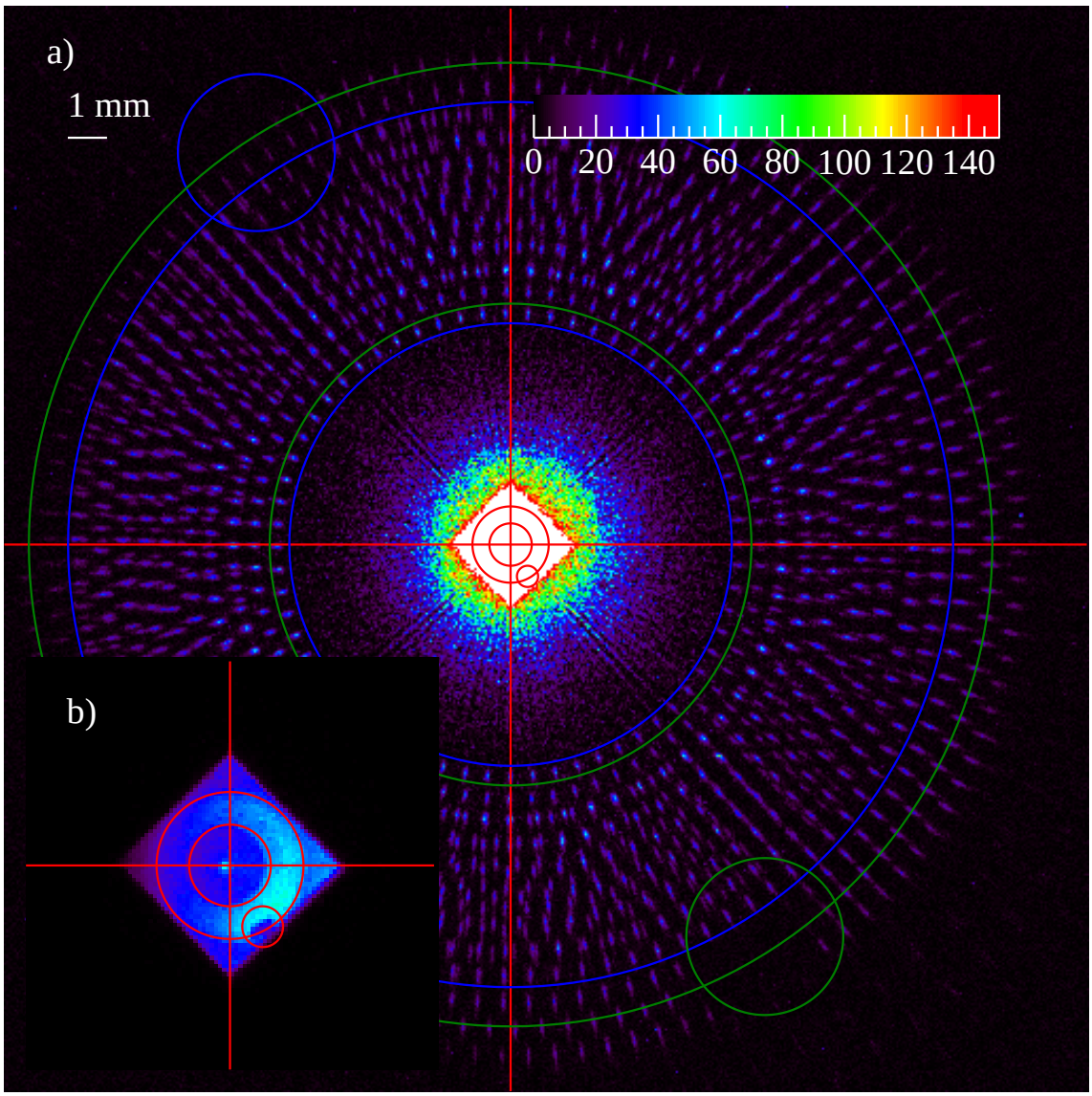

Figure 5.5: a) Diffraction pattern produced by the CZP following illumination using X-rays from the carbon target. The boundaries of the circular diffraction rings are approximated. b) The central region of a) showing the structure of the CZP transmitted.

ring observed. Where the two annular rings overlap, it may be said that the array of pinholes is approximately doubled, due to the contribution from both positive and negative orders of diffraction. The region of debris also may be used to support this, as the diffracted light is missing in both the lower right (green) and upper left (blue) quarters of the overlapping annular rings. The blue (where $m = +1$) region indicated is in the opposite quarter of the CCD image due to the inversion of the annulus as it passes through the focus spot, as shown in figure 5.4.

A comparable diffraction image is shown in figure 5.6, using the aluminium target of the microfocus source. The left hand panel a) shows the full area of the CCD chip, with the central square of the silicon nitride window supporting the CZP. The diffraction rings observed have a much smaller diameter than that obtained using the C target, due to the higher energy X-rays. The right hand panel b) shows the region indicated by the red square. This shows a representative image taken using a longer exposure time of the CCD, and therefore a higher intensity signal was collected. The long exposure time was achieved by positioning the gate valve over the bright central diamond shaped region. This prevents the CCD from saturating, and overwhelming the low intensity signal of the diffracted light.

The diameter of each of the diffraction rings is calculated using the previous method described for the characteristic carbon X-rays. The outer boundaries indicated by the circular arc segments shown in figure 5.6b correspond to $m = +2, -2, +3, -3, +4, -4$ in increasing radius, with positive orders shown in blue and negative in green. The outer boundary of the first order (not shown) is found to lie within the square of the silicon nitride window.

Both figures 5.5 and 5.6 were obtained with only the CZP in the optical path of the X-rays, the WSA and MZP were removed entirely from the McXI-I vacuum chamber. By placing the WSA close to the focused spot produced by the zone plate, a single diffraction may be selected. This is explained by figure 5.4, where a small

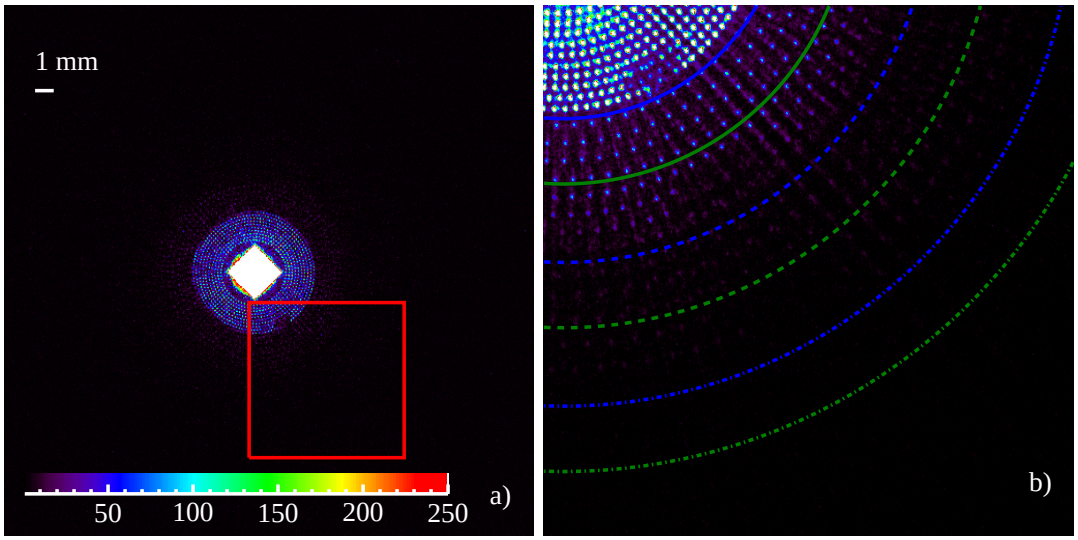

Figure 5.6: a) Diffraction pattern on the CCD detector using the carbon target. b) Shows a small region of the detector with a longer exposure to the X-ray beam. The diffraction rings correspond to $m = \pm 2, \pm 3$ and ± 4 respectively.

aperture placed a distance z'_{WSA} from the CZP will allow the C K X-rays through the pinhole. In order to achieve this, the pinhole must be precisely aligned with the focused spot.

As shown in table 5.1, the separation between the CZP and WSA can never be large enough to allow a single diffraction order of focused Al K_α X-rays to pass through completely. Figure 5.7 shows a small section of the annular ring diffracted Al K_α X-rays successfully focused through the WSA following diffraction. Examination of figure 5.4 shows this, if a small pinhole is placed a distance z'_{WSA} from the CZP, the annular ring of radiation has a large diameter as it converges through this pinhole. It is therefore possible for the pinhole to allow only a small segment of the focused light through.

In order to produce the diffraction pattern observed in figure 5.7, the diamond due to the silicon nitride window was aligned with the pinhole projection image through the WSA. The 40 µm diameter WSA pinhole is clearly visible as a bright region in the centre of the diamond. Such alignment is only possible due to the high

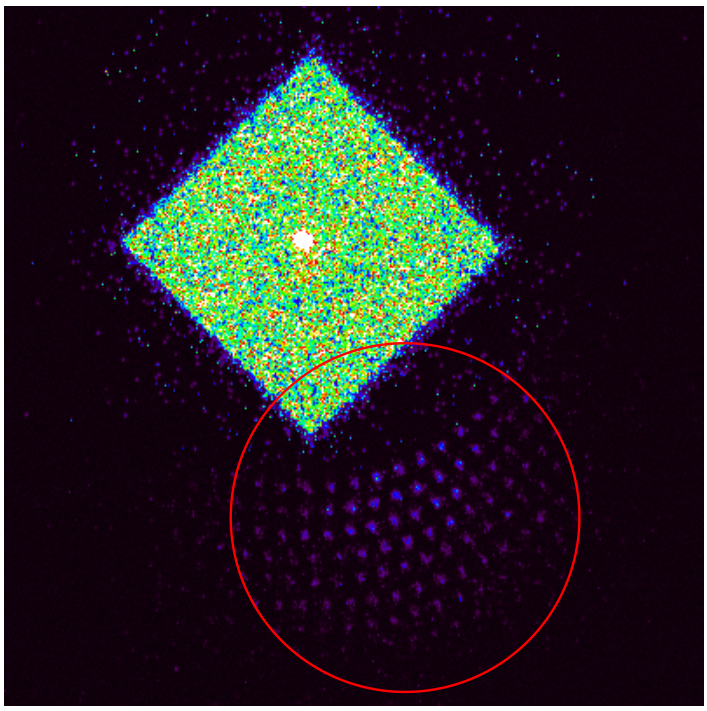

Figure 5.7: Diffracted Al X-rays passing through the WSA are projected towards the detector. As the size of the diffracted ring of radiation is much larger than the WSA, only a small circular segment passes through the 40 µm pinhole. The circular shape of the WSA pinhole is indicated by the red circle.

energy X-rays passing through the optical system. The total attenuation path for these hard X-rays includes the X-ray shutter (40 nm Ti, 50 nm silicon nitride), the CZP, (100 nm silicon nitride, 140 nm tungsten in the region of the zones) and the stainless steel foil defining the WSA aperture (thickness unknown).

While this filtering of Al K_α X-rays has been achieved, with further progress using this target limited only by the physical dimensions of the system, table 5.1 shows that it should be possible to obtain a full ring of diffracted light at the detector using the carbon target of the microfocus source, which may then be used to condense light onto the specimen. Several attempts were made to achieve this, using increasing WSA diameters (up to 1 mm), however the full diffraction ring was not observed.

5.3 Characterisation of soft X-ray micro zone plates

The objective lens of the McXI-II uses a small diameter Micro Zone Plate (MZP), to produce an image of the X-rays transmitted through the specimen. Such zone plates are developed by Silson Ltd. as part of the McXI project. Initial zone plate structures have been fabricated using the process described in section 1.8 a), by electroplating gold onto a silicon nitride surface. This has produced an MZP with a diameter of 200 μm, with an outermost zone width of $d_n = 100$ nm, and a typical thickness of 100 nm, as shown in figure 5.8.

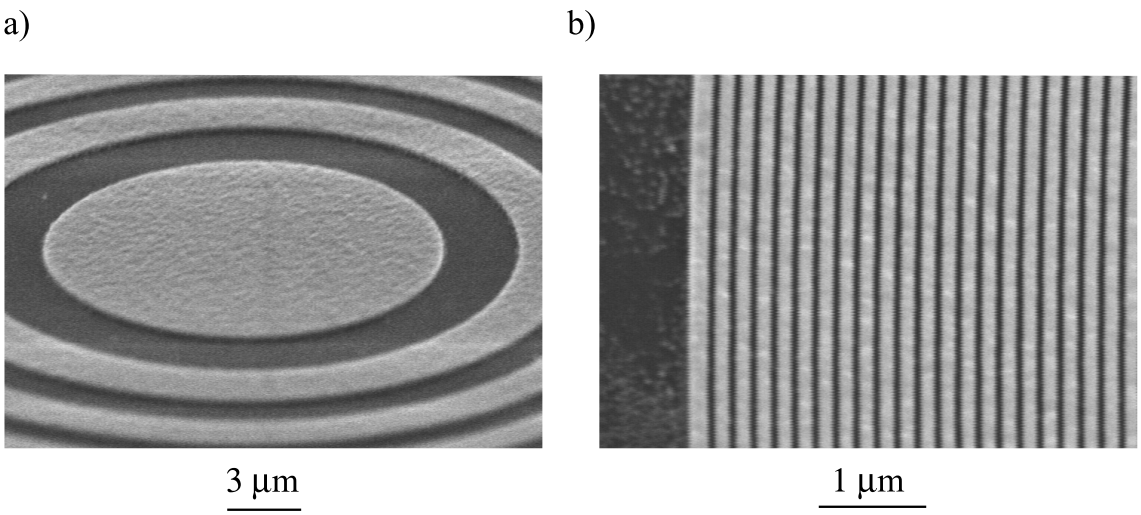

Figure 5.8: SEM images of a typical Au zone plate with a 100 nm outermost zone width. a) Central region showing the circular central stop. b) Outermost zones. (*Images provided by* Silson ltd.)

The MZP described above may be evaluated using the microfocus X-ray source and CCD detector. This has been achieved using the sample manipulator described in section 3.4 to position the MZP within the X-ray beam. It has been seen in figure 5.4, and throughout section 5.2.1 that a zone plate will produce a series of annular rings at a detector plane positioned far beyond the focused spot. It has also been determined that these rings may all overlap. The diameter of each annular ring for the MZP is estimated in figure 5.9, where the cross section of the diffracted light

is presented. Figure 5.9 assumes an equal diffraction efficiency between each order, with normalisation applied to ensure the total intensity in each diffracted order is constant. The diffraction rings shown in figure 5.9 are predicted for the distances $z = 290\,\text{mm}$, $z' = 295\,\text{mm}$.

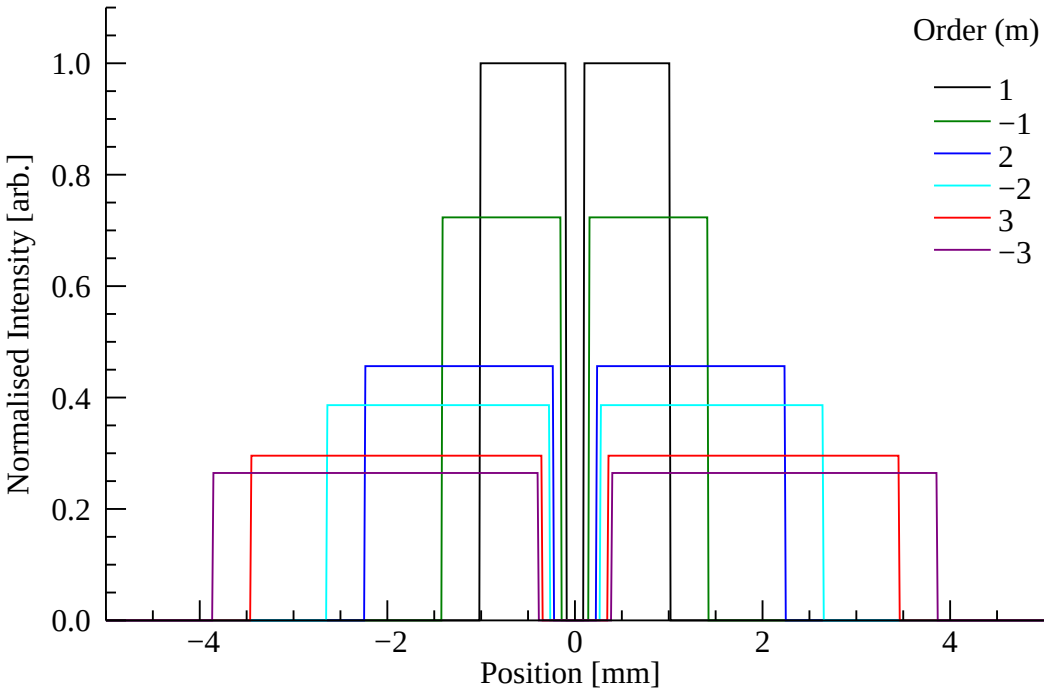

Figure 5.9: The intensity distribution produced in cross section due to the diffraction of aluminium K_α X-rays through the MZP. For each order of diffraction, the efficiency is assumed to be constant, as well as the total intensity diffracted into each order.

Equation (1.20) has shown that the diffraction efficiency is not always constant, with an efficiency of $\epsilon = 0$ for all even orders of diffraction. Figure 5.9 may therefore be altered to scale the diffracted rings to represent a more realistic model, however the even orders will be considered temporarily here, as a measure of the performance of the MZP. If radiation from the second order of diffraction is not observed, then the boundaries of the zone plate must be close to the ideal local mark to period ratio of 1 [9].

The resulting diffraction pattern obtained using the CCD detector and the MZP

is shown in figure 5.10, using the broadband X-rays emitted by the Al target. The central white region of the CCD is where X-rays pass undeviated to the detector through the silicon nitride membrane supporting the MZP. In this particular image the CCD is saturated, as identified by the bright side lobes extending horizontally from the central region. Surrounding this region are three concentric rings, the first two of which correspond to the diffracted light from the MZP. The outer disc of lowest intensity shows the diameter of the central aperture supporting the zone plate, and is caused by the high energy X-rays passing through the silicon frame (200 µm thick) of the zone plate without absorption.

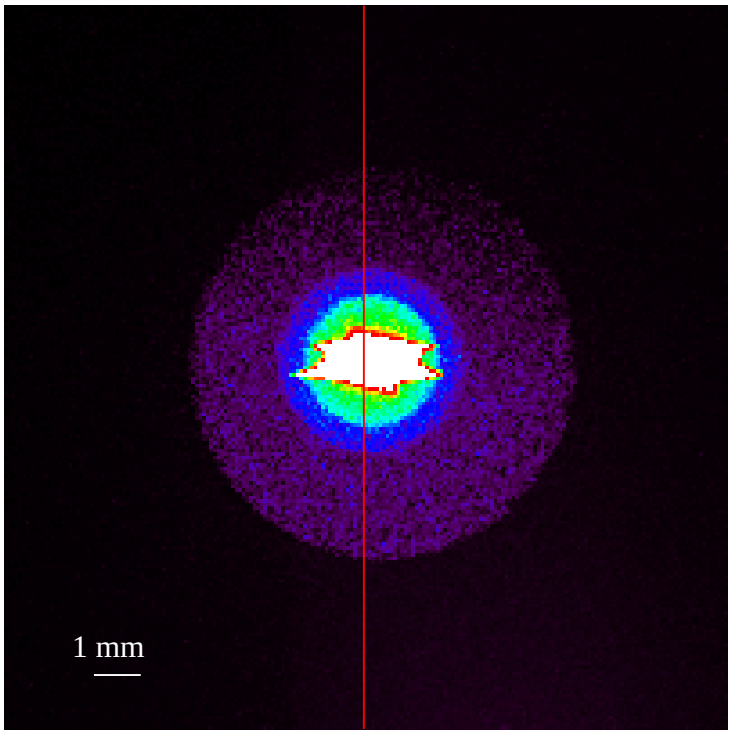

Figure 5.10: Diffraction pattern formed by zone plate of $d_n = 100\,\text{nm}$. The central (white) region shows saturation of the CCD due to X-rays passing through the transparent membrane supporting the zone plate. Two clear rings of diffracted light surround this central region.

The vertical red line in figure 5.10 is the line section plotted as the black experimental line in figure 5.11. The experimental intensity distribution has been averaged (by software binning) during analysis in order to improve the

observed ring structure due to the diffracted X-rays. The bright central region shows the undeviated radiation, extending $\sim 0.5\,\mathrm{mm}$ to either side of the centre. Symmetrically distributed either side of this central region, there are two slight distortions to the curve, which may be described as a "plateau" of constant intensity due to the diffracted light distributed into each order. The total intensity distribution is compared with the total of the $m = \pm 1$ diffraction orders shown in figure 5.9. The intensity of this predicted distribution is scaled in intensity to overlay with the plateau observed in the experimental line. The position of each of the plateaus does appear to match the predicted distributions for $m = \pm 1$.

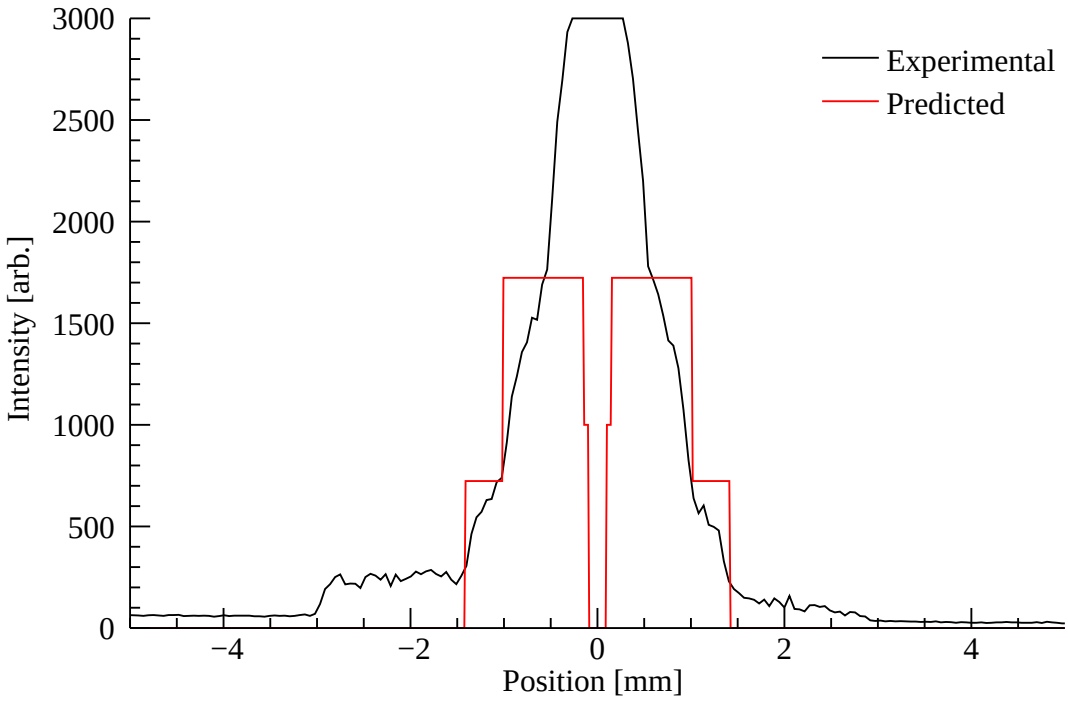

Figure 5.11: Vertical intensity distribution due to diffraction by a zone plate (black) compared to the predicted distribution from orders $m = \pm 1$.

There are no further plateaus with a wider width that are immediately visible in figure 5.11. It may therefore be assumed that the second and third order contributions to the intensity profile are negligible – the MZP appears to focus radiation more strongly into the first order only. This may be due to the low

diffraction signal levels measured, and further investigation may be required in order to show the higher orders of diffraction.

5.4 Summary

The McXI-I prototype microscope been has successfully integrated with the microfocus X-ray source. The characteristic C K and Al K_α X-rays produced by the source were used to characterise the focusing properties of the CZP. Using the hard X-rays produced by the source as an alignment tool, the projection images produced on the CCD detector allowed a partial diffraction pattern produced by the CZP to be projected through a pinhole. The microfocus source was also used to characterise a smaller diameter MZP. This has identified the first order annular diffraction rings, with no evidence seen for higher orders.

References

[1] *The McXI-II website*. http://www.mcxi.eu/index.php. Aug. 2011.

[2] *Making Cell Imaging Easier*. McXI Promotion Leaflet. 2010.

[3] *The NANO-UV website*. http://www.nanouv.com/. Aug. 2011.

[4] *Silson website*. http://www.silson.com/. Aug. 2011.

[5] *Delong Instruments website*. http://www.dicomps.com/. Aug. 2011.

[6] G. R. Morrison. *X-Ray Science & Technology*. Ed. by A. G. Michette and C. J. Buckley. IOP Publishing, 1993. Chap. 8.

[7] K. Powell. Priviate communication. Sept. 2011.

[8] U. Vogt, M. Lindblom, P. Charalambous, B. Kaulich, and T. Wilhein. "Condenser for Koehler-like illumination in transmission x-ray microscopes at undulator sources". In: *Optics Letters* 31.10 (2006), pp. 1465–1467.

[9] A. G. Michette. *Handbook of Optics*. Ed. by M. Bass. 2nd ed. Vol. 3. McGraw-Hill, 2001. Chap. 23, pp. 23.1–23.9.

Chapter 6

Conclusions

This thesis has concentrated on describing the optical performance of grazing incidence reflective channel arrays, with characteristic Al K_α X-rays of energy 1.487 keV. These Microstructured Optical Arrays or MOAs have been developed as part of the Smart X-ray Optics consortium, to provide a broadband alternative to zone plates for focusing X-rays, particularly for use in radiobiological experiments. This work has involved adaptations to an electron bombardment X-ray source in order to estimate the performance of both MOAs and zone plates.

6.1 Microstructured Optical Arrays

Zone plates are widely used to focus soft X-rays due to the high spatial resolutions achievable, however they are limited in the intensity delivered to the focused spot. The combination of low efficiencies due to multiple diffraction orders, chromatic aberration, and potentially small apertures reduce the ability of a zone plate to produce a high intensity focused spot. As the MOA focuses radiation using grazing incidence reflection, they are able to efficiently focus X-rays to the focus spot using a much larger aperture than that of a zone plate due to the high reflectivity at the outer edges of the active area. The focal length of the MOA is constant for

broadband radiation, and so a high flux of polychromatic X-rays can be delivered to the focused spot. Zone plates require a monochromatic X-ray source in order to eliminate the chromatic aberration.

MOAs use grazing incidence reflection from an array of channels, with the cumulative effect from the array contributing to the focused spot. In this respect, they share similarities with other focusing optics using a channel structure (MCP, lobster-eye, polycapillary), using the cumulative effect from an array of channels to produce a focused spot. MOAs however potentially have the capability to produce an actively controllable focused spot, with piezoelectric actuators curving the thin substrate of the channel array. Such actuation has successfully been applied to a MOA, producing an optical element with a radius of curvature below 50 mm. The use of two (or potentially more) reflections achieved by placing two MOA structures along the X-ray path has also been described. Reflection from two successive MOA arrays in this way has a number of advantages over that of a single reflection, including a wider aperture (by reducing the grazing angle at the edge of the active reflecting area), control of aberrations (primarily coma), and relaxing the necessity for a small radius of curvature.

Two methods have been described as a way of producing MOA channels in a thin silicon substrate, both of which have been optically characterised in chapter 4 of this thesis. Of these two anisotropic methods, DRIE etching of the channel structure produces a rougher reflecting surface, whereas the chemical etching produces very smooth (< 2 nm RMS) roughness channel walls.

6.2 The microfocus soft X-ray source

The microfocus X-ray source used within this thesis has been modified in order to allow a CCD detector to be coupled to the system. These changes to the X-ray path have allowed the installation of a sample manipulator, allowing optical elements to

be inserted into the X-ray path, allowing the performance to be monitored using the CCD detector. The optical characterisation apparatus (microfocus source, sample manipulator and CCD detector) developed has been further improved, most recently by the installation of an X-ray shutter, drastically reducing the stray light (both visible and X-ray), allowing lower intensity signals to be observed.

The overall performance of the microfocus X-ray source has changed continually during its lifetime, as modifications and upgrades are continually implemented. This has been true even before the source was installed at KCL in 2008. Due to the historical variation in the optimum parameters, following the recent redevelopment the current performance has been described. This recalibration has shown that the X-ray source size is typically smaller than 200 µm in diameter, with an electron beam current of 80 µA focused onto the target.

6.2.1 Optical performance of MOAs

Optical testing of MOAs has been performed using the microfocus X-ray source. In order to perform this testing, the radiation reflected by the MOA towards the focus spot needed to be separated in the plane of the CCD detector from the higher intensity distribution passing through the MOA channels without reflection. This was achieved by translating the MOA linearly across the optical axis, allowing the reflecting properties of an unactuated MOA to be examined at each position of the sample manipulator. The images obtained using the CCD were compared with simulated distributions.

The optical testing performed indicates that both methods of producing MOAs reflect the broadband X-rays generated by the aluminium target of the microfocus X-ray source in a consistent manner. Testing of the chemically etched MOAs shows that the channels may be slightly tapered. Additional testing at BESSY-II has shown that the walls within each channel may be misaligned by as much as 0.5°.

This results in the formation of a double image, produced by the non-parallel channel walls, and further investigation is required to either eliminate this effect during production of the MOA, or to compensate for the misaligned channel walls using actuation of the MOA substrate.

6.2.2 Optical performance of the McXI microscope

The McXI project has been developing a tabletop X-ray microscope, designed to provide imaging of biological samples down to a resolution of 30 nm. A prototype microscope has been tested on the microfocus X-ray source at KCL in order to develop alignment techniques of the optical elements, and to ultimately characterise the performance of the microscope. CCD images of the diffraction pattern resulting from the condenser zone plate were presented, using the characteristic X-rays produced by the carbon and aluminium targets of the microfocus source. Attempts to spatially filter the diffraction pattern, by placing a pinhole at the focus of the condenser zone plate were made. This allows the high orders of diffraction to be removed from contaminating the microscope image. A partial diffraction ring structure was observed using the X-rays produced using the aluminium target. Only a partial diffraction ring was observed as the focused spot of aluminium X-rays was positioned far beyond the pinhole.

The physical layout of the microscope should have allowed the spatial filtering of the characteristic carbon X-rays, as the pinhole may be positioned at the focused spot. This was found to be close to the limit of the translator of the condenser zone plate when coupled to the microfocus X-ray source. This is not an issue for the final microscope in development, as the distance between the source and condenser zone plate is much larger in the final system, and the aluminium X-rays are beyond the designed energy of the microscope.

The McXI project has also allowed the characteristaion of zone plates under

development to be performed. While this has not allowed the overall efficiency or resolution to be determined, the focusing of characteristic aluminium X-rays has been shown. The absence of higher diffraction orders in the CCD images collected means that the first order efficiency of the zone plate tested is not comparable with the higher diffraction orders.

6.3 Future outlook

Microstructured Optical Arrays have been characterised successfully using the microfocus X-ray source, however there are a number of improvements that could be made to allow the results to be refined further. Firstly, the microfocus X-ray source is producing a broadband range of X-ray energies, of which the characteristic emission energy has the highest intensity. The high energy bremsstrahlung produced by the microfocus source is evident in both MOA and zone plate measurements, as a disc of constant intensity, often overlapping at the detector plane with the important focused radiation. Implementation of a grazing incidence mirror (such as that described in section 3.5.2) will remove the high energy X-rays contributing to this background, allowing features close to the unreflected or undiffracted signal to be investigated. Such a mirror assembly is currently in development, and may be used with a transmission diffraction grating (currently awaiting installation within the sample manipulator) in order to determine the X-ray spectrum emitted by the source following the reflection. Further investigation is also required of the properties of the microfocus source, to ensure that the focused electron beam at the X-ray target is as small as possible while maintaining a comparable current. This may achieved by measuring the target current, while changing the current of the focusing lens, the Wehnelt potential and distance between the Wehnelt tip and filament. Each of these may have an effect on the electron distribution focused onto the target, hence the X-ray source size. Previous users of the microfocus source

have reported larger focused electron currents (500 μA [1]), and smaller electron distributions ($\sim$ 5 μm [2]) at the target than those presented within this thesis. Further investigation is therefore required to determine the optimum settings for the source.

There are also a number of routes potentially available in order to further describe the focusing properties of MOAs. This thesis has concentrated on examining unactuated structures, where the channels are considered to be parallel to the optical axis. The mounting and in-vacuum control of actuated samples has been considered [3], and has been designed to be easily installed onto the sample manipulator of the microfocus source. Actuation of the MOA will then change the distribution due to reflected X-rays in the plane of the CCD. The methods used to characterise unactuated MOAs will need to be refined, as the MOA channels can no longer be considered to be an extension of an infinite unactuated surface. A more suitable method may be to use the actuated MOA in a vertical configuration, where the focusing properties can be observed within the shadow of the central stop. In this configuration the reflections should occur from channel walls distributed symmetrically either side of the optical axis.

The simulation routines described in section 2.7 may also be extended in order to consider actuated MOAs. The current model only considers unactuated MOAs, where the channel walls are expected to lie parallel to the optical axis. This allows the symmetry of the reflection to be very easily determined. Calculation of the resulting reflection from a tilted channel will be possible. This may however require a higher degree of computation in order to calculate both the tilt angle at each end of the channel, as well as the converging angle of the reflected X-ray, calculated using the grazing reflection angle. Any developments made should attempt to keep the current capabilities of the current routines intact, allowing the change in profile at different spacings of the MOA and CCD detector, and translation of the MOA

across the optical axis as demonstrated within this thesis.

References

[1] M. Folkard, G. Schettino, B. Vojnovic, S. Gilchrist, A. G. Michette, S. J. Pfauntsch, K. M. Prise, and B. D. Michael. "A focused ultrasoft X-ray microbeam for targeting cells individually with submicrometer accuracy". In: *Radiation Research* 156.6 (2001), pp. 796–804.

[2] G. Schettino. "Development of a focused X-ray source as a microprobe of cellular radiation response". PhD thesis. University of London, 2000.

[3] D. Rodriguez Sanmartin, D. Zhang, T. Button, C. Meggs, C. Atkins, P. Doel, D. Brooks, C. Feldman, R. Willingale, A. Michette, S. Pfauntsch, S. Sahraei, M. Shand, A. James, G. Willis, C. Dunare, T. Stevenson, W. Parkes, and A. Smith. "Development of spider micro-structured optical arrays for X-ray optics". In: *Proceedings of the SPIE - The International Society for Optical Engineering* (2010), 780306 (11 pp.) DOI: 10.1117/12.860420.

Appendix A

X-ray absorption and reflection data

The properties of reflection and absorption of X-rays have been introduced in section 1.3. The following figures (A.1 and A.2) show the reflectivity from a silicon surface at grazing angles, with unpolarised light and a negligible surface roughness. The reflectivity profiles are shown for a range of grazing angles across the X-ray energy spectrum in figure A.1, and the characteristic energies produced by the microfocus source (C K = 0.277 keV, Al K_α=1.487 keV).

Also shown are the X-ray transmission through various filters and substrates used within this thesis. These have been calculated using equation (1.13). The data used for all figures used within this thesis has been obtained using the "X-ray database",

`(http://henke.lbl.gov/optical_constants/),`

produced as a tool used for calculating such datasets.

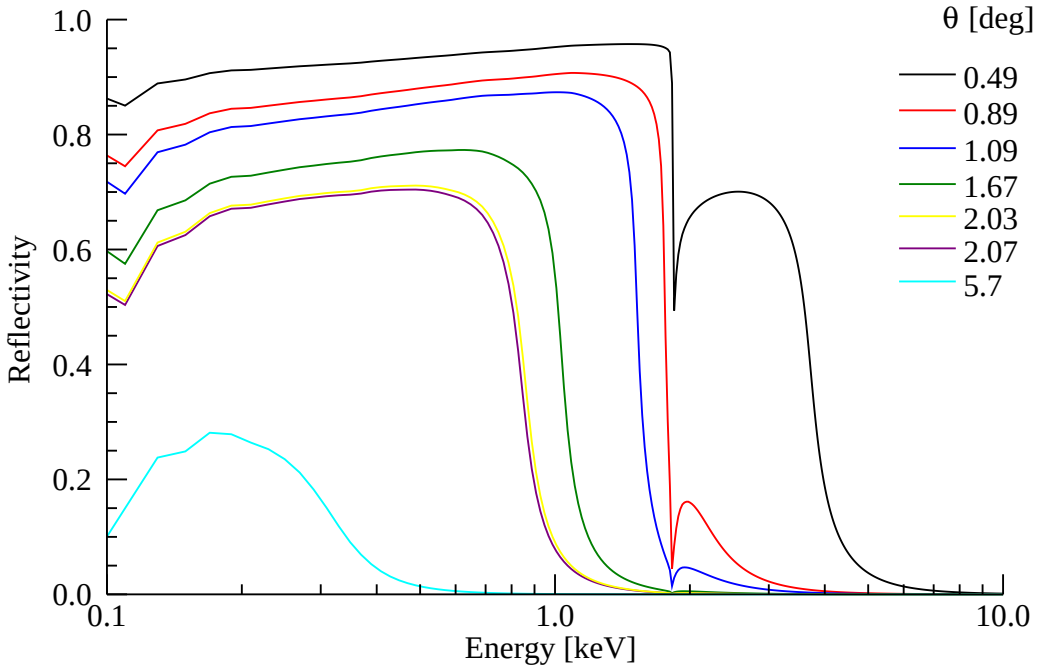

Figure A.1: Reflectivity *vs* energy curves generated for silicon, showing a variety of grazing angles.

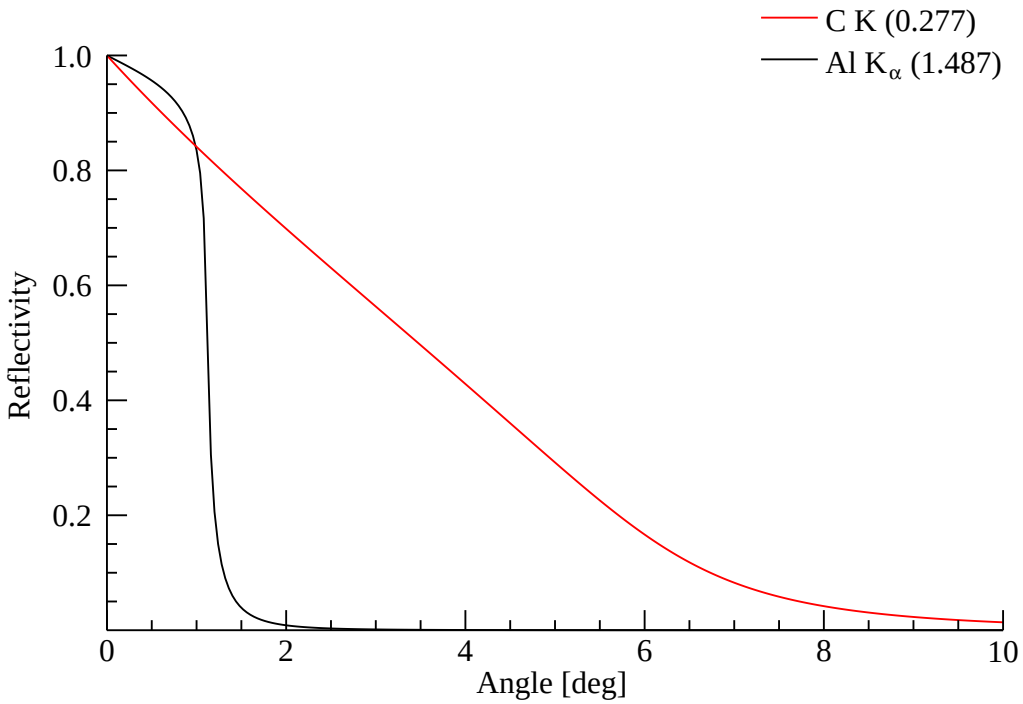

Figure A.2: Reflectivity *vs* grazing angle curves generated for silicon, for the characteristic X-ray energies produced by the microfocus source.

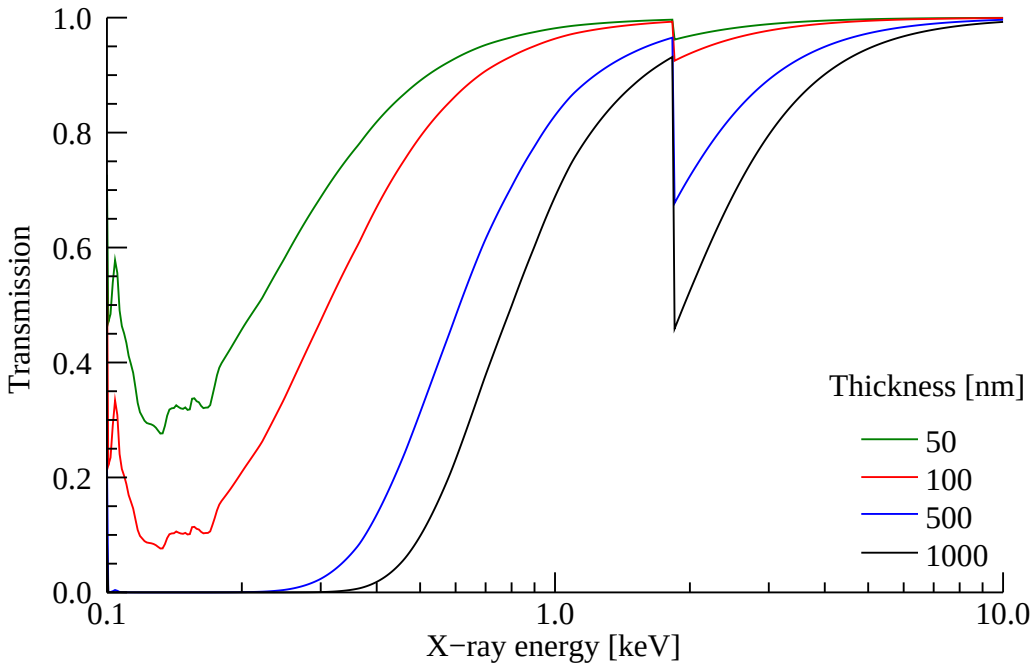

Figure A.3: X-ray transmission curves generated for a variety of thicknesses of silicon.

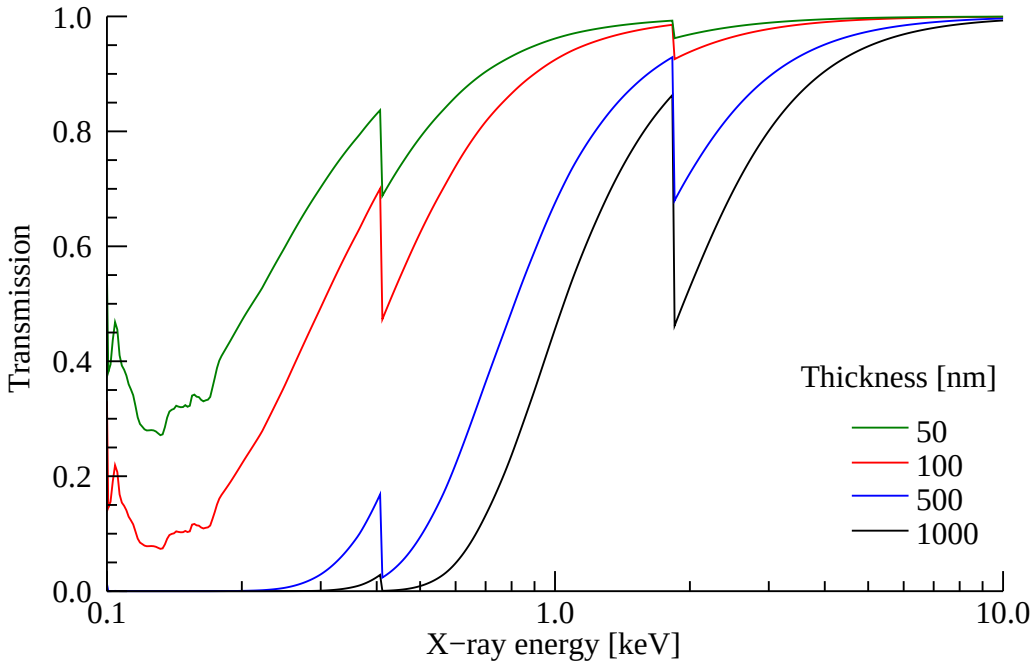

Figure A.4: X-ray transmission curves generated for a variety of thicknesses of silicon nitride.